UNIVERSITY OF OKLAHOMA

GRADUATE COLLEGE

QUANTUM PLASMONIC SENSING USING SQUEEZED LIGHT

A DISSERTATION

SUBMITTED TO THE GRADUATE FACULTY

in partial fullfillment of the requirements for the

Degree of

DOCTOR OF PHILOSOPHY

By

MOHAMMADJAVAD DOWRAN
Norman, Oklahoma
2021

QUANTUM PLASMONIC SENSING USING SQUEEZED LIGHT

A DISSERTATION APPROVED FOR THE
HOMER L. DODGE DEPARTMENT OF PHYSICS AND ASTRONOMY

BY THE COMMITTEE CONSISTING OF

Dr. Alberto M. Marino, Chair

Dr. Eric Abraham

Dr. Arne Schwettmann

Dr. Ian Sellers

Dr. Bin Zheng

To my beloved parents: ***Maman Shayesteh*** *and* ***Baba Hassan***

Acknowledgements

I want to express my sincere gratitude to my advisor, Dr. Alberto Marino, for his support and training during the entire time of my research project. He helped me tremendously to become a successful experimental researcher in quantum optics. I sincerely appreciate his tireless efforts. Also, I want to thanks my senior graduate researcher, Matthew Holtfrerich, who patiently explained the research to me. Plus, I am humbly grateful to another colleague and a close friend of mine, Dr. Ashok Kumar, for helping me understand the experimental techniques in our research and provide me with great insight through productive discussions. I would also like to thank other members of our group who helped me through my research in a different capacity: Timothy, Saesun, Gaurav, Aye, and Umang; I enjoyed working with you.

I also want to thank these people who were outside our research lab, but their share of support was undeniably integral to my research progress:

- The professional experts of the instrument machine shop: Mr. Joel Young and Mr. Barry Bergeron, for their helpful and instructional discussions and technical supports, and their friendly attitude.

- My course work professors, in particular Professor Kantowski, and Professor Milton.

- The Physics department administrations, Professor Gutierrez, Professor Strauss, and the front office, for keeping my academic records on the track.

– Grant sponsors: the W. M. Keck Foundation, the Farzaneh Family Foundation, Shafer-Ray Family, the national science foundation (NSF), and the Avenir Foundation, for awarding me assistantships, scholarships, and fellowship. I appreciate their generous support.

– Our research collaborators: Dr. Lawrie and Dr. Pooser, from Oak Ridge National Laboratory, Dr. Manjavacas and Keith Sanders from the University of New Mexico, and the Sandia National Laboratory.

– And, my Ph.D. advisory committee members: Dr. Abraham, Dr. Schwettmann, Dr. Sellers, and Dr. Zheng.

Thank you all!

Throughout the seven years of my graduate studies in the US, I was lucky to have the best supportive friends one can imagine: Alireza, Nafiseh, Morteza, Mohamad, Parisa, Tanaz, and Tehrani; My life out of the university was lame without you. Thanks for standing by me when I needed you. I would also like to thank Saleh, Shima, Joel, Kara, Faranak, Behzad, Mahdokht, Mohamad, Moti, Mahyar, Tahere, Peyman, Golya, Hadi, and Elahe. Thank you!

Last but not least, I could not reach where I am without my supportive family back home. We were apart, but you are, and always have been, in my heart: Baba, Maman, Behzad, Bahareh, Behnaz, AliAgha, Ali, Elham, MohamadReza, Yalda, Fatemeh, Sina, Sara, Omid, Yeganeh, and Dana. You are my life, my motive to move forward. I love you all and I count to see you soon!

Table of Contents

List of Tables

List of Figures

Abstract

Quantum sensing is an emerging field of quantum optics that seeks to take advantage of quantum correlations available in quantum states of light to enable sensitivities beyond the fundamental classical limits. The sensitivity of measurements and sensing apparatus when using classical states of light is limited to the shot-noise limit (SNL), which is achieved with coherent states of light.

Two-mode squeezed states of light (twin beams) have quantum correlations both in time and space, leading to temporal and spatial squeezing properties. Several applications can benefit from such noise reduction to enable new approaches, such as quantum-enhanced interferometry, quantum imaging, and quantum sensing. The emergence of quantum technologies has been referred to as the second quantum revolution. For metrology and sensing applications, in particular, it has led to new state-of-the-art sensitivity limits.

In this thesis, we discuss the implementation of quantum sensing based on squeezed states of light and plasmonic sensors as a platform for the demonstration of real-life quantum sensing. We present a quantum-enhanced plasmonic sensing setup that can detect changes in the refractive index of air beyond the SNL. Furthermore, we generalize such experimental apparatus to probe an array of sensors using the quantum correlations present in different spatial locations to demonstrate a parallel quantum-enhanced plasmonic sensing scheme that can simultaneously detect changes in the refractive index of air in multiple locations with a single probing beam. These results

prove the applicability of twin beams for real-life applications based on plasmonic sensors. The spatially resolved sensing scheme can be extended to pixel-size sensing of multiple sensors for multi-parameter estimation and detection applications to reach more complex sensing architectures.

List of Acronyms

AOM	acousto-optical modulator
BS	beam splitter
BTMSS	bright two-mode squeezed state
CL	confidence level
CS	coherent state
DI	deionized
DLP	digital light projector
EA	electronic attenuation
EBL	electron-beam lithography
EN	electronic noise
EM	electromagnetic
EOT	extraordinary optical transmission
EQEF	effective quantum enhanced factor
FIB	focused ion-beam
FOM	figure of merit
FWM	four-wave mixing
HD	homodyne detection
HJ	hybrid junction
HWHM	half-width half-max
HWP	half-wave plate
ID	intensity difference
LO	local oscillator
OPA	optical parameter amplification
ORNL	Oak Ridge National Laboratory
PBC	periodic boundary condition
PDF	probability distribution function
PEC	perfect electric conductor
PID	proportional-integral-derivative
PMC	perfect magnetic conductor
PML	perfectly matched layer
PMMA	poly-methyl methacrylate
PZT	piezoelectric transducer
QCRB	quantum Cramér-Rao bound
QEF	quantum enhancement factor
QM	quadrant mask
QPD	quadrant photodetector
QPS	quadrant plasmonic sensor
RBW	resolution bandwidth
RIU	refractive index unit
SA	spectrum analyzer
SAS	saturation absorption spectroscopy
SEM	scanning electronic microscope
SHG	second harmonic generation
SNL	shot-noise limit
SNR	signal-to-noise ratio
SPP	surface plasmon-polariton
TB	twin beam
THG	third harmonic generation
TM	transverse magnetic
TMSS	two-mode squeezed state
VBW	video bandwidth
VTMSS	vacuum two-mode squeezed state

Chapter 1

Introduction

Classical states of light are fundamentally noisy. Even if we can overcome the noise from technical imperfections, there is intrinsic fundamental noise originating from vacuum fluctuations of the electromagnetic modes of light. Laser light, for instance, is coherent and monochromatic; however, it is noisy in its core photon statistics, as its photons are randomly emitted with no correlations between them. An ideal laser beam without any technical classical noise represents a "coherent state," whose photons are randomly distributed in space and time, following a Poisson distribution. The noise of such a coherent state determines the fundamental noise limit for classical states of light, called the shot-noise limit (SNL), and is set by the uncertainty principle in quantum mechanics. The SNL defines the bound for the sensitivity of optical readout sensing and measuring devices when probed with classical states of light.

Quantum mechanics provides the solution to overcome this fundamental noise limit through the use of quantum-correlated states of light that show reduced-noise properties. Therefore, sensors and measurements which use such states can provide sensitivities beyond the SNL when probed with equal numbers of photons as their classical counterpart. While classical states are limited by the SNL, the states that can beat the SNL are referred to as the "quantum states" [1]. Anti-bunched states, Fock states, entangled and squeezed states are among the quantum states that have been introduced and studied both theoretically and experimentally over the past few

decades. Each of these quantum states can provide different advantages for particular applications.

In this thesis, we focus on two-mode squeezed states of light, also known as the "twin beams". These states can exhibit significant quantum correlations between their photons, and therefore can reach large noise cancellations, or "squeezing," compared to coherent states at the SNL. We can generate twin beams with high quantum correlations on-demand and with high intensities. Moreover, there are sensing devices that can benefit from these states without a significant modification in their setup for implementing quantum sensing.

The main goal of this thesis is to demonstrate the applicability of twin beams of light for enhancing the sensitivity of compatible shot-noise limited sensing and measurement devices. In particular, we use plasmonic sensors [2] and enhance their sensitivity in the detection of changes in refractive index beyond the SNL. Plasmonic sensors are nano-fabricated devices that are widely used in biochemical and medical diagnosis applications. These sensors have been reportedly reached the SNL when classical states are used to probe them [3]. Since the resonance response of these nanohole-structured sensors can be tuned to show maximum sensitivity at the wavelength of interest, we can use them as a platform for implementing quantum-enhanced sensing compatible with real-life applications. Moreover, using spatial quantum correlations in the twin beams, we implement quantum plasmonic sensing in a parallel configuration. Such experiments take the quantum states of light from fundamental studies into more practical applications, paving the way for other quantum-enhanced applications in

metrology, imaging, and information processing that can benefit fields such as biology, chemistry, and so on. Over the past two decades, the emergence of quantum-correlated states opened new opportunities for different applications, which has drastically changed the field of sensing and metrology. In this chapter, I briefly review the evolutionary progress of quantum sensing.

1.1 Quantum Revolution

Near the end of the nineteenth century, classical physics was at its highest level of maturity, which made physicists of that time confident in classical formulations of physical phenomena, ranging from the everyday motion of objects and fluids, to electromagnetic waves and optics. However, some problems were not fully understood, as they did not follow the expected behavior from classical theories [4]. Some of these phenomena include the photoelectric effect, black-body radiation, and atomic structure, to name a few. The pivotal point in the history of physics was Albert Einstein's interpretation of light as composed of particles, which was able to successfully explain the photoelectric effect in 1905. In his theory, he proposed light to be consisting of "quantized" packages of energy, called "photons."

This theory and other follow-up studies and discoveries revolutionized the Newtonian interpretation of light as "waves" and built the foundations of a new field of physics: quantum mechanics. This new formulation studies physical phenomena based on the probability of events happenings and the introduction of the uncertainty principle

for complementary variables. Moreover, the act of measurement and observation are described by operators that affect the physical system under study. Some of these approaches were counter-intuitive compared to the classical picture. Furthermore, the probabilistic interpretation of events in quantum mechanics leads to fundamental uncertainties in measurements, in contrast to classical measurements which are deterministic.

Apart from its success in explaining unanswered questions in physics, quantum mechanics has also been able to predict new experimental realizations based on its assumptions. The invention of the laser by Maiman in 1960 [5] provided a source of coherent photons in space and time and opened a new chapter in quantum optical phenomena that rely on nonlinear behaviors from materials. The emergence and development of nonlinear optics provided the required infrastructure for the generation of correlated photons, leading to the generation of new quantum states of light.

1.2 Second Quantum Revolution: Quantum Sensing

Science and technology provide the two platforms for evolving our understanding of the universe. Sometimes science predicts new concepts, which directs the engineering efforts for inventing new apparatuses and techniques, and sometimes new technologies lead to opportunities for physicists to enrich and deepen related sciences. These two fields also complete each other and emerging new concept in one leads to evolving the other one. For example, the uncertainty principle defines the relation between non-commuting

operators, and leads to a fundamental uncertainty in a measurement, independent of the measuring apparatus, and hence limiting the sensitivity and resolving power of classical measurements [6]. This concept fundamentally limits the sensitivity of measurements but provides technological opportunities to reach that limit.

In 1963, Glauber [7] developed the quantum optical theory of coherence and predicted the possibility of surpassing the SNL with particular quantum states while still satisfying the uncertainty principle. In 1977, Kimble and Mandel [8] showed the experimental realization of photon anti-bunching in resonance fluorescence from a two-level atom as the first demonstration of quantum states of light. Later, in 1985 Slusher [9] showed the first experimental realization of squeezed states of light through the nonlinear interaction between laser beams and sodium atoms.

The theory of quantum mechanics led to the *first quantum revolution*, which revolutionized our understanding of atomic and photonic physics. The new theoretical tools from the first quantum revolution evolved into practical technologies that translated fundamental science into application. Due to the importance of the emerging quantum technologies, the beginning of the 21$^{\text{st}}$ century is referred to as the beginning of the *second quantum revolution* [10]; the era for the advent of new quantum technologies: quantum computers, quantum information, and quantum metrology (including sensing, detecting, and imaging) [11].

The field of quantum sensing is evolving rapidly and includes applications in spectroscopy [12, 13, 14], interferometry [15, 16, 17] and gravitational wave detectors, such as LIGO [18, 19, 20, 21], precision measurement [22, 23], below-shot-noise sens-

ing applications [24, 25], chemical detection [26, 27, 28, 29, 30], and imaging systems [31, 32, 33, 34, 35]. In particular, quantum sensing and metrology seek to use quantum states to enhance measurements or parameter estimation to a level better than the corresponding classical strategies at the SNL [36, 37, 38], through the use of photonic states [39], atomic states [40], and even molecular states [41]. Optical quantum sensing and metrology can benefit different measurement techniques by taking advantage of quantum states to improve their sensitivity and detect smaller signals.

1.3 Thesis Outline

In chapter 2, we define the quantum states of light that we use in our experiments, twin beams, and their reduced noise properties, as well as theoretical and experimental tools for producing and characterizing them. These states provide the tools for enhancing the sensitivity of compatible measurements. The definition of sensitivity and the ways to enhance it will be studied in chapter 3, clarifying the role of quantum states in reaching sensitivities beyond the SNL. In chapter 4, we study plasmonic sensors and their role as a real-life platform to implement quantum-enhanced sensing. We study their functionality, as well as their characteristic response to an incident probing light. Combining the quantum states and the plasmonic sensors, we demonstrate a quantum-enhanced plasmonic sensing configuration in chapter 5. Moreover, we experimentally show the capability of twin beams to realize a quantum-enhanced plasmonic sensing scheme. In chapter 6, we extend this implementation to an array of plasmonic sensors

and implement a parallel quantum plasmonic sensing scheme that uses the temporal quantum correlations at different spatial locations within the twin beams. Finally, in chapter 7, we discuss the possibility of future work for providing further enhancements in the sensitivity of the presented quantum plasmonic sensor configurations.

Chapter 2

Squeezed States of Light: Twin Beams

Following the first theoretical studies on the quantization of an electromagnetic field, Glauber in 1963 developed the theory of coherence that predicted quantum states of light with sub-Poissonian photon statistics [42], such as photon anti-bunched states. Less than a decade later, squeezed states of light [43, 44, 45] were first introduced theoretically by Stoler [46, 47]. Later, Yuen [48, 49] and Caves [6] proposed using these states for enhancing the sensitivity of an interferometer below the SNL. The first experimental observation of squeezed states was in 1985 by Slusher [9]. They generated quadrature-squeezed states with sodium atoms. Such squeezed states provide the noise-reduced tools for probing sensors to reach sensitivities better than the SNL.

In this chapter, we introduce some definitions required to understand the properties of squeezed states, in particular two-mode squeezed states (TMSS) or twin beams of light, as well as techniques for generating them. We also present the theory needed for the noise analysis through measurement methods to study the temporal and spatial quantum correlations in the twin beams.

2.1 Quantum Description of Light

As first derived by Glauber in 1963 [7], in quantum mechanics, a single mode monochromatic field of light at frequency ω can be described by quantizing it with a single cavity mode that behaves like a simple harmonic oscillator of unit mass. Such an electric field

can be described in time (t) as:

$$\hat{E}(t) = E_0(\hat{a}e^{i\omega t} + \hat{a}^\dagger e^{-i\omega t}), \tag{2.1}$$

where $\hat{a}$ and $\hat{a}^\dagger$ are the annihilation and creation operators, and E_0 is the unit field per mode volume. In this notation, the hat "$\hat{}$" indicates an operator, and $i = \sqrt{-1}$.

The intensity of a beam of light is directly proportional to the number of photons reaching a detector within the detection time, or the detection bandwidth. The number of photons in the field is obtained by applying the number operator to a number state, as $\hat{n}|n\rangle = n|n\rangle$, where n refers to the number of photons in state $|n\rangle$, and $\hat{n} = \hat{a}^\dagger\hat{a}$ is the Hermitian observable counting these photons. The annihilation and creation operators, $\hat{a}$ and $\hat{a}^\dagger$, are non-Hermitian ($\hat{a} \neq \hat{a}^\dagger$) and obey the bosonic commutation relation $[\hat{a}, \hat{a}^\dagger] = \hat{a}\hat{a}^\dagger - \hat{a}^\dagger\hat{a} = 1$. These operators act on the number state $|n\rangle$ to lower and raise the number of photons in the field by one, that is $\hat{a}|n\rangle = \sqrt{n}|n-1\rangle$ and $\hat{a}^\dagger|n\rangle = \sqrt{n+1}|n+1\rangle$.

In order to describe $\hat{E}$ in terms of observable quantities, we can write the annihilation operator in terms of its real and imaginary parts, as:

$$\hat{a} = \hat{X} + i\hat{Y}. \tag{2.2}$$

With this definition, the quantized electric field in Eq. (2.1) can be written as:

$$\hat{E}(t) = 2E_0\left[\hat{X}\cos(\omega t) + \hat{Y}\sin(\omega t)\right], \tag{2.3}$$

where $\hat{X}$ and $\hat{Y}$ represent the Hermitian quadrature operators for the real (in-phase) and imaginary (out-of-phase) components of the field. The field can also be visualized

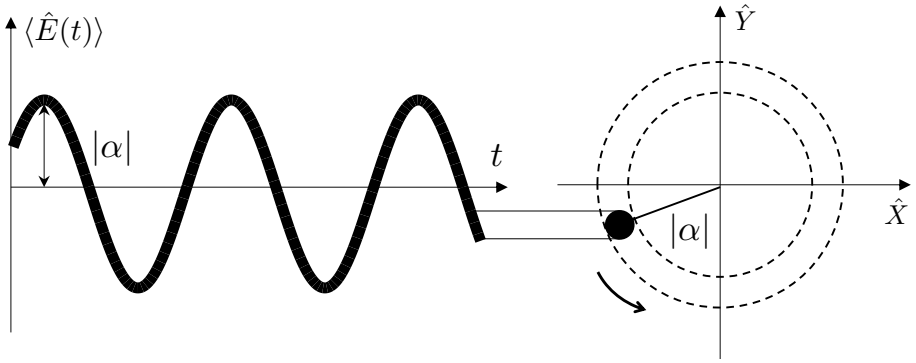

Figure 2.1: An electric field (left) can be displayed in phase-space (right) in terms of its real, $\hat{X}$, and imaginary, $\hat{Y}$, components.

in a phase space diagram, where the x- and y-axis represent the amplitude and phase quadratures of the electric field, respectively, as shown in Fig. 2.1.

Following the commutation relation between $\hat{a}$ and $\hat{a}^\dagger$, we have that $[\hat{X}, \hat{Y}] = i/2$. Therefore, the uncertainty principle, which determines the relation between the uncertainties of conjugate observables $\hat{X}$ and $\hat{Y}$, takes the form:

$$\langle \Delta^2 \hat{X} \rangle \langle \Delta^2 \hat{Y} \rangle \geq \frac{1}{16}, \tag{2.4}$$

where the uncertainty in each quadrature is given by its variance, defined as $\langle \Delta^2 \hat{X} \rangle = \langle \hat{X}^2 \rangle - \langle \hat{X} \rangle^2$. The bracket notation $\langle \rangle$ represents the expectation value of an operator, which means the statistical average of the outcomes of a series of experimental measurements. The square root of the variance represents the standard deviation of an observable $\hat{V}$, $\langle \Delta \hat{V} \rangle = \sqrt{\langle \Delta^2 \hat{V} \rangle}$.

2.1.1 Coherent State

The uncertainties of the field quadratures cannot be less than the minimum uncertainty value determined by the uncertainty principle. In general, classical states of light have uncertainties greater than the minimum uncertainty value given by the uncertainty principle. A particular case where both quadratures have equal and minimum uncertainties, $\left\langle \Delta^2 \hat{X} \right\rangle = \left\langle \Delta^2 \hat{Y} \right\rangle = 1/4$, is called a "coherent state" which represents a classical state with the least amount of noise and defines the SNL.

In operator notation, coherent states are given by displaced states from a vacuum mode, as $|\alpha\rangle = \hat{D}(\alpha)|0\rangle$, where $D(\alpha)$ is the unitary displacement operator:

$$\hat{D}(\alpha) = \exp(\alpha \hat{a}^\dagger - \alpha^* \hat{a}), \tag{2.5}$$

and $\alpha = |\alpha| e^{i\phi_\alpha}$ is the eigenvalue of the annihilation operator, $\hat{a}|\alpha\rangle = \alpha|\alpha\rangle$, and indicates the amplitude of the electric field of a coherent state as $|\alpha|$. The creation and annihilation operators are transformed by the displacement operator as $\hat{D}^\dagger(\alpha)\hat{a}\hat{D}(\alpha) = \hat{a} + \alpha$, and its adjoint as $\hat{D}^\dagger(\alpha)\hat{a}^\dagger\hat{D}(\alpha) = \hat{a}^\dagger + \alpha^*$.

In a phase space diagram, a coherent state is represented by a disk corresponding to the contour plot of the Wigner probability distribution, as shown in Fig. 2.2(a), which forms a Gaussian distribution with minimum equal uncertainties in both quadratures. A coherent state contains equal noise in both amplitude and phase of the field, as is shown in Fig. 2.3(a). By convention, we define the $\hat{X}$ and $\hat{Y}$ quadratures, as the amplitude and phase of the field, respectively*, if the amplitude of the light is large

*We use this convention throughout the thesis.

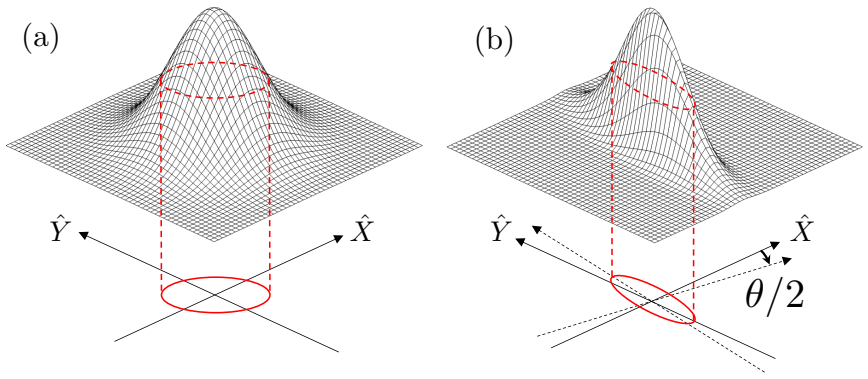

Figure 2.2: Wigner distribution of Gaussian states: (a) coherent state and (b) squeezed state. Angle θ gives the rotation of the squeezing ellipse in phase space.

enough, $|\alpha| \gg 1$. Therefore, the uncertainty area in phase space, also represents the uncertainty of amplitude and phase of the field, as shown in Fig. 2.3(a). The size of the uncertainty disk of a coherent state is the limit between classical and quantum states, such that the states with less uncertainties (noise) along any direction in phase space than a coherent state are quantum states. Therefore, for a given quadrature, the minimum uncertainty of a coherent state defines the SNL, also called the standard quantum limit if radiation pressure is negligible.

A laser beam is a close approximation to a coherent state with equal and minimum noise levels in each of its quadratures. Based on the definition of the SNL, the sensitivity of a measurement performed with a laser beam, as a classical state of the light, is limited fundamentally to the SNL achieved with a pure coherent state. A sensitivity better than this limit can only be obtained with quantum states, as those introduced in

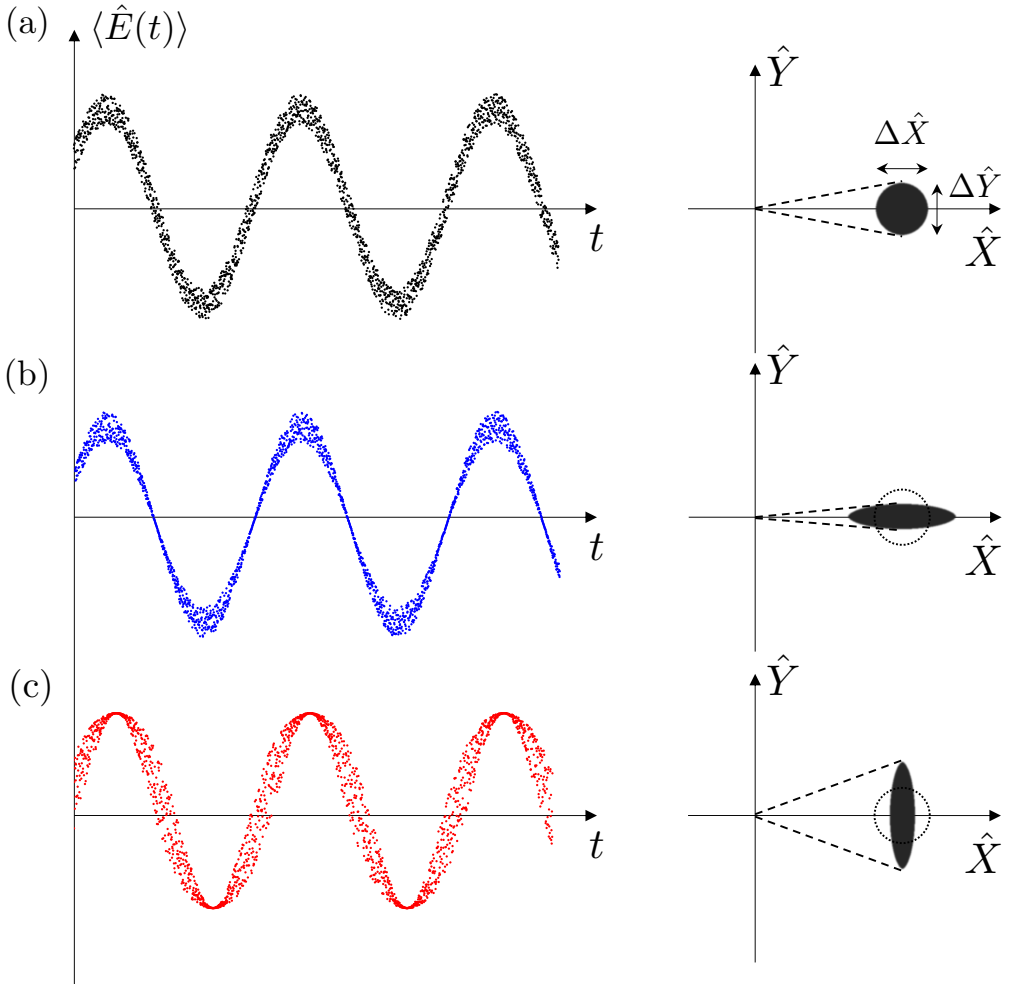

Figure 2.3: Presentation of an electric field in time (left) and in phase space (right). (a) A coherent state has equal uncertainty in both the amplitude and phase quadratures, which defines the SNL. (b) A phase-squeezed state has phase noise less than the SNL (dashed circles), but excess noise in the amplitude quadrature. (c) An amplitude-squeezed state has amplitude noise less than the SNL, but excess noise in the phase quadrature.

the following section.

2.1.2 Single Mode Squeezed State

Although the SNL is a fundamental limit for classical states of light, quantum mechanics provides a way to surpass this limit. Quantum squeezed states, as opposed to classical states, can beat the SNL by redistributing the fluctuations in conjugate components of the field. According to the uncertainty principle, a reduction in the uncertainty below the SNL can only happen in one quadrature to generate squeezing at the expense of an increase of uncertainty, anti-squeezing, in the other conjugate quadrature [50]. That means, from the uncertainty relation shown in Eq. (2.4), that the uncertainty for the quadratures of a squeezed state can be either:

$$\left\langle \Delta^2 \hat{X} \right\rangle < 1/4 \quad \text{and} \quad \left\langle \Delta^2 \hat{\mathrm{Y}} \right\rangle \geq 1/4, \tag{2.6}$$

or:

$$\left\langle \Delta^2 \hat{X} \right\rangle \geq 1/4 \quad \text{and} \quad \left\langle \Delta^2 \hat{\mathrm{Y}} \right\rangle < 1/4. \tag{2.7}$$

As shown in Figs. 2.3(b) and (c), the uncertainty area for a squeezed state is represented by an ellipse, which here is aligned with the $\hat{X}$ or $\hat{Y}$ directions. When the uncertainty in the phase quadrature is reduced below the SNL and excess noise is present in the amplitude quadrature, the state is called a phase-squeezed state, Fig. 2.3(b). On the other hand, when the uncertainty in the amplitude quadrature is reduced below the SNL and an excess noise is present in the phase quadrature, the state is called an amplitude-squeezed state, Fig. 2.3(c). Using squeezed states for detection purposes, if

the measurement is only sensitive to the amplitude (phase) of the light, we can benefit from the reduced noise property of an amplitude (phase) squeezed state.

Squeezed states are non-classical (quantum) states due to the fact that the uncertainty of one of their quadratures falls below the SNL. Additionally, due to the field quantization and the commutation relation between the field quadratures, squeezed states require a non-positive Glauber-Sudarshan P distribution [36], which is an indication of their quantum nature.

A bright quadrature squeezed state is mathematically defined as:

$$|\alpha, \zeta\rangle = \hat{D}(\alpha)\hat{S}(\zeta)|0\rangle, \tag{2.8}$$

where $\hat{S}(\zeta)$ is the squeezing operator that shrinks a quadrature while amplifying the other one, and the displacement operator makes it bright. Alternatively, we can also generate bright squeezed states with a reversed ordering of the operators than the one presented in Eq. (2.8). In that case, the displacement operator first generates a bright coherent state, then the squeezing operator generates a coherent squeezed state [6, 48]. These two approaches are related to each other, and can lead to the same results with proper transformations [44].

The unitary squeezing operator is defined as:

$$\hat{S}(\zeta) = \exp\left[\frac{1}{2}(\zeta^* \hat{a}^2 - \zeta \hat{a}^{\dagger 2})\right], \tag{2.9}$$

where $\zeta = se^{i\theta}$ is the complex squeezing parameter. Here s represent the magnitude of squeezing parameter. Moreover, θ indicates the phase of squeezing operator, and the rotation of the noise ellipse with respect to the $\hat{X}$ quadrature in phase space is given by

$\theta/2$. Generally, the noise ellipse of a squeezed state can be rotated to show squeezing along a superposition of phase and amplitude quadratures, as shown in Fig. 2.2(b).

2.1.3 Two-Mode Squeezed State: Twin Beams

The squeezing operator contains terms proportional to $\hat{a}^2$ and $\hat{a}^{\dagger 2}$, pointing to the fact that in a squeezing process photons are absorbed and created in pairs. If the generated photon-pairs are indistinguishable, the outcome state is a single mode squeezed state in which the photon pairs are generated in a single beam of light. The generation of photon pairs can be generalized to more than one mode, leading to higher order squeezed states. For example, when the photon pairs are distinguishable, such that one can separate them into two isolated beams, generating the TMSS, also known as twin beams [51]. In this thesis, we are interested in the study of these states for quantum sensing applications.

A bright TMSS is described by:

$$|\alpha, \beta; \zeta\rangle = \hat{D}_a(\alpha)\hat{D}_b(\beta)\hat{S}_{a,b}(\zeta)|0, 0\rangle, \tag{2.10}$$

where α and β are the complex amplitudes of the two coherent modes of light, $\hat{a}$ and $\hat{b}$. The two mode squeezing operator:

$$\hat{S}_{a,b}(\zeta) = \exp(\zeta^* \hat{a}\hat{b} - \zeta \hat{a}^\dagger \hat{b}^\dagger), \tag{2.11}$$

mixes the two input modes of light*, in such a way that two photons are simultaneously absorbed from (or generated into) these two modes of light. Similar to the single mode

*Operators $\hat{a}$ and $\hat{b}$ represent the annihilation operators for these two modes.

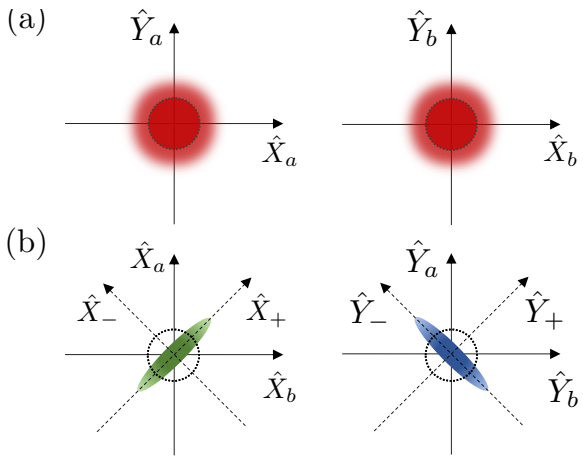

Figure 2.4: Phase space representation of a TMSS. (a) The quadratures of each mode of the TMSS show excess noise. Dotted circles indicate the SNL. (b) The joint sum and difference quadratures of a TMSS are squeezed. Reproduced from [52]

squeezed state, the order of squeezing and the displacement operators in Eq. (2.10) can be swapped with appropriate relation factors. As will be explained later, we experimentally generate a TMSS by applying the squeezing operator to a coherent state. In particular, for generating a bright TMSS, the squeezing process is seeded by a bright coherent state, rather than a vacuum mode. Moreover, the annihilation and creation operators undergo the following unitary transformations by the two mode squeezing operator:

$$\begin{aligned} \hat{S}_{a,b}^{\dagger}\hat{a}\hat{S}_{a,b} &= \hat{a}\cosh(s) - \hat{b}^{\dagger}e^{i\theta}\sinh(s), \\ \hat{S}_{a,b}^{\dagger}\hat{b}\hat{S}_{a,b} &= \hat{b}\cosh(s) - \hat{a}^{\dagger}e^{-i\theta}\sinh(s). \end{aligned} \tag{2.12}$$

As the squeezing operator mixes the photons from the two modes of light, we can

define joint quadratures from the four quadratures of the two modes as:

$$\hat{X}_{\pm} = \frac{1}{\sqrt{2}}(\hat{X}_a \pm \hat{X}_b) \quad \text{and} \quad \hat{Y}_{\pm} = \frac{1}{\sqrt{2}}(\hat{Y}_a \pm \hat{Y}_b), \tag{2.13}$$

with the commutation relations given by:

$$[\hat{X}_{\pm}, \hat{Y}_{\pm}] = i/2 \quad \text{and} \quad [\hat{X}_{\pm}, \hat{Y}_{\mp}] = 0. \tag{2.14}$$

As a result, the joint quadratures $\hat{X}_-$ and $\hat{Y}_+$ (and $\hat{X}_+$ and $\hat{Y}_-$) can be squeezed simultaneously in a two-mode squeezed state. As shown in Fig. 2.4, while both quadratures of each mode are noisier than the SNL, the quantum correlations between the two modes, due to the simultaneous generation of photons in pair, lead to a decrease in the amplitude difference quadrature, $\hat{X}_-$, and an increase in the variance of its joint quadrature, the phase difference quadrature $\hat{Y}_-$. Or similarly, when the phase sum quadrature $\hat{Y}_+$ is squeezed, the amplitude sum quadrature $\hat{X}_+$ contains excess noise. Therefore, the squeezing is distributed across the quadratures of the two distinguishable modes, and hence its name is called a twin beam.

2.2 Nonlinear Process to Correlate Photons

The pair photon production needed for the generation of a TMSS is described by a nonlinear Hamiltonian of the form:

$$\hat{H} = \hbar[\chi^{(n)}\hat{a}\hat{b} + \chi^{(n)}\hat{a}^{\dagger}\hat{b}^{\dagger}], \tag{2.15}$$

which leads to the two-mode squeezing operator. In this Hamiltonian, $\chi^{(n)}$ is the nonlinear susceptibility of the medium. For a single mode squeezed state, both modes

in Eq. (2.15) are degenerate, $\hat{a} = \hat{b}$. A nonlinear process deforms the noise distribution of a coherent state by introducing different gains for different quadratures of the field. This deformation of the noise through a nonlinear light-matter interaction can reduce the amplitude (or phase) noise in the generated photons [53].

We can see how a nonlinear process leads to pair photon generation by studying the response of a nonlinear material to the interacting fields of light. The electric response of a medium is described by its electric dipole moments per unit volume:

$$P(\vec{r},t) = \epsilon_0 \left[\chi^{(1)}E(\vec{r},t) + \chi^{(2)}E^2(\vec{r},t) + \chi^{(3)}E^3(\vec{r},t) + \ldots\right], \tag{2.16}$$

where ϵ_0 is the vacuum permittivity. The first term on the right hand side of Eq. (2.16) is the linear response of the material, as it is proportional to the E-field linearly. When the intensity of the light is strong enough, or the nonlinear coefficients of the material are large enough, higher order terms of the nonlinear response of the medium become significant and lead to interesting phenomena.

From Maxwell equations, we can obtain the wave equation for the propagation of an electromagnetic wave in the medium coordinate $\vec{r}$ and time t:

$$\nabla^2 E(\vec{r},t) - \frac{1}{c^2}\frac{\partial^2 E(\vec{r},t)}{\partial t^2} = \frac{1}{\epsilon_0 c^2}\frac{\partial^2 P(\vec{r},t)}{\partial t^2}, \tag{2.17}$$

where c is the speed of light in vacuum and ϵ_0 is the permittivity of vacuum. Substituting the polarization from Eq. (2.16), we obtain*:

$$\nabla^2 E(\vec{r},t) - \frac{\epsilon^{(1)}}{c^2}\frac{\partial^2}{\partial t^2}E(\vec{r},t) = \frac{1}{\epsilon_0 c^2}\frac{\partial^2 P^{\mathrm{NL}}(\vec{r},t)}{\partial t^2}, \tag{2.18}$$

*In this thesis, we ignore the magnetic response, $\mu = \mu_0$.

where $\epsilon^{(1)} = \epsilon_0 \chi^{(1)}$ is the relative permittivity which depends on the linear response of the medium electric polarization, and P^{NL} refers to the nonlinear terms in the polarization Eq. (2.16). The right hand side of this inhomogeneous wave equation acts as a source for the electromagnetic wave propagation in the medium. Therefore, the nonlinear response of the medium makes it possible to produce new frequencies as a result of the light-matter interaction.

The $\chi^{(2)}$ nonlinear term of the polarization acts as the source for second-order nonlinear processes, such as optical parametric amplification (OPA) and second harmonic generation (SHG). It only occurs in nonlinear crystals that do not show inversion symmetry (noncentrosymmetric). On the other hand, third order nonlinear effects, such as third harmonic generation (THG), the Kerr effect, and four-wave mixing (FWM), can occur in materials with nonzero $\chi^{(3)}$ susceptibility, regardless of their inversion symmetry [54]. Both of these nonlinear orders show up in the same Hamiltonian described with Eq. (2.15), and can be used for generating squeezed light. In this thesis, we only focus on the FWM process.

2.2.1 Four-Wave Mixing in Rubidium Atoms

Due to the inversion symmetry of atoms, even orders of susceptibility, including $\chi^{(2)}$, vanish, and the most dominant nonlinear response of the medium becomes $\chi^{(3)}$. It means that the third order nonlinear response of atoms can mix different modes of light. As shown in Fig. 2.5(a), a $\chi^{(3)}$ medium allows mixing of the three input fields for the generation of a fourth field. Here, we refer to the two photons in the stronger mode

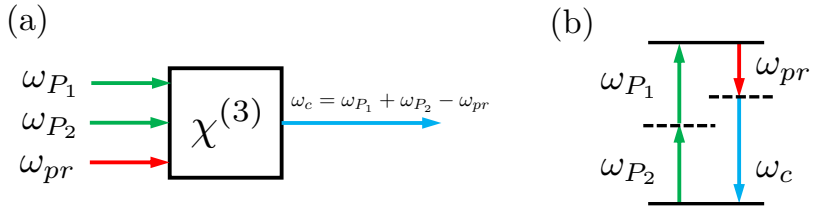

Figure 2.5: (a) A $\chi^{(3)}$ medium allows an ideal FWM process, which couples three waves to generate a new fourth field. (b) A four-level atom allows the absorption and emission of photons in pairs.

as pumps (ω_{P1}, ω_{P2}). The two other modes are called the probe (ω_{pr}) and conjugate, (ω_c). A four-level atomic system is capable of hosting the FWM process, as shown in Fig. 2.5(b).

All frequency components of the interacting fields satisfy the wave equation (2.18). That means, if we write the field components as $E(\vec{r},t) = A(\vec{r},t)e^{i(\vec{k}\cdot\vec{r}-\omega t)}$, the wave equation satisfies:

$$\frac{dA_j}{dz} = i\frac{\omega_j}{2\epsilon_0 n_j c}P(\omega_j)e^{-ik_j z}, \tag{2.19}$$

In this equation, A_j is the slowly-varying amplitude of the field, ϵ_0 is the permittivity and c is the speed of light in vacuum, and k_j, ω_j, and n_j are the wavevector, frequency, and refractive index, and $P(\omega_j)$ is the nonlinear polarization of the medium. Each mode is labeled by subscript $j = P_1, P_2, pr, c$, for the two pumps P_1 and P_2 and the probe and conjugate modes pr and c, respectively. The nonlinear polarization $P(\omega_j)$, is the driving term of Eq. (2.19) which leads to the excitation of fields in the nonlinear

medium, and is given by:

$$P_j^{\mathrm{NL}} \propto \chi^{(3)} \omega_j A_i A_j A_k^* e^{i(k_i + k_j - k_k)z}, \tag{2.20}$$

for all permutations of j, j, k subscripts.

Under the rotating-wave approximation, we can eliminate the time dependence of the wave equation, leading to:

$$\omega_{P_1} + \omega_{P_2} = \omega_{pr} + \omega_c, \tag{2.21}$$

which is the energy conservation for the FWM process. In particular, the propagation equation for the conjugate mode simplifies as:

$$\frac{dA_c}{dz} \propto i\chi^{(3)} A_{P_1} A_{P_2} A_{pr}^* e^{i\Delta k z}. \tag{2.22}$$

Similarly, we can write the wave equations for the coupled-amplitudes of the other three components of the field. In Eq. (2.22), $\Delta k = (k_{P_1} + k_{P_2} - k_{pr} - k_c)$ represents the relation between the momentum components of the four field wavevectors and is referred to as the "phase-matching condition". It means that the FWM occurs most efficiently when the momentum vectors satisfy $\Delta k = 0$. We will revisit this condition in section 2.4.

Under an undepleted pump approximation, which can be satisfied when implementing the FWM process with intense pump beams, we can assume that the A_{P_1} and A_{P_2} modes stay constant, i.e. $(dA_{P_1}/dz) = (dA_{P_2}/dz) = 0$. Therefore, we have the following

coupled-amplitude wave equations for the probe and conjugate modes:

$$\frac{dA_{pr}}{dz} = i\chi^{(3)} I_P A_c^*, \tag{2.23}$$

$$\frac{dA_c}{dz} = i\chi^{(3)} I_P A_{pr}^*, \tag{2.24}$$

where $I_P \propto A_{P_1} A_{P_2}$ is a constant that depends on the intensity of the pump modes. Therefore, the FWM process couples the probe and conjugate photons through the $\chi^{(3)}$ nonlinearity of the material when intense pump beams are used. Moreover, when the photons of the probe mode seed the FWM process, the stimulate the process to generate bright probe and conjugate beams.

2.2.2 Experimental Setup for Generating Twin Beams

Here, we discuss the generation of twin beams from a FWM process in the D1 line of ^{85}Rb atoms in a hot vapor cell. A scheme of the experimental setup is shown in Fig. 2.6(a), where the process is pumped with a strong pump beam from a Titanium-Sapphire laser at the wavelength of $\lambda = 795$ nm. As shown in Fig. 2.6(b), the D1 line of ^{85}Rb atoms represents the transition between levels $5^2S_{1/2}$ and $5^2P_{1/2}$. The hyperfine splitting is 3.035 GHz for the ground states and 361 MHz for the excited states. Due to the effect of Doppler broadening in a vapor cell, the hyperfine structure of the excited level cannot be resolved with a simple absorption spectroscopy, and requires saturation absorption spectroscopy (SAS). We use a SAS setup (not shown here) to measure the absolute frequency of the laser beams and their detuning from atomic level transitions.

As shown by green lines in Fig. 2.6, the two pump photons are generated from a

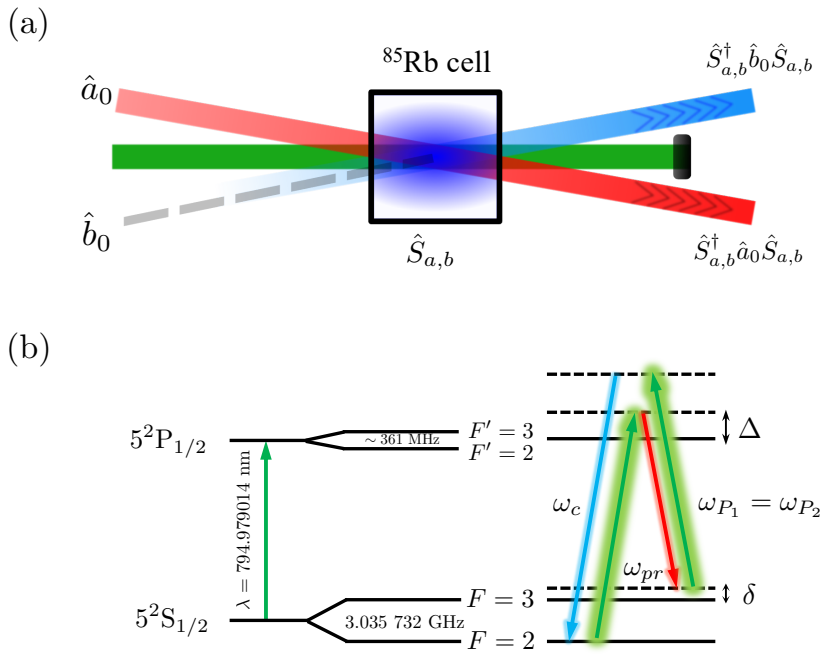

Figure 2.6: (a) Schematic for the FWM experiment. (b) Hyperfine energy levels of ^{85}Rb D1 line (left) used in the FWM process with a double-Λ configuration (right). Δ: one-photon detuning, δ: two-photon detuning. Color code: green: pump, red: probe, blue: conjugate, gray dashed line: vacuum mode.

single intense beam, $\omega_{P_1} = \omega_{P_2}$. By sending the strong pump beam to the Rb vapor cell, pairs of photons are generated through a spontaneous FWM process, to generate vacuum two-mode squeezed state (VTMSS). To generate bright two-mode squeezed states of light (BTMSS), we seed the FWM process with photons at the frequency of the probe beam. The seeding beam is generated by taking a small fraction of the pump beam using a beam sampler. This portion double-passes an accousto-optical modulator (AOM) to red-detune it by 2×1.52 GHz. By seeding the FWM process, pairs of the probe and conjugate photons are generated as a result of a stimulated FWM process: the seeded probe beam is amplified and a new conjugate beam emerges [55].

The efficiency of the FWM process in converting energy from the pump photons to the quantum correlated twin beams depends on the strength of the $\chi^{(3)}$ nonlinearity in the Rb atoms. Large nonlinearities occur when the pump frequency is tuned on-resonance with an atomic transition. However, on-resonance transitions increase unfavorably the absorption and spontaneous emission rates, both of which reduce the coherency of the light-matter interaction and act as loss mechanisms. To overcome these effects and extract a large nonlinear response from the atoms, we use a double-Λ configuration to generate bright squeezed states with high intensity naturally from the atomic interaction [56, 57, 58, 59]. To prevent atomic absorption, the pump frequency is detuned from the $F = 3$ of the $5^2S_{1/2}$ ground level to the $5^2P_{1/2}$ excited level, called the single-photon detuning as is indicated by Δ in Fig. 2.6(b).

The efficiency and gain of the FWM process determines the amount of quantum-correlations between the generated twin beams. As will be discussed in section 2.3.1, the

quantum correlations between twin beams are characterized by measuring the level of noise-reduction, or squeezing, between them. There are several important experimental parameters that need to be optimized to obtain the best squeezing. For example, the density of the Rb atoms involved in the FWM interaction, which can be controlled by the temperature of the Rb vapor cell, the coupling of the atomic transition, which is defined by the pump's size and power, the single-photon detuning Δ, the relative pump and probe detuning δ (two-photon detuning), and their angle of overlap inside the Rb cell, to name a few. Depending on the specific application for the temporal or spatial distribution of the squeezed photons, these parameters are optimized at different values, as will be described in chapters 5 and 6.

2.3 Detection Methods

The quantum correlations between the twin beams produced from the FWM can be characterized by choosing an appropriate detection method. The simplest measurement consists of a differential measurement between the photocurrents of the photodetectors used to measure the twin beams. With this method, we can cancel the common classical and quantum noise between the twin beams and measure the noise reduction with respect to the SNL. However, obtaining more information about the quantum properties of the twin beams, such as the quadrature squeezing, the level of entanglement, and the pureness of the generated states, require more elaborate techniques for state detection, such as a homodyne measurement.

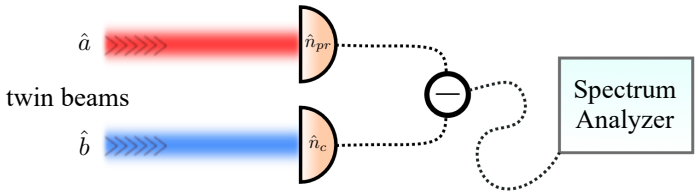

Figure 2.7: Intensity-difference measurement for twin beams. Photodetectors measure the intensity (proportional to the number of photons) in each mode. A spectrum analyzer is used to obtained the noise power spectrum of the difference signal from the two photodetectors.

2.3.1 Intensity-Difference Detection

An intensity-difference (ID) measurement is performed by subtracting the photocurrents of two independent photodetectors and then analyzing the noise of the difference signal on an spectrum analyzer (SA) [60], as shown in Fig. 2.7. The outcome of such measurement is given by:

$$\hat{M} = \hat{n}_{pr} - \hat{n}_c, \tag{2.25}$$

where $\hat{n}_{pr} = \hat{a}^\dagger \hat{a}$ and $\hat{n}_c = \hat{b}^\dagger \hat{b}$, are the photon number operators indicating the intensity of the two modes under study. Here, these modes are the probe ($\hat{a}$) and conjugate ($\hat{b}$) beams from the twin beams. The uncertainty (noise) of the ID between the twin beam is obtained by calculating the variance of measurement $\hat{M}$, as:

$$\begin{aligned} \left\langle \Delta^2 \hat{M} \right\rangle &= \left\langle (\hat{n}_{pr} - \hat{n}_c)^2 \right\rangle - \left(\left\langle \hat{n}_{pr} - \hat{n}_c \right\rangle \right)^2, \\ &= \left\langle \Delta^2 \hat{n}_{pr} \right\rangle + \left\langle \Delta^2 \hat{n}_c \right\rangle - 2 \left[\left\langle \hat{n}_{pr} \hat{n}_c \right\rangle - \left\langle \hat{n}_{pr} \right\rangle \left\langle \hat{n}_c \right\rangle \right], \end{aligned} \tag{2.26}$$

where the last term is the covariance (*cov*) between the two measured beams, and is determined by the correlation between them.

When the two beams under study are coherent states, there is no correlation between them and the covariance term vanishes. The noise of the ID for two uncorrelated coherent state of light is the sum of the noise of the individual beams. This noise level for the coherent states, $\left\langle \Delta^2 \hat{M} \right\rangle_{\mathrm{CS}}$, defines the SNL. On the other hand, if the two input beams are probe and conjugate modes from a FWM process, the covariance term is non-zero and the noise of the ID measurement, $\left\langle \Delta^2 \hat{M} \right\rangle_{\mathrm{TB}}$, is reduced below the noise of the SNL, leading to the measurement of squeezing.

Since we are interested in calculating the variance of an ID measurement for the twin beams, we use the unitary transformations performed by the squeezing and displacement operators. For example, to calculate the mean value an arbitrary operator $\hat{O}$, we use:

$$\begin{aligned}\left\langle \hat{O} \right\rangle &= \langle \alpha, \beta, \zeta | \hat{O} | \alpha, \beta, \zeta \rangle \\ &= \langle 0,0 | \hat{D}_b^\dagger(\beta) \hat{D}_a^\dagger(\alpha) \hat{S}_{a,b}^\dagger(\zeta) \hat{O} \hat{S}_{a,b}(\zeta) \hat{D}_a(\alpha) \hat{D}_b(\beta) | 0,0 \rangle. \end{aligned} \tag{2.27}$$

If both modes are seeded with coherent states $\alpha = |\alpha| e^{i\phi_\alpha}$ and $\beta = |\beta| e^{i\phi_\beta}$, the mean values of each beam is given by:

$$\begin{aligned}\left\langle \hat{n}_{pr} \right\rangle =& |\alpha|^2 \cosh^2(s) + |\beta|^2 \sinh^2(s) \\ & - 2|\alpha\beta| \cos(\psi) \sinh(s) \cosh(s) + \sinh^2(s), \end{aligned} \tag{2.28}$$

$$\begin{aligned}\left\langle \hat{n}_{c} \right\rangle =& |\beta|^2 \cosh^2(s) + |\alpha|^2 \sinh^2(s) \\ & - 2|\alpha\beta| \cos(\psi) \sinh(s) \cosh(s) + \sinh^2(s), \end{aligned} \tag{2.29}$$

where $\psi = (\theta - \phi_\alpha - \phi_\beta)$, with θ the phase of the two-mode squeezing operator, $\zeta = se^{i\theta}$. Similarly, the uncertainty of each mode by itself is:

$$\begin{aligned}\left\langle \Delta^2 \hat{n}_{pr} \right\rangle = &\left[|\alpha|^2 \cosh^2(s) + |\beta|^2 \sinh^2(s) + 2|\alpha\beta| \cos(\psi) \sinh(s) \cosh(s)\right] \times \\ &\left[\cosh^2(s) + \sinh^2(s)\right] + \sinh^2(s) \cosh^2(s), \end{aligned} \tag{2.30}$$

$$\begin{aligned}\left\langle \Delta^2 \hat{n}_{c} \right\rangle = &\left[|\beta|^2 \cosh^2(s) + |\alpha|^2 \sinh^2(s) + 2|\alpha\beta| \cos(\psi) \sinh(s) \cosh(s)\right] \times \\ &\left[\cosh^2(s) + \sinh^2(s)\right] + \sinh^2(s) \cosh^2(s). \end{aligned} \tag{2.31}$$

In Eqs. (2.28)–(2.31), the terms which are multiplied by the seeding field α and β, represent the stimulated emission of photons from the FWM process. On the other hand, even when there is no seeding, $\alpha = \beta = 0$, there still exist nonzero means and variances of the photon numbers, representing the spontaneous emission of photons from the FWM process. Throughout the rest of this thesis, we focus on the case where only the probe beam is seeded with a bright coherent state, $|\alpha| \gg 1$, and the conjugate mode is seeded with a vacuum mode, $|\beta| = 0$. This means that the FWM process becomes insensitive to the relative phase between the seeding beams and the squeezing operator, i.e. ψ, as can be seen from Eqs. (2.28)–(2.31). Then, the mean values of the probe and conjugate photon number simplify to:

$$\left\langle \hat{n}_{pr} \right\rangle = |\alpha|^2 \cosh^2(s), \tag{2.32}$$

$$\left\langle \hat{n}_{c} \right\rangle = |\alpha|^2 \sinh^2(s), \tag{2.33}$$

where we ignore the $\sinh^2(s)$ term for the photons emitted spontaneously, as we assume $|\alpha| \gg 1$. These results clearly show the amplification of the seeded probe beam and the

generation of the conjugate beam. Therefore, the gain of the input seed probe due to the FWM is given by $g = \cosh^2(s)$. The uncertainties of the two modes also simplify to:

$$\left\langle \Delta^2 \hat{n}_{pr} \right\rangle = |\alpha|^2 \cosh^2(s) \left[\cosh^2(s) + \sinh^2(s) \right], \tag{2.34}$$

$$\left\langle \Delta^2 \hat{n}_{c} \right\rangle = |\alpha|^2 \sinh^2(s) \left[\cosh^2(s) + \sinh^2(s) \right]. \tag{2.35}$$

Moreover, due to the emission of photons in pairs, the twin beams have a non-zero covariance, given by:

$$cov = \left\langle \hat{n}_{pr} \hat{n}_{c} \right\rangle - \left\langle \hat{n}_{pr} \right\rangle \left\langle \hat{n}_{c} \right\rangle = 2|\alpha|^2 \cosh^2(s) \sinh^2(s). \tag{2.36}$$

Using Eq. (2.26), the variance of the ID between the twin beam becomes:

$$\left\langle \Delta^2 \hat{M} \right\rangle_{\mathrm{TB}} = |\alpha|^2, \tag{2.37}$$

which means that, for an ideal TMSS with perfect quantum correlation, the common noise between the twin beam can be canceled with an ID measurement, while only the noise of the input seeding coherent state remains.

To characterize the amount of noise reduction with the twin beams, we calculate the noise of an equal measurement but with pure coherent states to determine the SNL. That means, we replace the probe and conjugate beams from the twin beam with two coherent states of the same optical power. For coherent states, the mean and the variance are equal, as can be seen from Eqs. (2.32) and (2.34), for example, when $s = 0$. Therefore, we calculate the noise of two coherent states of the same optical power as the twin beams given by the mean values in Eqs. (2.32) and (2.33).

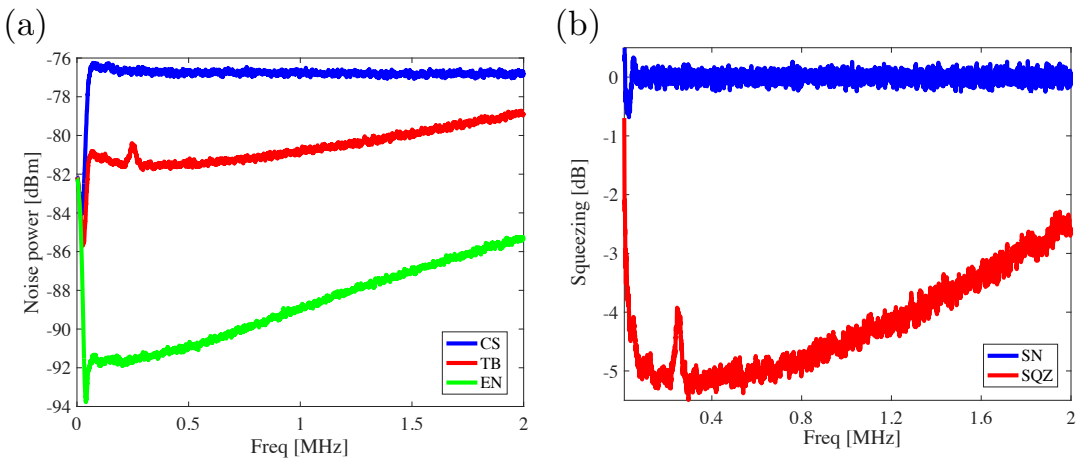

Figure 2.8: Typical squeezing traces in an ID measurement. (a) Noise power spectrum for coherent states (CS), twin beams (TB), and electronic noise of the detectors (EN). (b) Absolute squeezing obtained after subtracting EN and normalizing the twin beam ID noise to the SNL.

The level of squeezing is measured by taking the ratio of the relative noise in the twin beam to the noise of a coherent state with equal power as the probe and the conjugate beams:

$$R_{\text{lin}} = \frac{\left\langle \Delta^2 \hat{M} \right\rangle_{\text{TB}}}{\left\langle \Delta^2 \hat{M} \right\rangle_{\text{CS}}} = \frac{1}{\sinh^2(s) + \cosh^2(s)}. \tag{2.38}$$

This result can also be written in terms of the gain of the FWM as $R_{\text{lin}} = 1/(2g-1)$, which clearly shows the noise reduction in the twin beam compared to the coherent state when $g > 1$. We usually report the squeezing in log-scale:

$$R_{\text{log}}[\text{dB}] = 10 \log\left(R_{\text{lin}}\right). \tag{2.39}$$

Some typical experimental results demonstrating the noise of the twin beams with respect to the noise of the coherent states with an ID measurement are shown in Fig. 2.8.

As we have seen, an ID measurement allows us to cancel the common technical classical noise as well as the quantum correlated noise in the twin beams, and provides a simple and efficient method to perform quantum-enhanced measurements. Moreover, since it's technically hard to have a perfect coherent state, the cancellation of classical noise in an ID technique makes it possible to reach the SNL with a classical state of light from a laser beam. Another advantage of an ID measurement for our quantum sensing application is that, as we will see in chapter 5, it can be used in optical readout sensors to detect changes in the intensity of the probing light. However, an ID measurement is not sensitive to the quadratures of two measured fields. Such measurements require a phase-sensitive technique, such as the homodyne method, which will be described in section 2.3.5.

2.3.2 Optical Losses

In an experimental setup, the detection and optical elements are not ideal and optical losses are inevitable. In quantum mechanics, optical losses are modeled with a beam splitter (BS) with an unused input port. As shown in Fig. 2.9, the input state enters from the left port and exits from the transmitted port (on the right) with not only a reduced amplitude, but also with the addition of a vacuum mode that enters from the unused port of the beam splitter. The vacuum mode $\hat{a}_v$ couples with the input mode $\hat{a}$, as:

$$\hat{a}_{\text{out}} = \sqrt{t}\hat{a} + \sqrt{r}\hat{a}_v, \tag{2.40}$$

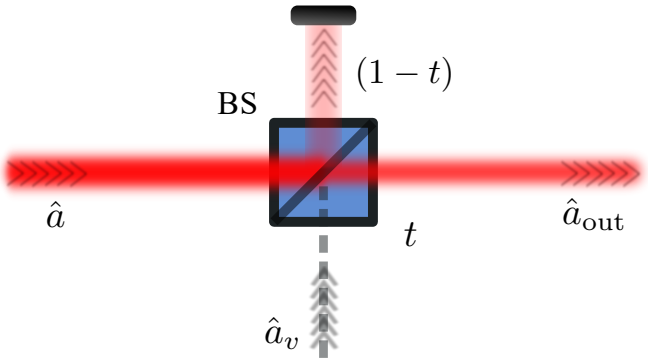

Figure 2.9: Optical loss can be modeled with a beam splitter (BS), which couples a vacuum mode with the input mode.

where t and $r = (1-t)$ are the intensity transmission and reflection coefficients for the beam splitter.

To calculate the effect of optical losses on the level of squeezing obtained with an ID measurement, we model losses on the twin beam after the FWM using beam splitters in the probe and conjugate arms with intensity transmissions η_{pr} and η_c, respectively. That is, the losses in each arm are given by $(1-\eta_{pr})$ and $(1-\eta_c)$. These beam splitters represent all the losses in the optical elements from the source to the detectors, as well as the detectors inefficiencies, combined. Therefore, by generalizing previous results to include the vacuum modes coupled due to the losses, the noise of the twin beams on an ID measurement will be given by:

$$\begin{aligned}\left\langle \Delta^2(\hat{n}_{pr} - \hat{n}_c) \right\rangle =& \eta_{pr}^2 |\alpha|^2 \cosh(2s) + 2\eta_c^2 |\alpha|^2 \sinh^4(s) \\ & - 2\eta_{pr}\eta_c |\alpha|^2 \cosh(2s) + |\alpha|^2 \left[\eta_{pr} \cosh^2(s) + \eta_c \sinh^2(s)\right], \end{aligned} \tag{2.41}$$

where we assume seeding only the probe beam $|\alpha| \gg 1$ and ignore the spontaneously

emitted photons. The level of squeezing then becomes:

$$R_{\text{lin}}^{\text{loss}} = 1 + \frac{2\eta_c^2 \sinh^4(s) + 2\sinh^2(s)\cosh^2(s)(\eta_{pr}^2 - 2\eta_{pr}\eta_c)}{\eta_{pr}\cosh^2(s) + \eta_c \sinh^2(s)}. \tag{2.42}$$

Compared to the case of no losses, Eq. (2.38), the noise-reduction of the twin beam is degraded. The effect of loss can be partially compensated by optically or electronically balancing the twin beam noise to find the optimum noise cancellation.

2.3.3 Optimized Measurements of Squeezing in Presence of Optical Losses

The optical losses in the twin beam result in an imbalance of the noise and the optical power between probe and conjugate. Moreover, losses in the twin beams reduce the quantum correlations between the photons. Therefore, the presence of optical losses prevents the efficient common noise cancellation and leads to obtaining less squeezing. By introducing extra optical losses on the beam with more intensity, we can recover some of the initial squeezing and improve the squeezing measurement. As we can see in Fig. 2.10(a), even when there is no optical loss in the conjugate beam ($\eta_c = 1$), we can enhance the noise cancellation and therefore the level of squeezing by introducing some optical losses to the probe beam. This is because the probe beam is amplified during the FWM process to $g|\alpha|^2$ from a seeded beam $|\alpha|^2$, and is brighter than the unseeded conjugate beam, $(g-1)|\alpha|^2$. Therefore, by inserting some losses to the beam with more intensity, we can improve the squeezing measurement.

When there are some losses in the conjugate beam, for example $\eta_c = 0.85$ as shown in Fig. 2.10(b), the optimum squeezing is obtained when there are losses in the probe

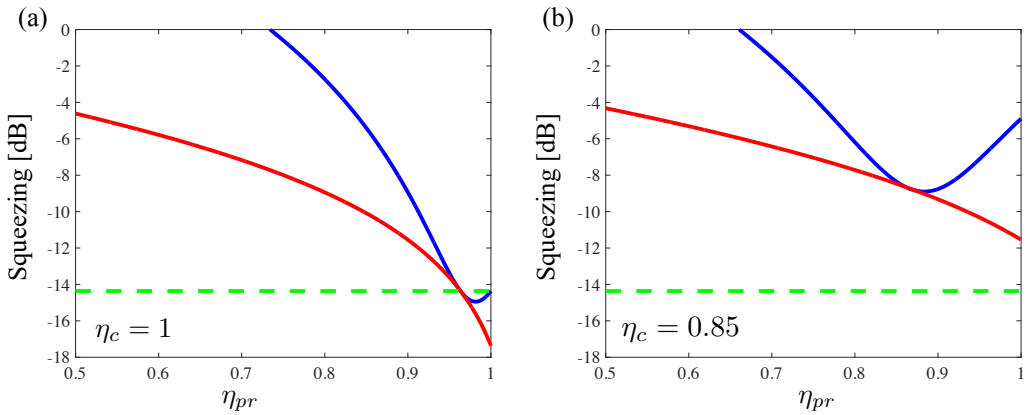

Figure 2.10: Squeezing in an ID measurement as a function of optical losses in probe beam for (a) $\eta_c = 1$, and (b) $\eta_c = 0.85$. blue trace: R_{loss}, red trace: optimum $R_{\text{loss}}^{\text{EA}}$, dashed green: initial squeezing level without optical losses ($s = 2$). Due to the imbalance in twin beams power, even without losses ($\eta_{pr} = \eta_c = 1$), we can obtain better squeezing levels with inserting optical losses in the beam with more power (probe beam here). Inserting an EA always reaches better squeezing.

beam to have the intensity transmission of the probe beam becomes almost balanced with the intensity of the conjugate beam. This leads to measuring the best squeezing at $\eta_{pr} \approx 0.8$. However, for large imbalances in losses between the twin beams, the ID measurement leads to excess noise, even above the SNL.

For a particular case when the losses in the twin beam are the same, $\eta_{pr} = \eta_c = \eta$,

the measured squeezing becomes:

$$\begin{aligned} R_{\text{lin}}^{\text{balanced loss}} &= 1 + \eta \frac{2\sinh^2(s)}{\cosh^2(s) + \sinh^2(s)} \\ &= \eta \left(\frac{1}{\cosh^2(s) + \sinh^2(s)} \right) + (1 - \eta) \\ &= \eta R_{\text{lin}} + (1 - \eta), \end{aligned} \tag{2.43}$$

where R_{lin}, is the noise reduction between the twin beams with respect to the SNL without losses, as defined in Eq. (2.38). The first term in Eq. (2.43) indicates the intensity transmissions of the initial squeezed states through the two BSs, while the second term indicates the noise of the vacuum mode which is coupled into the measurement. The noise of these two uncorrelated modes adds in quadrature in the final measurement, weighted by the intensity transmission or reflection of each mode.

While inserting optical loss can recover some of the initial squeezing, these losses couple vacuum noise into the field that introduces extra noise in the measurement. If we are able to modify the electronics of individual detectors to change their gain, we can optimize the noise cancellation between the twin beams without the added vacuum noise.

Since an amplifying gain ($G > 1$) requires an active electronic amplifier that can add extra noise to the measurement, we insert an electronic attenuation ($G < 1$) to the photocurrent of the detector which has suffered less from optical losses. Electronic attenuation (EA) can be performed with passive electronic elements that do not add extra noise to the measurement. If we assume we have more optical loss on the probe beam, we insert the EA to the conjugate detector, as shown by G in Fig. 2.11.

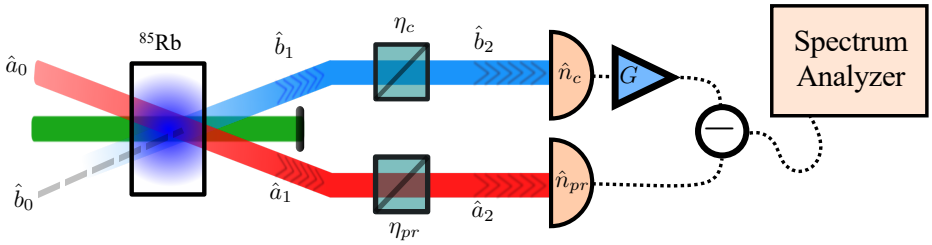

Figure 2.11: Optimum ID measurement. Optical losses for measuring squeezing of twin beams can be partially compensated either optically or electronically. G: EA.

The variance of the ID measurement with this EA, that is $\hat{M} = (\hat{n}_{pr} - G\hat{n}_c)$, then becomes:

$$\langle \Delta^2 \hat{M} \rangle^{\text{ID}} = \langle \Delta^2 \hat{n}_{pr} \rangle' + G^2 \langle \Delta^2 \hat{n}_c \rangle' - 2G[cov]', \tag{2.44}$$

where the prime notation indicates the measurements of noise and mean values with optical loss. These values can be calculated as:

$$\langle \Delta^2 \hat{n}_{pr} \rangle' = \eta_{pr}^2 \langle \Delta^2 \hat{n}_{pr}^0 \rangle + \eta_{pr}(1 - \eta_{pr}) \langle \hat{n}_{pr}^0 \rangle, \tag{2.45}$$

$$\langle \Delta^2 \hat{n}_c \rangle' = \eta_c^2 \langle \Delta^2 \hat{n}_c^0 \rangle + \eta_c(1 - \eta_c) \langle \hat{n}_c^0 \rangle, \tag{2.46}$$

$$[cov]' = \eta_{pr}\eta_c [cov]^0, \tag{2.47}$$

where the zero superscript indicates the initial mean and variances of the twin beams right after the FWM and without optical losses, as defined in Eqs. (2.32) to (2.36).

By taking the derivative of Eq. (2.44) with respect to G, the minimum uncertainty of the measurement becomes:

$$\langle \Delta^2 \hat{M} \rangle_{\text{min}}^{\text{ID,TB}} = \langle \Delta^2 \hat{n}_{pr} \rangle' - \frac{[cov']^2}{\langle \Delta^2 \hat{n}_c \rangle'}, \tag{2.48}$$

or:

$$\left\langle \Delta^2 \hat{M} \right\rangle_{\min}^{\mathrm{ID,TB}} = \eta_{pr} |\alpha|^2 \cosh^2(s) \left[1 + \frac{2\eta_{pr} \sinh^2(s)[1 - 2\eta_c]}{1 + 2\eta_c \sinh^2(s)} \right], \tag{2.49}$$

for an optimum value of G given by:

$$G_{\mathrm{opt}} = \frac{2\eta_{pr} \cosh^2(s)}{2\eta_c \sinh^2(s) + 1}. \tag{2.50}$$

In order to calculate the maximum noise reduction and hence the best squeezing, the corresponding SNL for this measurement is calculated using Eq. (2.44), and by replacing the twin beams with coherent states of the same power, while keeping the same optical losses and the same optimum G that minimizes the noise of the twin beams. Moreover, as mentioned before, for coherent states, there is no correlations, $[cov] = 0$, and the mean is equal to the noise, $\left\langle \Delta^2 \hat{n}_c^0 \right\rangle = \left\langle \hat{n}_c^0 \right\rangle$. Therefore, the noise of the ID measurement at the SNL is given by:

$$\begin{aligned} \left\langle \Delta^2 \hat{M} \right\rangle_{\mathrm{opt}}^{\mathrm{ID,SNL}} &= \eta_{pr} |\alpha|^2 \cosh^2(s) + \eta_c |\alpha|^2 \sinh^2(s) G_{\mathrm{opt}}^2 \\ &= \eta_{pr} |\alpha|^2 \cosh^2(s) \left[1 + \frac{2\eta_{pr}\eta_c \sinh(2s)}{[1 + 2\eta_c \sinh^2(s)]^2} \right], \end{aligned} \tag{2.51}$$

where the "opt" subscript means that the optimum EA is used, which is given by Eq. (2.50). The noise reduction is then given by:

$$R_{\mathrm{loss}}^{\mathrm{EA}} = \left[\frac{1 + 2\sinh^2(s)[\eta_{pr} + \eta_c - 2\eta_{pr}\eta_c]}{1 + 2\eta_c \sinh^2(s)} \right]. \tag{2.52}$$

The optimum squeezing level with EA is shown by red traces in Fig. 2.10. This figure also compares the two methods introduced here to partially overcome an imbalance in optical losses in an ID measurement of the twin beams. As we can see, the use of an EA leads to more squeezing. As opposed to optical balancing, the EA method does

not couple vacuum modes into the measurement, and therefore better maintains the quantum correlations in the twin beams. Both methods can partially overcome an imbalance in optical losses and enhance the squeezing measurement.

2.3.4 SNL Calibration

The level of squeezing in the twin beams is measured with respect to the SNL, obtained with coherent states. As explained before, for a coherent state, the noise is equal to the mean number of photons. Therefore, the noise of a coherent state grows linearly with the intensity of the light. Any deviation from this linear behavior indicates that the noise measurement is not shot-noise limited, which means the state is not a coherent state, but a state with excess noise with respect to the SNL. When a noisy state is used, the SNL is not calibrated properly, which leads to an overestimation of the SNL and the wrong measurement for the level of squeezing.

Technically, it is hard to have pure coherent states to measure the SNL. We usually use a laser beam, which contains classical technical noise. To obtain the SNL from a measurement with such a laser beam, we can use an ID measurement to cancel the classical noise and reach the SNL. However, to verify that this measurement is truly at the SNL, we need to measure the noise of the laser with the same ID measurement as a function of the input laser power. To perform this test, we split the laser beam using a 50/50-BS, and take an ID measurement between the two outputs. When the noise vs. power behavior is linear, as shown in Fig. 2.12, the measurement is shot-noise limited and we can measure the accurate level of the SNL. On the contrary, if the noise

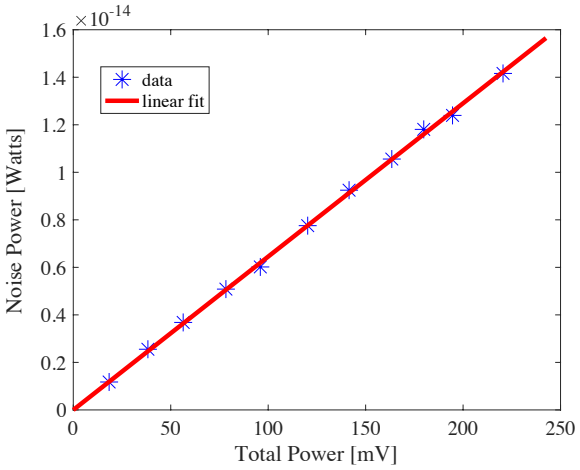

Figure 2.12: Sample data for calibrating the SNL: A linear behavior of the noise power vs. total optical power indicates that the measurement is shot-noise limited.

shows a quadratic growth with increasing power, the measurement is not capable of cancelling the classical noise and the SNL is not measured properly [60].

Proper calibration of the SNL becomes even more important when we introduce an optimum EA to compensate for losses in measurements with twin beams. This optimum EA becomes a part of the detection system, and we need to verify if the measurement is still shot-noise limited to obtain the actual SNL. It is worth noting that if we had a pure coherent state to substitute for the probe and conjugate beams with the same optical power, we could directly measure the real SNL. But for a laser beam with classical noise, we verify that the measurement with unbalanced optical powers and an optimum EA is capable of cancelling the noise and reach the SNL.

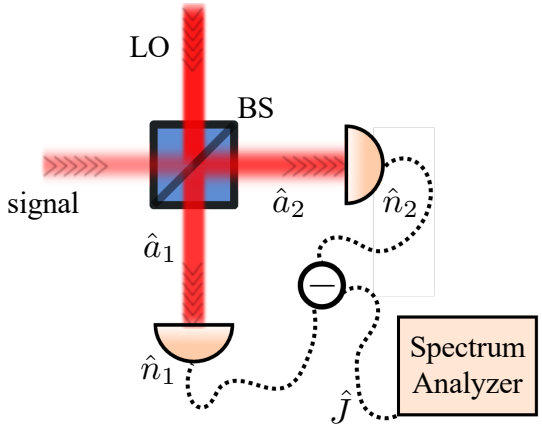

Figure 2.13: Balanced HD: the signal is mixed with a strong LO on a 50/50-BS. The ID of the two detectors provide the phase dependence signal from the resulting interfere. The phase of the LO is scanned by the piezo on its path (not shown).

2.3.5 Homodyne Detection

Although an ID technique is an easy setup for measuring squeezing in the twin beam, it is not sensitive to the phase of the fields under study. Phase-sensitive measurements of an optical field that oscillates at terahertz frequencies is possible with a balanced homodyne detection (HD) technique [61, 62, 63]. A HD measurement is one of the standard techniques that are used to measure the noise of the amplitude and phase quadratures of the fields under study to characterize their quantum correlations.

The schematic of a balanced homodyne detection is shown in Fig. 2.13. The desired field to be measured, the *signal*, can be described as $\hat{E}_s(t) \propto \left[\hat{a}e^{-i\omega t} + \hat{a}^\dagger e^{i\omega t}\right]$. The signal field is combined on a balanced beam splitter with a strong field called the *local oscillator*, LO, described as $\hat{E}_{LO}(t) \propto \left[\hat{a}_{LO}e^{-i\omega t+i\theta} + \hat{a}^\dagger_{LO}e^{i\omega t-i\theta}\right]$. The combined output

light from the two ports of the BS is collected by two photodetectors and their output photcurrents are electronically subtracted.

The output modes of the beam splitter are given by:

$$\hat{a}_{1,2} = \frac{\hat{a}_{LO}e^{i\theta} \pm \hat{a}}{\sqrt{2}}, \tag{2.53}$$

which leads to the difference photocurrent intensity, $\hat{J} = \hat{n}_1 - \hat{n}_2 = \hat{a}_1^\dagger \hat{a}_1 - \hat{a}_2^\dagger \hat{a}_2$, to take the form:

$$\hat{J} \propto \hat{a}_{LO}^\dagger \hat{a} e^{-i\theta} + \hat{a}_{LO}\hat{a}^\dagger e^{+i\theta}. \tag{2.54}$$

Here, we refer to the output of the HD as $\hat{J}$, to distinguish it with the output of the intensity different measurement. Since the LO is a high-intensity field, we can treat it as a classical field, i.e. $\hat{a}_{LO} \approx \alpha_{LO}$. Therefore, the output signal from the HD can be approximated as:

$$\hat{J} \propto \alpha_{LO}\left[\hat{a}e^{-i\theta} + \hat{a}^\dagger e^{+i\theta}\right]. \tag{2.55}$$

As we can see, the HD operator can scan between amplitude and phase quadratures of each mode, depending on the phase of the LO. The phase of the LO can be scanned by using a piezoelectric in its beam path. For example, with $\theta = 0$ we have $\hat{J} \propto (\hat{a} + \hat{a}^\dagger)$, and with $\theta = \pi/2$, the HD operator becomes $\hat{J} \propto (\hat{a} - \hat{a}^\dagger)$, which are the amplitude $\hat{X}$ and phase $\hat{Y}$ quadratures, respectively.

Following the notation of [64], to measure the quadrature noise of the twin beams,

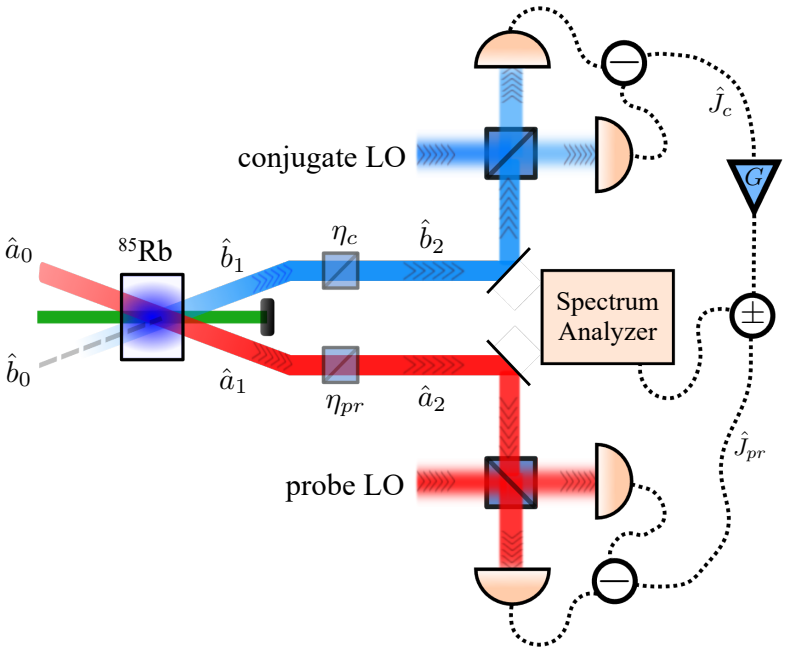

Figure 2.14: Double balanced HD for an optimum characterization of twin beams in presence of optical losses and an EA.

we define the generalized quadrature operators of each of the two fields, as:

$$\hat{J}_{pr} = e^{-i\theta_{LO,pr}}\hat{a} + e^{i\theta_{LO,pr}}\hat{a}^{\dagger}, \tag{2.56}$$

$$\hat{J}_{c} = e^{-i\theta_{LO,c}}\hat{b} + e^{i\theta_{LO,c}}\hat{b}^{\dagger}, \tag{2.57}$$

where we assume each field is measured with a separate HD such that the phase of the two LOs, $\theta_{LO,pr}$ and $\theta_{LO,c}$, can be individually scanned, and modes $\hat{a}$ and $\hat{b}$ represent the probe and conjugate beams, respectively. The outputs of the balanced HDs for the probe and the conjugate beams are then send to a hybrid junction (HJ) to generate the sum and difference signals $\hat{J}_{pr} \pm \hat{J}_c$. These outputs provide access to the generalized joint quadrature sum and difference of the twin beams. i.e. $\hat{X}_{\pm}$ and $\hat{Y}_{\pm}$.

To take into account imperfections in the measurement, we include optical losses in the two beams with the same notation as used in the previous section, as shown in Fig. 2.14. Moreover, similar to the concept of introducing an EA to partially compensate optical losses, we insert an EA after the HD for the mode which suffers less optical losses, assumed to be the conjugate mode. Therefore, the outcome of the measurement becomes: $\hat{M}_{\pm}^{\mathrm{HD}} = \hat{J}_{pr} \pm G\hat{J}_c$.

The final field operators for the probe and the conjugate modes on the HDs are shown by a_2 and b_2 in Fig. 2.14. These two modes, after generating with the FWM process and optical losses, are given by:

$$\hat{a}_2 = \left[\hat{a}_0 \cosh(s) - \hat{b}_0^{\dagger} \sinh(s) e^{i\theta}\right] \sqrt{\eta_{pr}} + \hat{a}_v \sqrt{1-\eta_{pr}}, \tag{2.58}$$

$$\hat{b}_2 = \left[\hat{b}_0 \cosh(s) - \hat{a}_0^{\dagger} \sinh(s) e^{i\theta}\right] \sqrt{\eta_c} + \hat{b}_v \sqrt{1-\eta_c}, \tag{2.59}$$

where θ is the phase of the squeezing operator in the FWM process, and the subscript v represents the vacuum modes that couple due to optical losses.

Using these field operators for the twin beam, we can calculate the mean and variances for each HD to show that they take the form:

$$\left\langle \hat{J}_{pr} \right\rangle = 2\sqrt{\eta_{pr}} |\alpha| \cosh(s) \cos(\theta_{LO,pr}), \tag{2.60}$$

$$\left\langle \hat{J}_c \right\rangle = -2\sqrt{\eta_c} |\alpha| \sinh(s) \cos(\theta_{LO,c} + \theta), \tag{2.61}$$

$$\left\langle \Delta^2 \hat{J}_{pr} \right\rangle = 2\eta_{pr} \sinh^2(s) + 1, \tag{2.62}$$

$$\left\langle \Delta^2 \hat{J}_c \right\rangle = 2\eta_c \sinh^2(s) + 1. \tag{2.63}$$

We can also calculate the covariance to be of the form:

$$[cov]^{\mathrm{HD}} = \langle \hat{J}_{pr}\hat{J}_c \rangle - \langle \hat{J}_{pr} \rangle \langle \hat{J}_c \rangle = -\sqrt{\eta_{pr}\eta_c}\sinh(2s)\cos(\theta_{LO,pr} + \theta_{LO,c} + \theta). \tag{2.64}$$

The mean and variance of the difference of the two HD measurements can then be calculated as:

$$\langle \hat{M}_- \rangle^{\mathrm{HD,TB}} = \langle \hat{J}_{pr} \rangle - G^{\mathrm{HD}-} \langle \hat{J}_c \rangle, \tag{2.65}$$

$$\langle \Delta^2 \hat{M}_- \rangle^{\mathrm{HD,TB}} = \langle \Delta^2 \hat{J}_{pr} \rangle + (G^{\mathrm{HD}-})^2 \langle \Delta^2 \hat{J}_c \rangle - 2G^{\mathrm{HD}-}[cov]^{\mathrm{HD}}, \tag{2.66}$$

where the minus subscript indicates the difference measurement between the two HDs.

By optimizing over the EA, $G^{\mathrm{HD}-}$, the variance of the difference HD reaches a minimum given by:

$$\langle \Delta^2 \hat{M}_- \rangle^{\mathrm{HD,TB}}_{\mathrm{min}} = 1 + \frac{2\eta_{pr}(1-2\eta_c)\sinh^2(s)}{1+2\eta_c\sinh^2(s)}, \tag{2.67}$$

for an optimum EA of [65]:

$$G^{\mathrm{HD}-}_{\mathrm{opt}} = \frac{\sqrt{\eta_{pr}\eta_c}\sinh(2s)\cos(\theta_{LO,pr} + \theta_{LO,c} + \theta)}{1+2\eta_c\sinh^2(s)}. \tag{2.68}$$

In order to access the generalized joint sum quadrature of the twin beams, we can monitor the sum signal from the HJ. Using our calculation results, by adding the two HDs, we obtain the mean and variance signal as below:

$$\langle \hat{M}_+ \rangle^{\mathrm{HD,TB}} = \langle \hat{J}_{pr} \rangle + G^{\mathrm{HD}+} \langle \hat{J}_c \rangle, \tag{2.69}$$

$$\langle \Delta^2 \hat{M}_+ \rangle^{\mathrm{HD,TB}} = \langle \Delta^2 \hat{J}_{pr} \rangle + (G^{\mathrm{HD}+})^2 \langle \Delta^2 \hat{J}_c \rangle + 2G^{\mathrm{HD}+}[cov]^{\mathrm{HD}}, \tag{2.70}$$

where the plus subscript indicates the summation of the two HDs. Therefore, by monitoring both the sum and the difference signal of the two HDs, we can access both joint quadratures of the twin beams.

2.3.6 Entanglement

The quantum correlations between the twin beams can be characterized by the amount of quantum entanglement between the photons in the two beams. There are several standards to quantify this entanglement that are suitable for different applications. Here, since we are interested in characterizing the amplitude and phase entanglement between the twin beams, we use the "inseparability" criteria [66], which is defined as the sum over the joint quadratures and indicates the presence of entanglement if:

$$\mathcal{I} = \left\langle \Delta^2 \hat{X}_- \right\rangle_{\min} + \left\langle \Delta^2 \hat{Y}_+ \right\rangle_{\min} < 2. \tag{2.71}$$

The joint quadratures, $\left\langle \Delta^2 \hat{X}_- \right\rangle_{\min}$ and $\left\langle \Delta^2 \hat{Y}_+ \right\rangle_{\min}$, have been normalized such that their SNL is equal to 1. That is, for a two-mode coherent state, the inseparability parameter $\mathcal{I}$ equals to 2, meaning no entanglement. Therefore, the presence of squeezing in both generalized quadratures of the twin beam is a signature of continuous variable entanglement. Lower values of $\mathcal{I}$ indicate a larger degree of entanglement, providing a direct measure of the degree of entanglement in the system.

Since characterizing the inseparability parameter requires accessing the joint quadratures of the twin beam, we can use a balanced HD for each mode of the twin beam and use the signals for the difference of the HDs, $\left\langle \Delta^2 \hat{M}_- \right\rangle^{\mathrm{HD}}$, and the sum of the HDs, $\left\langle \Delta^2 \hat{M}_+ \right\rangle^{\mathrm{HD}}$, given by Eqs. (2.66) and (2.70) respectively. Therefore, we can access the joint amplitude-difference quadrature $\left\langle \Delta^2 \hat{X}_- \right\rangle = \left\langle \Delta^2 \hat{M}_- \right\rangle^{\mathrm{HD}} = \left\langle \Delta^2 (\hat{J}_{pr} - \hat{J}_c) \right\rangle$, and the phase-sum quadrature $\left\langle \Delta^2 \hat{Y}_+ \right\rangle = \left\langle \Delta^2 \hat{M}_+ \right\rangle^{\mathrm{HD}} = \left\langle \Delta^2 (\hat{J}_{pr} + \hat{J}_c) \right\rangle$ of the twin beam for the correct choice of the LO phases. These two measurements allow us to quantify the

inseparability criteria. An example of such measurement will be presented in chapter 5, where we characterize the quantum entanglement between the twin beams before and after interacting with plasmonic sensors.

2.4 Spatial Quantum Correlations

During the FWM process, energy conservation leads to the relation between the frequencies of the pump and the twin beams. Moreover, the momentum of the four fields must also be conserved, which leads to correlations in the distribution of the photons in space. Here in this section, we study such spatial correlations between the twin beams.

As mentioned before, the twin beams are coupled via the FWM process. In particular, the relation between the momentum vectors is given by Eq. (2.22). These momentum vectors represent the direction of the Poynting vector that determines the direction of the EM wave of propagating for each mode.

For a special case in which the process is phase-mached, $\Delta k = 2k_P - (k_{pr} + k_c) = 0$, the FWM process occurs most efficiently and the twin beams are generated with the most quantum correlations. That means the energy from the pump photons flows efficiently to the pair production of the twin beams in the FWM process. As shown by Eqs. (2.23) and (2.24), for a phase-matched condition, the amplitudes of the twin beams grow exponentially with propagation inside the nonlinear medium.

Generally, $\Delta k \neq 0$, and the efficiency of generating twin beams is reduced from the

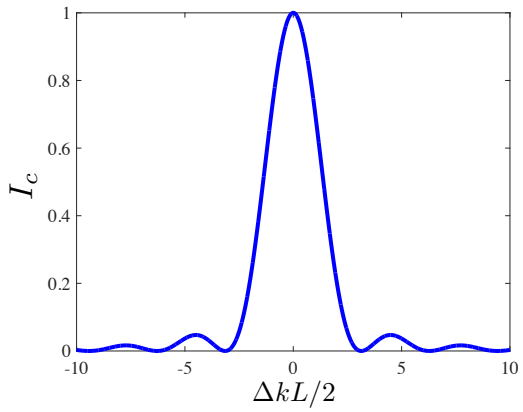

Figure 2.15: The intensity of the conjugate mode represents the efficiency of the FWM process and depends on the phase-matching condition along the propagation of the beams inside the nonlinear medium.

phase-matched condition. For simplicity, we assume the amplitude of the pump beam remains constant as the undepleted pump approximation ($dA_{P_1}/dz = dA_{P_2}/dz = 0$). Therefore, the amplitude of the conjugate beam at the end of the nonlinear medium of length L becomes:

$$A_c(L) \propto A_{P_1} A_{P2} \int_0^L A_{pr}^* e^{i\Delta kz} dz, \tag{2.72}$$

where the initial values of the field amplitudes are at $z = 0$, and the proportionality factor depends on $\chi^{(3)}$, the 3$^{\text{rd}}$ order nonlinear susceptibility of the medium. The intensity of the unseeded conjugate mode (initiated from vacuum, $A_c(0) = 0$) generated from the FWM is then given by [67]:

$$I_c \propto I_{P_1} I_{P_2} I_{pr} L^2 \text{sinc}^2 \left(\Delta kL/2\right). \tag{2.73}$$

The intensity of the conjugate beam as a function of the mismatch condition is plotted in Fig. 2.15, which shows the efficiency of the FWM process. Assuming pump photons

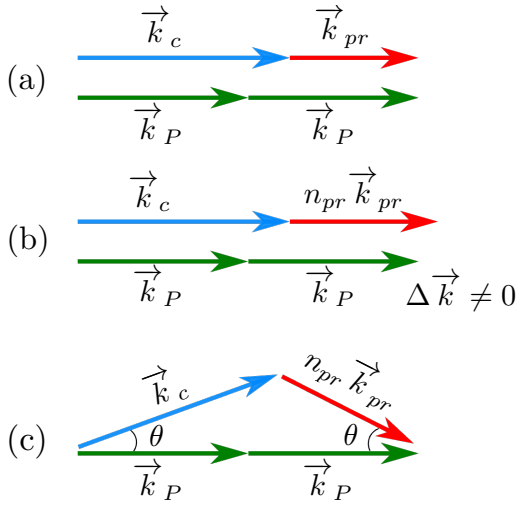

Figure 2.16: Phase-matching condition in FWM between pump (green), probe (red), and conjugate (blue) (a) in free space, (b) with phase-mismatch due to a dispersive medium, and (c) with phase-matching by tuning the angle θ between the beams.

propagate along z-direction of the Rb cell, the phase-mismatch $\Delta kL/2$ gives the range of the k-vectors for the twin beams over which the FWM can occur efficiently. On the contrary, for the case of phase-mismatching, the energy flows from the generated twin beams to the pump beam, which reduces the efficiency of the FWM process of interest.

Due to the dispersive behavior of the medium, the frequency dependence of the index of refraction for each field needs to be taken into account. This leads to a change of the k-vectors by the refractive index, according to $k = n(\omega)\omega/c$. However, the dispersive behavior for the pump beam can be neglected because the Rb atoms are effectively populated in the upper ground state due to the optical pumping in the FWM process, as shown in Fig. 2.6(b). Moreover, the conjugate beam is fur away from atomic

transitions and its dispersive response is not significant. The dispersive behavior for the probe beam is the most dominant dispersive term. Therefore, the phase-matching condition that needs to be satisfied for an efficient FWM, is effectively modified to:

$$\Delta k = 2k_P - (n_{pr}k_{pr} + k_c) = 0, \tag{2.74}$$

where the k-vectors are considered to the be in vacuum. This equation explicitly shows the effect of the refractive index of the medium on the probe beam.

The effective phase-matching condition, Eq. (2.74), can be satisfied by introducing an angle θ between the pump and the probe beams, as shown in Fig. 2.16(c) [52]. Therefore, when the two photons from the pump are co-propagating with k_P along the z-direction, the phase-matching condition becomes:

$$\Delta k_z = 2k_P - n_{pr}k_{pr}\cos(\theta) - k_c\cos(-\theta). \tag{2.75}$$

This means the twin beam photons will be generated with equal but opposite angles symmetrically with respect to the pump beam. Moreover, as shown in Fig. 2.15, the range of the k-vectors that can satisfy the phase-matching condition leads to a range of angles. Therefore, the FWM process can efficiently generate the twin beams over an acceptance angle $\Delta\theta$, which defines the angular bandwidth of the process, as shown in Fig. 2.17.

The phase-matching condition also governs the spatial distribution of the twin beam photons, which leads to position-dependent quantum correlated subregions in the twin beams. The smallest correlated subareas of the twin beams is called the coherence area [68]. The size of these coherence areas determines the spatial resolution of the

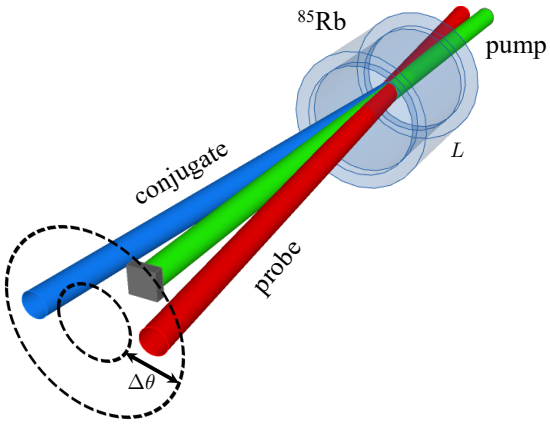

Figure 2.17: The phase-matching condition allows the FWM to occur within an acceptance angle, forming a cone of spontaneously generated vacuum TMSS, around the pump beam. Only the seeded area generates stimulated TMSS, or bright twin beams.

twin beams. That means, smaller coherence areas lead to finer spatial resolutions and are favorable for imaging applications. The optimum experimental parameters for the FWM process to generate spatially correlated twin beams with high resolution, or small coherence areas, depend on the analysis plane, whether in the near field or the far field.

2.4.1 Near Field vs. Far Field

Assuming the center of the Rb cell to be the plane where the FWM process occurs and where the twin beams are simultaneously born, a Fourier transform of the cell center generates the far field, while a plane that is an image of the cell center is the near field. When the analysis plane is on the far field, the momentum of the twin beams at their birth-plane is mapped on to position in the far field. Following the phase-matching

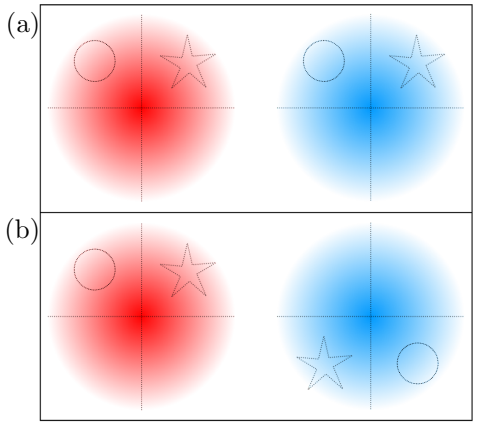

Figure 2.18: Distribution of coherence areas for multi-spatial twin beams (red: probe, blue: conjugate) in (a) the near field and (b) the far field. Star and circle represent independent neighboring subregions in the multi-spatial mode twin beams.

condition, the emission directions of the twin beams are symmetrically opposite to each other with respect to the pump beam. Also, if we assume that the probe photons have a flat wavefront with a single k-vector, a spread of the probe k_{pr}-vectors can be phase-matched with a range of conjugate k_c-vectors. Therefore, in the far field, a point in the probe beam is correlated to the coherence area in the conjugate beam, distributed symmetrically with respect to the pump beam, and vice versa, as shown in Fig. 2.18. The size of the coherence area for the twin beams in the far field is determined by the pump beam's waist size and the flatness of its wavefront at the center of the vapor cell [34].

The near field corresponds to a plane that images the twin beam photons from the center of the Rb cell, and provides information about the location where the twin beam

photons are generated. Given that the probe and conjugate photons are generated at the same transverse spatial locations, the correlated areas of the twin beams on the image plane occur with the same orientation. The phase-matching condition needs to be satisfied along the atomic medium where the FWM occurs, determined by the length of the Rb cell, as shown in Fig. 2.15. As a result, the smaller the length of the atomic cell, the larger the spread of the acceptable k-vectors for an efficient FWM. Coupling of the k-vectors with more spread leads to a higher spatial resolution of the twin beams in the near field. Therefore, in order to have smaller coherence areas in the near field, a shorter vapor cell is needed.

2.4.2 Multi-Spatial-Mode Properties of Twin Beams

A coherent state of light does not contain any temporal or spatial correlations in its subregions and the photons are randomly distributed in space and time. That is, if we produce two coherent states by splitting a laser beam on a balanced BS, there are no correlations between any pairs of subregions. Therefore, the noise of an ID measurement between such subregion pairs of these two coherent states always stays at the SNL.

On the contrary, if there are spatial quantum correlations between the photons of the two beams under study, clipping the beam to select subregions would have a different effect on the noise of these two subregions. In particular, when twin beams are used, the deviation from a linear change of the noise-power as subregions of the twin beams are clipped is an indication of the existence of multi-spatial mode quantum correlations in the twin beams [34, 68, 69], as illustrated in Fig. 2.18.

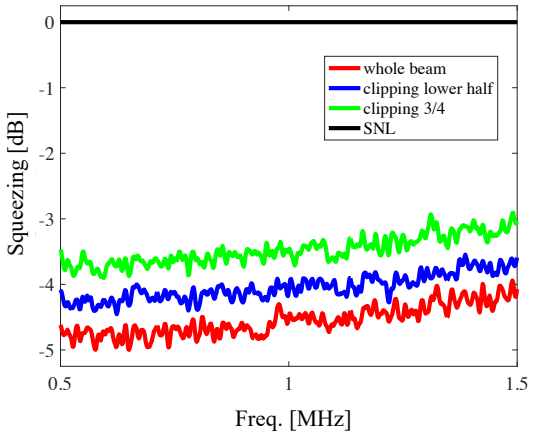

Figure 2.19: Quantum correlated subareas in the twin beams in the near field maintain the level of squeezing in the whole twin beam at both low and high frequencies.

In order to check the distribution of coherence areas in the twin beams, and verify their multi-spatial-mode nature, we measure the level of squeezing within subareas of the twin beam by clipping the beams and performing ID between different subregions of the twin beam. Maintaining the initial squeezing measured with the whole beam for measurements between correlated subareas indicates that independent isolated coherence areas exist in the twin beam. Otherwise, if the size of the coherence area is larger than the selected subareas of the twin beam, the clipping mechanism degrades the level of squeezing obtained with the ID measurement. This is similar to losing quantum correlations between the photons with a loss mechanism, because the blocked subareas lose the quantum correlated photons and leads to coupling of vacuum modes.

The parameters of the FWM can be optimized to have multi-spatial modes in either the near or far field. However, only in the near field the coherence areas of the twin

beam lead to squeezing in both low and high frequencies due to competing nonlinear processes. As we can see in Fig. 2.19, the subregions of the twin beam have almost the same level of squeezing as the whole twin beam in a near field plane. On the contrary, in the far field, subareas from the twin beam shows excess noise, sometimes above the SNL, at low frequencies due to cross talk between the twin beams in the FWM process [70].

Chapter 3

Quantum-Enhanced Sensing

Acknowledgement

Parts of this chapter are published in [71]. The dissertation author is the first author of this publication.

Quantum sensing has emerged as an important field of study in quantum science and technology. It includes estimating a physical quantity based on quantum phenomena, as well as enhancing the sensitivity of existing measurement schemes beyond the SNL by using quantum correlated resources. A quantum-enhanced sensing configuration can be achieved by using quantum squeezed states with reduced noise properties [6, 37, 15, 25]. This means that conventional detection techniques and sensing devices that have reached the SNL can in principle be enhanced with the use of quantum states. A famous example of this is the LIGO, where the phase noise of the interferometer is reduced by coupling a squeezed vacuum into the unused port of a Michelson interferometer [17]. Such a quantum enhancement can be used for quantum metrology [16], quantum imaging [33, 35], and sub-shot-noise sensing with optical readout devices like plasmonic sensors [72, 73, 74, 75] and other devices in biology [38, 76].

With the goal of showing the viability of quantum enhancement for real-life applications, in this thesis, we focus on a quantum sensing protocol that takes advantage of

quantum correlations between squeezed states of light as probing tools. To implement such quantum sensing configurations, quantum states of light substitute their classical counterparts to enhance the sensitivity beyond what is possible with classical states: the SNL.

In this chapter, based on the definition of sensitivity, we discuss the building blocks needed to implement a quantum-enhanced sensing configuration and study approaches for taking the most advantage of the available quantum resources. Although several quantum states can be used for quantum sensing application, our focus in this thesis is on BTMSS (twin beams), introduced in chapter 2. Furthermore, we discuss the importance of the response of the sensor and its transfer function on the advantage that can be obtained with the use of the quantum correlations. We focus on this by studying the fundamental sensitivity bounds for "optical resonant sensors." These passive sensors, with a linear response, include a broad class of sensors that operate based on a shift of their resonant response caused by an external physical stimuli. In chapter 4, we study plasmonic sensors as a particular example of an optical resonant sensor.

3.1 Measurement and Sensitivity

Any measurement contains uncertainties or as noise indicating the separation between the measured quantity and its true (or mean) value. In particular, in an optical measurement with an electromagnetic field, the origin of such uncertainties can be

classical or quantum in nature. Classical sources of noise originate from environmental random fluctuations and are not fundamental, therefore can be eliminated by well-designed schemes for generating and detecting the light. Quantum sources of noise, on the other hand, are inherently fundamental to the generation of the fields, and independent of detection methods. The quantum noise originates from the vacuum fluctuations that are always present, even in the absence of field [44], and even using perfect detectors. As introduced in chapter 2, we can cancel all the classical noise and reach the SNL for classical states of light at best, while with quantum states we can surpass this fundamental noise limit.

In quantum mechanics, we perform a measurement by applying operator $\hat{M}$ on the state of the system under study. The outcome of a measurement with a normal (Gaussian) probability distribution, can be described as:

$$\hat{M} \xrightarrow{\text{gives}} \langle \hat{M} \rangle \pm \sigma, \tag{3.1}$$

where $\langle \hat{M} \rangle$ is the mean (expectation value) and $\sigma = \sqrt{\langle \Delta^2 \hat{M} \rangle}$ is the standard deviation of observable $\hat{M}$, as introduced in section 2.1. In any measurement, a natural question is the precision, or sensitivity of the measurement. The sensitivity determines how well we can resolve two mean values in a measurement, or alternatively quantifies the smallest resolvable separation between these two measured mean values. This is pictorially shown in Fig. 3.1(a) when the outcomes of measurement $\hat{M}$ are given by a normal probability distribution function (PDF). The PDF shows the probability of obtaining a given measurement outcome. In this figure, the outcomes of measurement

$\hat{M}$ have two mean values $\hat{M}_1$ and $\hat{M}_2$. The separation between the two measured mean values indicates the sensitivity to resolve the outcome of a measurement uniquely from other mean values.

One conventional definition of the sensitivity is based on the standard deviation, σ, to quantify how far apart the two measured mean values are. The sensitivity is then reported by integer multiplications of σ, such as 1σ, 2σ, and 3σ, as shown in Fig. 3.1(b). Another common way to define the sensitivity is by calculating the confidence level (CL) of the measurement from the PDF. The CL indicates the percentage of data points that fall below this level, and therefore, represents our confidence in expecting the outcome of the measurement to fall within a specific interval from the mean value of the desired measured parameter. The CL is related to the standard deviation, but not in terms of discrete values. Standard values of 90%, 95%, and 99% CL, are shown in Fig. 3.1(b).

When the measured parameter can be modulated around its mean, we are interested in finding the smallest magnitude of the modulation that the sensor can resolve from noise. Comparing the size of the modulation signal to the noise of the measurement gives the signal-to-noise-ratio (SNR), providing a measure of useful information (signal) to the undesired information (noise). Hence, increasing the SNR value increases the capability of the sensing apparatus to resolve information about the desired modulation out of the noise in the measurement. Therefore, the sensitivity of this measurement determines the smallest resolvable modulation signal compared to the noise of the measurement. For example, when the magnitude of the signal becomes equal to the noise, that is SNR= 1.

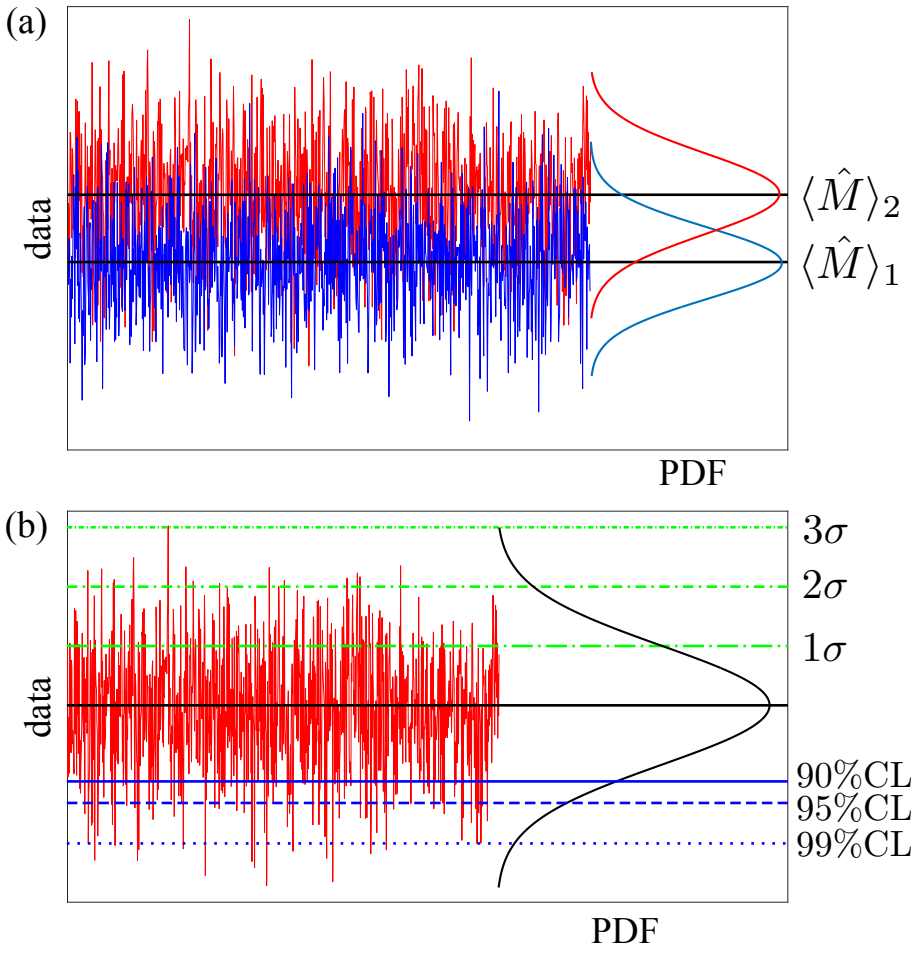

Figure 3.1: (a) The outcomes of measurement $\hat{M}$ have a Gaussian probability distribution function (PDF) with two mean values $\langle \hat{M} \rangle_1$ and $\langle \hat{M} \rangle_2$. (b) Uncertainty levels around the mean value of a measurement with Gaussian PDF.

Using the definitions for the sensitivity of a measurement, the smaller the uncertainty (noise) in the measurement, i.e. σ, the closer two mean values can get while still being able to resolve them, which leads to a better sensitivity. In this thesis, we define the sensitivity of measurement $\hat{M}$ as its standard deviation, $\sqrt{\langle \Delta^2 \hat{M} \rangle_{\min}}$. Therefore, the smaller the uncertainty (noise) the higher the sensitivity (minimum uncertainty leads to maximum sensitivity).

3.1.1 Sensitivity of an Estimation Parameter

Not every parameter can be directly measured. However, we can estimate such parameters via performing a measurement on another dependent variable. Let's say the parameter of interest n depends on a measurable parameter $\hat{M}$, as $n = n(\hat{M})$. The sensitivity of the desired parameter n will then be defined through the error propagation relation as:

$$\langle \Delta^2 n \rangle = \frac{1}{|\partial \hat{M}/\partial n|^2} \times \langle \Delta^2 \hat{M} \rangle. \tag{3.2}$$

That is, in order to find the sensitivity of our parameter of interest, $\langle \Delta n \rangle$, first its functional dependence on the measurement parameter $\hat{M}$ needs to be defined through characterizing the transfer function of the sensing apparatus. Then, the sensitivity of the sensor for the estimated variable can be calculated by using the transfer function of the sensor and the uncertainty of the measurement parameter.

For example, an optical readout sensor can introduce changes in the transmission of the probing light, T. The uncertainty of transmission ΔT can then be estimated by measuring the uncertainty of the intensity of the probing light, ΔI, using the error

propagation relation given in Eq. (3.2). Moreover, if the change in transmission itself is introduced by another parameter, we can use the error propagation relation once more to estimate the sensitivity of the parameter of interest through a proper measurement on the probing light.

3.2 Enhancing the Sensitivity

There are several ways to enhance the sensitivity of a measurement or a sensing device. One way is through increasing the intensity of the probing light, which reduces the relative noise of the measurement as $\sqrt{\langle \Delta^2 \hat{M} \rangle / N}$ for classical states, where N is the mean number of photons used for probing the system. However, increasing the number of probing photons is not always a feasible option due to multiple reasons. One is the limitation on the available resources, as the number of photons in an intense beam of light is limited. Another limitation is the damage threshold of the sample under study or the sensor itself that limits the amount of permitted optical power for probing. Moreover, the amount of optical power that we can send into a detector is finite [26, 76, 77, 78, 79]. Considering these limitations, it is crucial to keep track of the number of probing photons for comparing different sensing methods with equal resources.

With a fixed number of photons, the noise of the measurement can also be reduced by increasing the detection time to average over more measurements. Because in this thesis we are interested in enhancing the sensitivity of a sensor with the use of quantum

squeezed light, to have a fair comparison between measurements with classical and quantum resources we keep the number of photons and the detection time the same as our sensing resources throughout this thesis. With equal resources, we can perform a fair comparison between the sensitivities with quantum twin beams and coherent states and quantify the amount of advantages with the use of quantum-correlated states of light.

To understand how to enhance the sensitivity, we consider Eq. (3.2). The first term on the right hand side of this equation is the inverse of the rate of changes in the measured variable with respect to the estimated physical parameter of interest, $\frac{1}{|\partial \hat{M}/\partial n|}$, and depends on the transfer function of the sensor. Larger rates of such changes lead to smaller uncertainties in our estimation, consequently, a higher sensitivity of the sensor. The sensor's transfer function defines the characteristic response of the sensor to different variables, which can be adjusted to obtain large rates of changes within the fabrication limitations. Here, we assume that the response of the sensor is the same for both classical and quantum states of light and we are able to tune the response of the sensor to operate at the point where we achieve the maximum sensitivity [80].

The second term on the right hand side of Eq. (3.2) is the uncertainty of the measurement parameter, $\left\langle \Delta^2 \hat{V} \right\rangle$, which is fundamentally limited by the noise properties of the probing state of light. The smallest variance of the measurement parameter is given by the fundamental limits due to quantum mechanics [3]. Enhancing the sensitivity is particularly critical when we want to detect small modulations with magnitudes comparable to the noise at a fundamental limit. When classical states of

light are used, the lowest noise level will be obtained with coherent states, defining the SNL in the sensitivity of our measurement. Moreover, when quantum states of light as used, such as the twin beams that we introduced in chapter 2, the uncertainties of the measurement can reach values below the SNL, and therefore a quantum enhancement is possible.

Since the sensitivity of a sensor depends both on the response of the sensor and the noise properties of the probing light, both factors need to be taken into account to estimate its overall sensitivity. The interplay between these two factors changes the optimum operating point depending on the measurement variable and sensor's transfer function. In the next section, we introduce the constituting elements of a general quantum sensing configuration, which clarifies the connection between different sensitivity factors. In section 3.4, we will use the example of optical resonant sensors to better demonstrate the interplay between responses of the sensor and properties of the probing light.

3.3 Quantum Sensing Building Blocks

In general, quantum-enhanced sensors consist of three main parts: the source of quantum states*, the sensing device, and an appropriate detection method, as shown in Fig. 3.2. For our particular implementation, the light source can generate BTMSS of light with uncertainties below the SNL, as introduced in chapter 2. The probe of the twin beams

*Since we are studying applications for quantum states of light, we consider quantum states and coherent states of light to probe optical readout sensors.

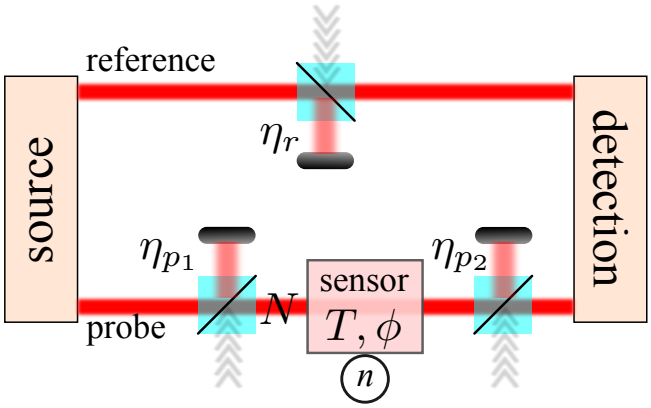

Figure 3.2: Quantum sensing building blocks: a source of quantum states, a sensing device, and a detection scheme. N: number of photons probing the sensor, n: physical quantity of interest. Arrows indicate the coupling of vacuum modes due to optical losses.

is used to probe an optical readout sensor, while the conjugate beam is used as the reference. Such sensors can sense changes in the physical parameter of interest by introducing measurable changes in the probing light field [81].

To implement the classical counterpart configuration, the light source can generate coherent states of light to replace the twin beams and perform the sensing at the SNL. However, as we will see later in this analysis, the optimum measurement with coherent states is one with a single mode used to probe the sensor, as using the second mode increases the uncertainty of the measurement. To include experimental imperfections, we model optical losses with BS in the probe mode both before and after the sensor, as well as the losses in the reference mode, as introduced in chapter 2.

The optical readout from the probe and the reference beams, after interacting

with the sensor, are measured using detection methods compatible with the measuring variable. It is important to note that with both classical and quantum states the number of photons probing the sensor, N, and the detection settings are kept fixed as they represent the resources for sensitivity estimation.

3.4 Optical Resonant Sensors

Optical resonant sensors are passive optical devices with linear responses and are characterized by a transfer function that exhibits a resonance in its transmission spectrum, $T(\lambda)$, where λ is the wavelength. As a result of the resonance, the phase of the light field probing these sensors, $\phi(\lambda)$, undergoes changes corresponding to the transmission resonance, where the relation between the phase and the transmission is governed by the Kramer-Kronig relationship [82, 83]. These sensors are widely used as label-free sensors with an optical readout, whose sensitivities are limited to the SNL when probed with classical states of light [84]. Examples of these sensors include optical cavities [85], whispering-gallery mode sensors [86, 87], photonics crystal sensors [88], and plasmonic sensors [27, 89].

Optical resonant sensors can be used to estimate changes in an external physical quantity, such as temperature, pressure, force, index of refraction, etc., based on measuring changes in the transmission or the phase of the probing light, as shown in figure 3.3. When the physical parameter of interest, n, changes by an amount Δn, it can lead to changes in transmission and phase by ΔT and $\Delta\phi$, respectively [90, 91, 92, 93].

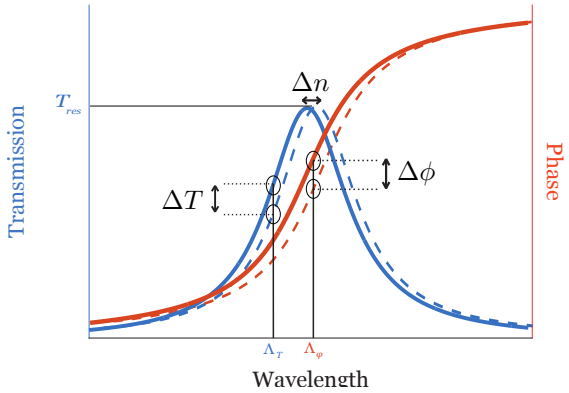

Figure 3.3: The optical resonance in the transmission spectrum (blue traces) and the corresponding phase spectrum (red traces) shift to the dashed lines due to changes in a physical quantity n. This leads to changes in transmission and phase of the probing light at the operational wavelength.

Thus, we can use optical resonant sensors to estimate changes in the external physical parameter by measuring changes in transmission, transmission-based scheme, or phase, phase-based scheme, of the probing light.

Sensing schemes based on phase and transmission can provide different sensitivities, and have been compared for particular cases of resonant sensors [81, 89, 91, 92, 93], but not at their fundamental sensitivity limits. Moreover, the sensitivity of these sensors with both schemes can be enhanced beyond the SNL by replacing the coherent states with quantum correlated states, such as the twin beams that were introduced in chapter 2. Twin beams have already proved applicable for quantum-enhanced schemes based on phase [64, 94] and transmission [95].

Here, to have a fair and absolute comparison between the sensitivity of both

schemes, we consider the uncertainties based on transmission and phase to be at the their fundamental bounds, given by the quantum Cramér-Rao bound (QCRB) [96, 97]. The QCRB provides the fundamental bound for the sensitivity of each sensing scheme, T or ϕ, and sets the maximum quantum enhancement with given resources. This fundamental bound gives the maximum information we can extract from a sensor with any possible measurement using a given state of light. The QCRB depends on the properties of the states of light used for probing, the unitary transformation of the sensing device, and the losses involved before or after the sensing device. The QCRB is calculated by optimizing over all possible measurements, and therefore, it is independent of the measurement procedure.

In this section, we focus on comparing the sensitivity of resonant sensors based on the transmission and phase schemes, for sensors with a peak in their transmission spectrum. However, this study can be generalized to other possible sensing schemes and to sensors with an arbitrary transfer function response as we showed in [71].

3.4.1 Sensitivity of Sensing Schemes

For an optical resonant sensor, we can estimate the changes in a physical quantity of interest n by measuring transmission T and phase ϕ from the probing light. Following the notation of Eq. (3.2), the sensitivity is then defined as the minimum uncertainty of changes in the physical parameter $\langle \Delta n \rangle$ that the sensor can resolve [73, 3]:

$$\langle \Delta n(X) \rangle_{\min} = \min \left[\left(\frac{\Delta X}{|\partial X/\partial \lambda|} \right) \cdot \frac{1}{|\partial \lambda/\partial n|} \right], \tag{3.3}$$

where the variable $X(\lambda)$ indicates transmission $T(\lambda)$ or phase $\phi(\lambda)$, as illustrated in Fig. 3.3.

Since the transmission and phase depend on the wavelength of light, the sensitivity of the sensor will have a spectrum. The fundamental bound for this sensitivity spectrum of a resonant sensor depends on both the response of the sensor through its transfer function and on the QCRB for the scheme, which itself depends on the noise properties of the probing state of light. A trade off between these two factors determines the overall fundamental bound of sensitivity of an optical resonant sensor.

The dependence of the physical quantity of interest on the estimation parameters, $n = n(X(\lambda))$, is obtained from the characteristic behavior of the resonant sensor and is determined by its unique design and fabrication parameters. Such dependence can be characterized by the sensor's transfer function spectrum. The two rates in Eq. (3.3) are then directly obtained from the shift of the transfer function in response to the changes in the physical quantity of interest. On the other hand, the uncertainty of a parameter $\langle \Delta X(\lambda) \rangle$ is fundamentally limited by the QCRB and only depends on the intensity and the noise properties of the probing states of light.

The first term on the right hand side of Eq. (3.3) can be written in terms of the sensitivity of shifts in the resonant wavelength, $\langle \Delta\lambda \rangle_X = \langle \Delta X \rangle / |\partial X/\partial\lambda|$. The second term on the right hand side of Eq. (3.3), $1/|\partial\lambda/\partial n|$, represents the rate of change in the resonance wavelength due to changes in the external physical parameter, and is a common factor for both sensing schemes. In this study, when we compare the sensitivity of the transmission and phase schemes, this term cancels out, but needs to be included

for calculating the absolute sensitivity of the sensor with each scheme.

3.4.2 Optical Resonant Sensor Transfer Function

The transfer function defines the characteristic transmission spectrum of the resonant sensor to the interrogating light. Since we consider sensors with linear responses, transmission and phase are related by the Kramers-Kronig relationships. Therefore, we can extract the analytical phase spectrum response of a resonant sensor from its transmission transfer function.

In this thesis, we focus only on sensors with a transfer function that has a peak resonance on its transmission spectrum, which can be written as:

$$\mathrm{T}(\lambda) = T_{\mathrm{res}} T_0(\lambda), \tag{3.4}$$

where T_{res} is the transmission at resonance, and T_0 defines the resonance lineshape. A general transfer function for intensity transmissions with arbitrary peak or dip resonances is studied in [71].

The lineshape $T_0(\lambda)$ that we consider in Eq. (3.4) has a unit transmission at resonance while the tails go to zero as $|\lambda| \to \infty$. Here, as the transfer function, we consider a Lorentzian lineshape, as it describes the resonant response of homogeneous interactions, such as a two-level atom or a Fabry-Perot cavity, with isolated resonances, and is given by:

$$T_0(\lambda) = \left| \frac{1}{\frac{\lambda - \lambda_0}{\Delta L} + i} \right|^2, \tag{3.5}$$

where λ_0 is the resonant wavelength, ΔL is the half-width half-max (HWHM), and

$i = \sqrt{-1}$. To make the transfer function independent of the HWHM and the resonant wavelength of the Lorentzian lineshape, we define the generalized wavelength as $\Lambda = \left(\frac{\lambda - \lambda_0}{\Delta L}\right)$. With this definition, the sensitivity of the resonant sensor will be re-scaled as $\langle \Delta\Lambda \rangle_X = (\Delta L)^2 \langle \Delta\lambda \rangle_X$, which represents another common factor in our comparison between the sensing schemes based on transmission and phase.

For arbitrary values of T_{res}, the transmission and phase transfer functions for a Lorentzian lineshape takes the form:

$$T(\Lambda) = \frac{T_{\text{res}}}{1 + \Lambda^2}, \tag{3.6}$$

$$\phi(\Lambda) = \arctan\left(\frac{1}{\Lambda}\right). \tag{3.7}$$

From these relations, we can directly calculate the derivatives of the transmission or phase response with respect to wavelength, constructing the transfer function part of the sensitivity spectrum.

3.4.3 QCRB: Fundamental Uncertainty Bounds

By using the QCRB for parameter X, we can calculate the fundamental sensitivity bound for an optical resonant sensor. This bound provides the smallest changes in the physical parameter of interest that can be resolved using a particular state. Based on the sensing configuration where one mode of the twin beam is used to probe the sensor and the other one is used as a reference, as shown in Fig. 3.2, the QCRB for transmission for a BTMSS is given by [95]:

$$\langle \Delta^2 T \rangle^{\text{BTMSS}} \geq \frac{T}{\eta_{p2} N} - \frac{2T^2 \eta_{p1}}{N} \frac{\sinh^2(s)[2\eta_r - 1]}{\left[1 + 2\eta_r \sinh^2(s)\right]}, \tag{3.8}$$

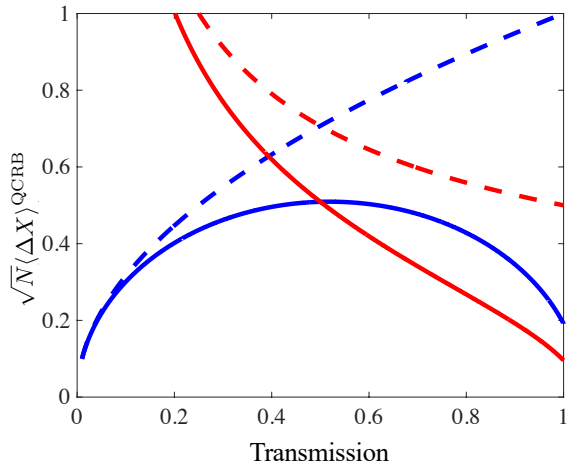

Figure 3.4: The uncertainties (standard deviations) at the QCRB of transmission (blue traces) and phase (red traces) for a lossless configuration, as a function of transmission through the resonant sensor. Dashed lines indicate when a coherent state is used, while solid traces are for a BTMSS with $s = 2$. A smaller uncertainty indicates a larger sensitivity of a parameter.

where η_{p1}, η_{p2}, η_r, are the intensity transmissions before and after the sensor in the probe beam and in the reference beam (the conjugate mode of the twin beam), respectively. On the other hand, the QCRB for phase is given by [71]:

$$\left\langle \Delta^2 \phi \right\rangle^{\mathrm{BTMSS}} \geq \frac{1}{4T\eta_{p2}N} - \frac{\eta_{p1}}{2N} \frac{\sinh^2(s)[2\eta_r - 1]}{\left[1 + 2\eta_r \sinh^2(s)\right]}. \tag{3.9}$$

In Eqs. (3.8) and (3.9), N is the number of photons probing the resonant sensor, which we keep fixed as our resource, and is given by losses before the sensor and the photons generated from the source.

The QCRB for the estimation parameter with a coherent state is calculated by setting the squeezing parameter to zero, $s = 0$, in Eqs. (3.8) and (3.9). This means

that the first term in these two equations represent the SNL for each sensing scheme. By increasing the level of squeezing from zero, the quantum correlations between the twin beams reduce the uncertainty of the estimation parameter. In our comparison between the SNL and the twin beams, we consider the particular squeezing of $s = 2$, corresponding to ≈ -14.5 dB of ID squeezing. This level of squeezing has been experimentally generated for single-mode squeezed states [98] and is within reach for the case of bright twin beams.

Figure 3.4 shows the QCRB for transmission and phase, given by taking the square root of Eqs. (3.8) and (3.9), as a function of transmission T for a BTMSS with $s = 2$ and a coherent state, $s = 0$, without optical losses. As we can see, the QCRB for transmission has local minima (corresponding to the most sensitivity points) when T goes to one or zero. These points refer to the cases where all or none of the photons probing the sensor reach the detector and lead to the least uncertainty of transmission. For the QCRB for phase, the sensitivity worsens monotonically with reduced transmission due to the loss of photons carrying information about the phase. In the limit of no photons, the uncertainty goes to infinity, as we do not have any information about the phase. Moreover, the reduction in the uncertainty (enhancement in sensitivity) can be clearly seen when using twin beams with respect to a coherent state.

3.4.4 Experimental Setups to Saturate the QCRB

The fundamental QCRB for the uncertainty of a parameter is a theoretical value. However, we show here that we can reach the QCRB for transmission and phase

experimentally. Based on the results we got in section 2.3.5, we can show that a HD technique with an EA, as shown in Fig. 2.14, can saturate the QCRB for transmission and phase.

As given in section 2.3.5, we can access the squeezed joint quadratures of the twin beams, the amplitude-difference and phase sum-quadratures, by subtracting and adding the output signal of the two HDs, given by $M_{\pm} = \hat{J}_{pr} \pm G\hat{J}_r$, where $\hat{J}_{pr}$ and $\hat{J}_r$ are the HD measurements for the probe and the reference beams, respectively, and G is the variable EA. Following the configuration in Fig. 3.2, in order to calculate $|\partial\hat{M}/\partial X|$, the resonant sensor is placed on the path of the probe beam, $\hat{J}_{pr}$, such that only the HD of the probe beam contains information on the phase and transmission introduced by the sensor.

The uncertainty of the phase can be obtained from the error propagation relation according to:

$$\left\langle \Delta^2\phi \right\rangle_{\hat{M}_+} = \frac{\left\langle \Delta^2\hat{M}_+ \right\rangle}{|\partial\left\langle \hat{M}_+ \right\rangle/\partial\phi|^2}. \tag{3.10}$$

Moreover, the mean of the quadrature sum measurement between the two HDs can be obtained from Eqs. (2.60) and (2.61), and is given by:

$$\begin{aligned}\left\langle \hat{M}_+ \right\rangle^{\mathrm{HD}} =& 2\sqrt{\eta_{p1}\eta_{p2}T}|\alpha|\cosh(s)\cos(\theta_{LO,pr}+\phi) \\ &- 2G\sqrt{\eta_r}|\alpha|\sinh(s)\cos(\theta_{LO,r}+\theta),\end{aligned} \tag{3.11}$$

where $|\alpha|$ is the magnitude of the probe beam seeding the FWM process. For the denominator of Eq. (3.10), by keeping the EA its constant optimum value, we have:

$$\left|\frac{\partial\left\langle \hat{M}_+ \right\rangle}{\partial\phi}\right| = 2\sqrt{\eta_{p1}\eta_{p2}T}|\alpha|\cosh(s)\sin(\theta_{LO,pr}+\phi), \tag{3.12}$$

which can be maximized by setting the phase of the probe LO such that $\sin(\theta_{LO,pr}+\phi)$ becomes one. Moreover, the optimum variance of measurement $\hat{M}_+$ is given by:

$$\begin{aligned}\left\langle \Delta^2 \hat{M}_+ \right\rangle_{\text{opt}}^{\text{HD,TB}} =& 2\eta_{p1}\eta_{p2}T\sinh^2(s)+1 \\ &- \frac{4\eta_{p1}\eta_{p2}\eta_r T\cosh^2(s)\sinh^2(s)}{1+2\eta_r\sinh^2(s)},\end{aligned} \tag{3.13}$$

with optimum EA [65]:

$$G_{\text{opt}} = \frac{\sqrt{\eta_{p1}\eta_{p2}\eta_r T}\sinh(2s)}{1+2\eta_r \sinh^2(s)}. \tag{3.14}$$

Using these results, the optimum uncertainty for phase estimation is given by:

$$\left\langle \Delta^2 \phi \right\rangle_{\text{opt}} = \frac{1}{4\eta_{p2}TN} - \frac{\eta_{p1}}{2N}\frac{\sinh^2(s)[2\eta_r-1]}{\left(1+2\eta_r \sinh^2(\text{s})\right)}, \tag{3.15}$$

which is the same as the QCRB for phase given in Eq. (3.9). Similar to the previous definition, the number of photons probing the sensor is equal to $N=\eta_{p1}|\alpha|^2\cosh^2(s)$.

In order to access the amplitude-difference quadrature for the twin beams, we consider the difference of the two HD measurements, $\hat{M}_- = \hat{J}_{pr} - G\hat{J}_r$. Using such a measurement, the uncertainty in transmission is obtained from:

$$\left\langle \Delta^2 T \right\rangle_{\hat{M}_-} = \frac{\left\langle \Delta^2 \hat{M}_- \right\rangle}{|\partial\langle \hat{M}_- \rangle/\partial T|^2}. \tag{3.16}$$

For the denominator, we have:

$$\left|\frac{\partial\langle \hat{M}_- \rangle}{\partial T}\right| = \sqrt{\frac{\eta_{p1}\eta_{p2}}{T}}|\alpha|\cosh(s)\cos(\theta_{LO,pr}+\phi). \tag{3.17}$$

To have the minimum uncertainty in the estimation of transmission, the phase of the probe's LO is set such that $\cos(\theta_{LO,pr}+\phi)$ becomes maximum. Moreover, the variance of

measurement $\hat{M}_-$ has the same optimum value as measurement $\hat{M}_+$, given in Eq. (3.13). Using these results, the optimum uncertainty for transmission results in:

$$\left\langle \Delta^2 T \right\rangle_{\text{opt}} = \frac{T}{\eta_{p2} N} - \frac{2T^2 \eta_{p1}}{N} \frac{\sinh^2(s)[2\eta_r - 1]}{\left[1 + 2\eta_r \sinh^2(s)\right]}, \tag{3.18}$$

which is the same as the QCRB of transmission shown in Eq. (3.8).

An ID method with a variable EA can also saturate the QCRB for transmission [95]. This method is easier to implement that a HD as it does not require the generation of the LO, and therefore, lacks the need of spatial mode matching between the LO and the signal beams and the complication of locking the phases of their LOs. We can show that by using the model introduced in section 2.3.1 for calculating the sensitivity of an ID measurement, we can also saturate the QCRB of transmission [71].

3.4.5 Interplay between QCRB and Transfer Function

Knowing the transfer function of a given sensor and the the QCRB for transmission and phase, we can calculate the fundamental sensitivity bound of a resonant sensor based on either sensing scheme. The two factors determine the optimum operating wavelength and the overall sensitivity of the sensor. Since the minimum value of the QCRB with twin beams and the sharpest rate of changes for the sensor's transfer function do not coincide at the same wavelength, there is an interplay between these two quantities to obtain the maximum sensitivity of the sensor.

We study this interplay for the particular example of an ideal resonant sensor without optical losses and with a full-peak resonance Lorentzian lineshape, $T_{\text{res}} = 1$,

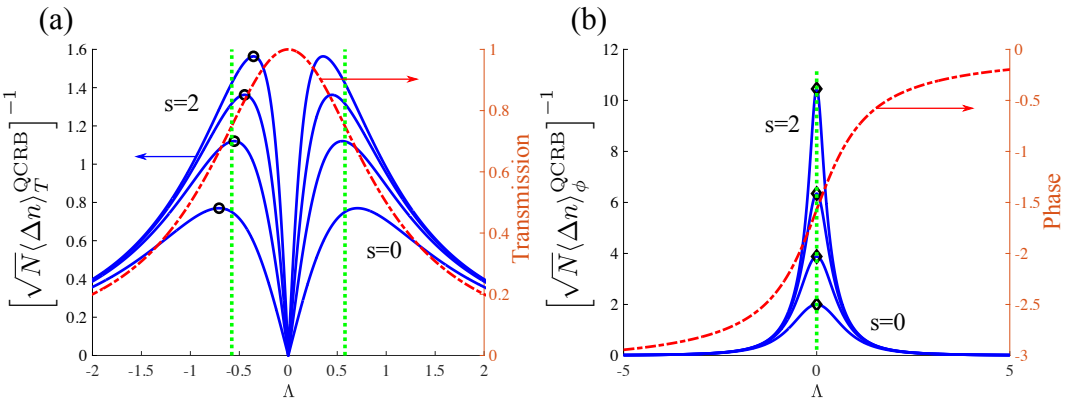

Figure 3.5: Interplay between the QCRB and the rate of change of the transfer function for (a) transmission and (b) phase sensing scheme, for $s = 0, 1.0, 1.5, 2.0$. Green dotted lines indicate the wavelengths where the slope of the transfer functions maximize.

shown in Fig. 3.5. In this figure, we plot the inverse of the uncertainty of the physical quantity of interest multiplied by the square root of the number of photons probing the sensor, that is $\left[\sqrt{N}\langle\Delta n\rangle_X^{\mathrm{QCRB}}\right]^{-1}$, for sensing schemes based on transmission and phase. By studying the inverse of the uncertainty, we can better see the wavelength where the maximum sensitivities occur.

As the squeezing of the BTMSS increases, the sensitivity for both schemes increases but at different rates. Also, the optimum wavelength at which the highest sensitivity is achieved for each scheme is different. As can be seen in Fig. 3.5(a), for the sensitivity bound of a transmission-based sensing scheme, as the squeezing parameter increases the wavelengths of maximum sensitivity shift towards the wavelengths of higher transmissions, i.e. towards the resonant peak at $\Lambda = 0$. As mentioned before, the QCRB for

transmission minimizes as transmission goes to one, while the slope of the transmission spectrum is away from the resonance, shown by the green dotted lines in Fig. 3.5(a). As the level of squeezing increases, higher sensitivities are achieved at higher transmissions.

On the other hand, for a phase-based sensing, shown in Fig. 3.5(b), the maximum sensitivity always occurs on resonance. This is because both the maximum slope and the minimum value of the QCRB for phase occur at the resonant wavelength. Therefore, for all levels of squeezing, the most sensitive wavelength for the phase-based sensing schemes always occurs at the resonant wavelength.

3.5 Quantum Enhancement

The reduced-noise properties of the twin beams can reduce the uncertainty of sensing schemes based on the transmission and phase with respect to their equivalent classical counterparts, when coherent states are used. We first focus on the quantum enhancement in reducing the uncertainty of the estimation parameter. To quantify this quantum enhancement, we define the quantum enhancement factor (QEF) as the ratio between the uncertainty of the estimation parameter with coherent states at the QCRB over the same bound with the twin beams. With equal resources, the QEF for the estimation of parameter X is given by:

$$\mathrm{QEF}(X) = \sqrt{\frac{\langle \Delta^2 X \rangle_{\mathrm{SNL}}^{\mathrm{QCRB}}}{\langle \Delta^2 X \rangle_{\mathrm{BTMSS}}^{\mathrm{QCRB}}}} = \left\{ 1 - T \left[\frac{2(2\eta_r - 1)\eta_{p1}\eta_{p2} \sinh^2(s)}{1 + 2\eta_r \sinh^2(s)} \right] \right\}^{-1/2}, \qquad (3.19)$$

which is the same for both transmission and phase, and depends on the squeezing parameter, s, transmission, T, and the optical losses in the probing and reference

beams. A QEF greater than one corresponds to a better sensitivity of parameter X (transmission or phase) with the use of twin beams compared to a coherent state. According to Eq. (3.19), such quantum enhancements happen as long as losses in the reference beam are confined to $(1-\eta_r) < 1/2$, keeping the second term positive. If losses in the reference beam are high enough, the QEF drops below one, indicating no advantage in using a twin beam over a coherent state.

Although the quantum enhancement to reduce the uncertainty of the estimation parameter is important, we are more interested in quantifying the quantum enhancement in the overall sensitivity bound of the sensor for the physical quantity of interest. Such quantum enhancement in the sensitivity depends on the sensing scheme because the response spectrum of a resonant sensor is different for each scheme. To quantify the quantum enhancement in the sensitivity of the resonant sensor, and to fairly compare the different sensing schemes, we compare the maximum sensitivities, which occur at different Λs with a BTMSS and a coherent state, at their fundamental QCRB. To contrast this comparison with the QEF in Eq. (3.19), we define the "effective quantum enhancement factor" (EQEF), as:

$$\mathrm{EQEF}(X) = \frac{\min\limits_{\Lambda} \left\langle \Delta n \right\rangle_{X,\mathrm{BTMSS}}^{\mathrm{QCRB}}}{\min\limits_{\Lambda} \left\langle \Delta n \right\rangle_{X,\mathrm{SNL}}^{\mathrm{QCRB}}}, \tag{3.20}$$

which not only includes $\left\langle \Delta^2 X \right\rangle^{\mathrm{QCRB}}$, the QCRB of parameter X, but also $|\partial X/\partial n|$, the transfer function response of the resonant sensor.

Since the optimum wavelengths at which the best sensitivity for each scheme occurs are different, the EQEF contains the interplay between the minimum QCRB of the

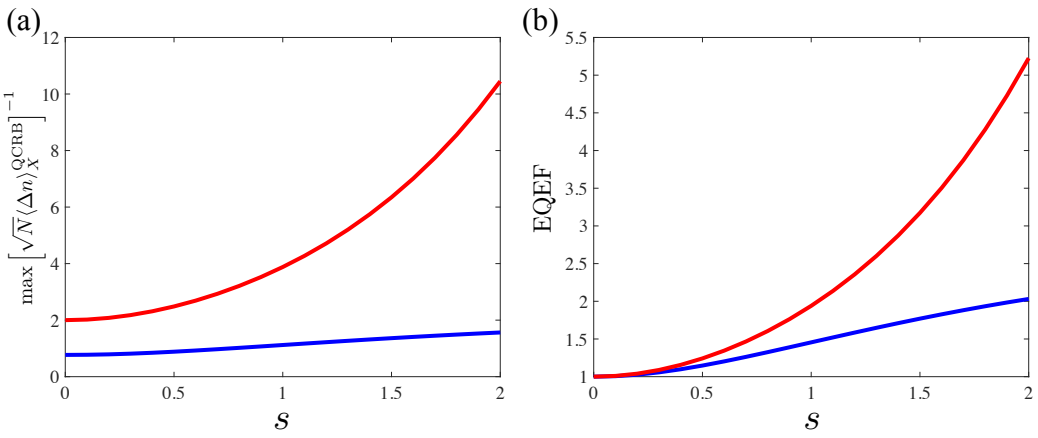

Figure 3.6: (a) Maximum fundamental sensitivities and (b) EQEF as a function of squeezing for sensing schemes based on transmission (blue) and phase (red). Here $T_{\mathrm{res}} = 1$.

estimation parameter and the sharpest rates of changes in the estimation parameter with respect to the physical quantity of interest. In Eq. (3.20), the term "min-Λ" refers to this interplay and corresponds to the optimum wavelength at which the best sensitivity for each scheme occurs. These correspond to the points that were indicated by circles (diamonds) for transmission (phase) in Fig. 3.5, and are shown in Fig. 3.6(a) as a function of the squeezing parameter. In Fig. 3.6, we assume the sensor has a full-peak resonant transmission with $T_{\mathrm{res}} = 1$. As we can see, a phase-based scheme (red traces) provides a better sensitivity than a transmission-based scheme (blue traces), even with coherent states, $s = 0$.

The EQEF for resonant sensors based on phase and transmission are plotted in Fig. 3.6(b). As the squeezing parameter increases, the EQEF of the phased-based scheme grows faster than the EQEF for the transmission-based scheme, which indicates

that the phase-based scheme takes better advantage of the quantum correlations in the twin beam. However, this feature depends on the lineshape of the sensor's transfer function [71], and a transmission-based scheme can outperform a phase-based scheme for sensors with particular lineshapes.

3.5.1 Effect of Optical Losses

Real-life measurements and sensing setups are not ideal and include losses. To study more realistic operational conditions, we consider the effect of losses on quantum resonant sensors. As described by Eqs. (3.8) and (3.9), optical losses increase the uncertainty in transmission and phase, therefore, deteriorate the sensitivity of the resonant sensor for both sensing schemes. Also, as shown in Eq. (3.19), as optical losses external to the sensor increase, the quantum enhancement with the BTMSS is reduced and can lead to no enhancements. All sources of photon loss in the sensing setup, such as imperfect optics and photo-detectors, can be integrated into the loss parameters before and after the sensor in the probing path via η_{p1} and η_{p2}, respectively, and in the reference arm via η_r, according to the nomenclature used in Fig. 3.2.

Different states of light are also affected differently by optical losses happening at different points. The sensitivity of a resonant sensor probed with coherent states, for example, is not affected by the losses before the sensor, as we are keeping the number of photons probing the sensor unchanged as our resources. Moreover, since there is no reference beam for the sensing schemes with a coherent state, the sensitivity of a resonant sensor will be independent of η_r as well. However, the losses after the

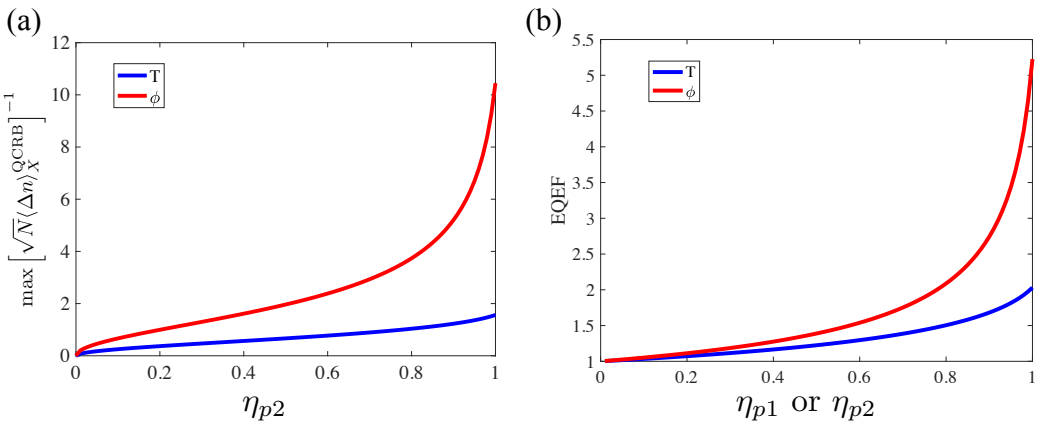

Figure 3.7: (a) Effect of optical losses in the probe beam after the sensor (characterized by η_{p2}) on the best sensitivities at the QCRB. (b) EQEF vs. optical losses in the probe beam before or after the sensor. Blue: transmission-based scheme, Red: phase-based scheme. $T_{\mathrm{res}} = 1$, $s = 2$.

sensor, η_{p2}, will deteriorate the sensitivity as photons containing information about the transmission or phase from the sensor will be lost. With a BTMSS, on the other hand, all three sources of loss reduce the fundamental sensitivity of the sensor, and the quantum enhancement will be limited when any of these losses exist. This is because optical losses make the QCRB with a BTMSS tend towards the one with a coherent state using either transmission and phase schemes.

The effect of optical losses in the probe beam after the sensor (η_{p2}) is shown in Fig. 3.7 for twin beams with $s = 2$ probing a sensor with $T_{\mathrm{res}} = 1$. The losses after the sensor not only increase the noise of the probe beam but also lead to the loss of the transmission and phase information from the sensor. As shown in Fig. 3.7(a), the maximum sensitivities of both schemes suffer from η_{p2}, but the phase-based scheme

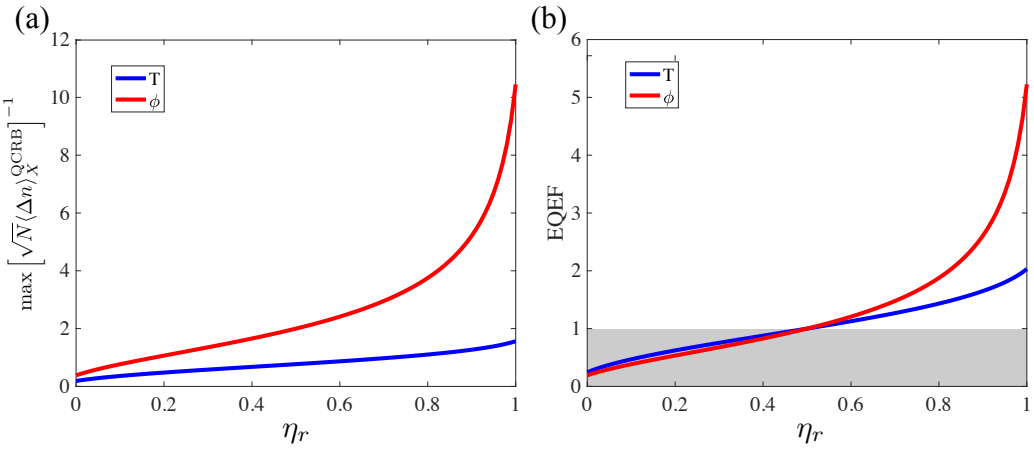

Figure 3.8: Effect of optical losses in the reference beam (characterized by η_r) on (a) the best sensitivities of the sensor at the QCRB and on (b) the EQEF, for our example full-peak Lorentzian resonant sensor, based on transmission (blue) and phase (red).

remains more sensitive for all levels of loss. On the other hand, losses in the probe beam either before or after the sensor have the same mathematical effect on the EQEF. As shown Fig. 3.7(b), optical losses in the probe beam before or after the sensor reduce the EQEF towards one, with the phase-based scheme always being able to take more advantage of the squeezing properties.

The effect of losses in the reference beam is shown in Fig. 3.8, for a BTMSS with $s = 2$ and a sensor with $T_{\mathrm{res}} = 1$. Even though the reference beam does not contain any information on the transmission and phase from the sensor and is only used to cancel the quantum correlated fluctuations, losses in this beam $(1 - \eta_r)$ still change the photon statistics of the BTMSS and reduce its quantum correlations. Therefore, losses in the reference beam increase the uncertainty of both sensing schemes based on

transmission and phase. As losses in this arm increase, the phase-based sensing scheme stays more sensitive than the transmission-based scheme, as shown in Fig. 3.8(a).

The optical losses in the reference beam also reduce the quantum enhancement when using a BTMSS, as shown in Fig. 3.8(b). At a critical point where the losses in the reference beam exceeds $(1 - \eta_r) = 1/2$, the uncertainties in transmission and phase schemes with the BTMSS cannot surpass the uncertainties with the coherent state, and the EQEF drops below one. This is because each mode of the BTMSS by itself has more uncertainty than the coherent states. This behavior can also be seen from Eq. (3.19). Under this condition, the sensor does not benefit from using squeezed states.

3.6 Figure of Merit

When we have access to either sensing scheme, it is worth studying which one allows us to obtain better sensitivities and take more advantage of the quantum properties of twin beams. To quantify such a comparison, we define the "figure of merit" (FOM) parameter as the ratio between the optimum resonant sensor sensitivities for the phase and transmission schemes at the QCRB:

$$\mathrm{FOM} = \frac{\min\limits_{\Lambda} \left\langle \Delta n \right\rangle_T^{\mathrm{bound}}}{\min\limits_{\Lambda} \left\langle \Delta n \right\rangle_\phi^{\mathrm{bound}}}, \tag{3.21}$$

where min refers to the wavelength where the sensitivity of each scheme reaches its best values. Here, we assume that we are able to tune the operating wavelength of the given resonant sensor to operator at the most sensitive wavelength for each

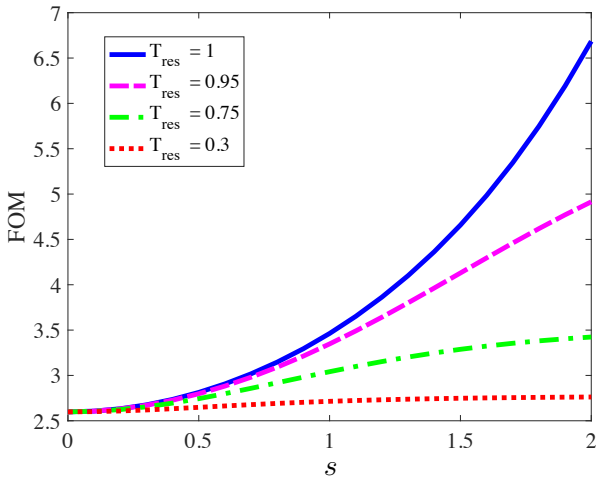

Figure 3.9: FOM vs. squeezing parameter for various values of T_{res}. The phase-based scheme outperforms the transmission-based scheme for a sensor with a Lorentzian peak-resonance lineshape.

scheme. A FOM greater than one quantifies how much the phase-based scheme can outperform the transmission-based one, and vice versa. Figure 3.9 shows the FOM vs. squeezing parameter, for different values of T_{res}. As we see from this figure, even with coherent states, the phase-based sensing scheme provides a higher sensitivity than the transmission-based one. Such a behavior is due to the particular lineshape of the resonant transfer function of the sensor. However, this advantage is not always there for lineshapes where the transmission response has sharper slopes. The FOM for those cases can fall below one, as shown in [71].

The results from this section and section 3.4.5 show two main rules of thumb for estimating the sensitivity of resonant sensors:

1. A BTMSS with a large squeezing level is more vulnerable to optical losses, either

external or internal to the sensor. Therefore, the optimum operating wavelength of the sensor tends towards higher transmissions, although the transmission slope is not the largest.

2. The overall sensitivity spectrum and the optimum operating wavelength of the sensor depend on the lineshape of the sensor's transfer function. As we show in [71], sensors whose transmission slope is sharper than a Lorentzian lineshape, can have better sensitivity for the transmission-based scheme than for the phase-based scheme. Different lineshapes can also affect the amount of quantum enhancement that the sensor can obtain in either scheme.

The method studied here can be generalized to any passive resonance-based sensor with a linear response.

Chapter 4

Plasmonic Sensors

An important example of an optical resonant sensor, discussed in chapter 3, is a plasmonic sensor. Plasmonic sensors are optical readout passive devices which are widely used in bio-chemical diagnosis and detection applications. These sensors have found a number of applications over the past two decades as they are sensitive to local changes in refractive index. As a result, they have been used for chemical and biochemical sensing applications as robust diagnostic tools, such as cancer diagnostics [99, 100, 2, 101], and virus detection [102], and other bio-sensing applications [103].

The response of a plasmonic sensor can be designed to tune the wavelength of its maximum sensitivity. This tunability allows us to design plasmonic structures that can operate with maximum sensitivity at the wavelength of the quantum-correlated states of light, such as the twin beams, used to probe them. Moreover, technological advances in nanofabrication allow us to manipulate metal thin films and fabricate nanoscale structured sensors with dimensions and geometries based on numerical simulations [104].

Plasmonic sensors rely on optical readout techniques and have already reached their fundamental detection limit at the SNL with classical resources [105]. Moreover, as will be shown in chapter 5, plasmonic sensors maintain the quantum properties of the twin beams, and hence are compatible with these states [72, 106, 107]. This compatibility makes it possible to enhance the sensitivity of plasmonic sensors with quantum states of light [108, 109]. Therefore, plasmonic sensors provide a great platform for providing

a quantum-enhanced sensitivity through the use of quantum states of light, which is the main goal of my dissertation work.

In this chapter, we show the general properties and the basic functionality of plasmonic sensors with subwavelength periodic nanohole arrays. Also, we study their response to changes in the refractive index of their surroundings. With the help of a simulation software, COMSOL Multiphysics, we study and predict the resonance excitation of plasmons and estimate the order of magnitude of their sensitivity to changes in the refractive index of the air. Experimental tests of the samples fabricated based on the dimensions from the simulation will also be presented. Finally, in this chapter we study the sensitivity of plasmonic sensors according to the notation presented in chapter 3.

4.1 Plasmon Excitation

The plasmonic sensors that we discuss in this section consist of a metallic layer between two dielectric materials. They are used for detecting changes in the refractive index of the dielectric environment in their proximity [28], as those changes will modify their boundary conditions. When an electromagnetic (EM) wave illuminates such a structure, electronic oscillations at the metal-dielectric interface can get excited, as shown in Fig.4.1, for a metal-dielectric interface. These excitations form a hybrid mode between the oscillations of the metallic electrons and the incident photons, which are called surface plasmon-polariton (SPP) modes [110, 111].

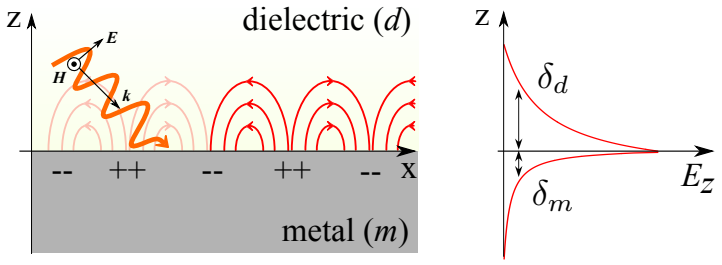

Figure 4.1: (a) SPP mode excitation at a metal-dielectric interface. (b) Evanescent field at the interface. The decay length into the dielectric material (δ_d) is of the same order of magnitude as the wavelength of the light, while the decay length into the metal (δ_m) determines the skin depth.

SPPs are EM modes that satisfy Maxwell equation boundary conditions at the metal-dielectric interface. Taking this interface to be in the $x-y$ plane and the illuminating field propagation direction to be in the $z-x$ plane, as shown in Fig. 4.1, the electric and magnetic components of a transverse magnetic (TM) mode of light can be written as:

$$\mathbf{E}_j(\mathbf{r},t) = (E_x, 0, E_{zj}) \exp[i(k_x x + k_{z_j} z - \omega t)], \tag{4.1}$$

$$\mathbf{H}_j(\mathbf{r},t) = (0, H_y, 0) \exp[i(k_x x + k_{z_j} z - \omega t)], \tag{4.2}$$

where $(E_x, 0, E_z)$ represents the electric field components with wavevector $(k_x, 0, k_z)$ in the plane of incidence $(z-x)$, and $(0, H_y, 0)$ represents the magnetic field along the y-direction. In this notation, the dielectric media are labeled as $j = d$, and the metallic layer is labeled by $j = m$, as shown in Fig. 4.1.

Due to the continuity condition of the field components at the metal-dielectric

boundary from Maxwell's equations, the tangential component of the electric field and the normal component of the magnetic field are continuous at the interface. Also, the normal component the electric field and the tangential component of the magnetic field are related to the surface charge and current densities, respectively. These boundary conditions lead to:

$$\begin{aligned} E_x = \tfrac{k_{z_j}}{\omega\epsilon_j} H_y \ , \quad E_{z_j} = -\tfrac{k_x}{\omega\epsilon_j} H_y, \\ \tfrac{k_{z_d}}{\epsilon_d} = \tfrac{k_{z_m}}{\epsilon_m} \ , \quad k_x^2 + k_{z_j}^2 = \epsilon_j k_0^2, \end{aligned} \tag{4.3}$$

where $k_0 = 2\pi/\lambda = \omega/c$ is the wavevector of the light field in vacuum (with ω the frequency of the incident light and c the speed of light in vacuum), and ϵ_j is the permittivity of $j = d$ the dielectric and $j = m$ the metallic layer. The dispersion relations for the excited modes of the field at the interface are obtained from the boundary conditions in Eq. (4.3), and can be written as:

$$k_x = k_0 \sqrt{\frac{\epsilon_d \epsilon_m}{\epsilon_d + \epsilon_m}}, \tag{4.4}$$

$$k_{z_j} = k_0 \frac{\epsilon_j}{\sqrt{\epsilon_d + \epsilon_m}}. \tag{4.5}$$

The permittivity of the dielectric media (ϵ_d) is real and positive, while the metallic layer has a complex permittivity with a negative imaginary part, that is $\epsilon_m = \epsilon_m' - \mathrm{i}|\epsilon_m''|$, where prime and double-prime represent the real and imaginary parts, respectively. Since the permittivity of the metal is complex, its corresponding k-vector becomes complex, indicating that the field dissipates as it propagates. Therefore, the components of the light normal to the metal-dielectric interface will exponentially damp along z-direction. These modes represent the perpendicular SPP modes and are called the evanescent

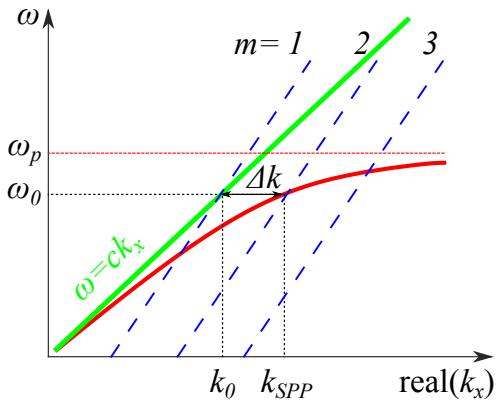

Figure 4.2: Frequency (energy) vs. momentum (real part of the k-vector) for the SPP excitations (red). A coupling mechanism is needed to compensate for the momentum mismatch Δk. Dashed lines indicate reciprocal lattice modes from a periodic hole array. ω_0 and k_0 are the frequency and the wavevector of the illuminating light in vacuum. ω_p is the plasma frequency of the metal layer. c is the speed of light in vacuum.

modes. On the other hand, the SPP modes that propagate along the x-direction at the interface are called the transverse SPP modes, $k_x = k_{SPP}$, as shown in Fig. 4.1.

To excite SPP modes, the momentum (k-vectors) and energy (frequency ω) of the incoming photons should match with the ones of the SPP modes. Such an energy-momentum relation for a plasmonic structure is determined by the frequency-dependent complex permittivity of the metallic layer as given by Eq. (4.4), where $\epsilon_m = \epsilon_m(\omega)$, and is plotted in Fig. 4.2. In this figure, ω_p indicates the plasma frequency, the frequency at which the free electron cloud inside the metal can be considered as an oscillating plasma.

The SPP modes cannot be excited directly in a metallic layer in air, and require a coupling device such as coupling prism made out of glass [112, 113]. This configuration, which is usually referred to as the Kretschmann configuration [114, 115, 116], allows us to compensate for the momentum mismatch Δk, and mediate the coupling of the momenta of the illuminating photons and the SPPs.

When monochromatic light excites the SPP modes on a metallic layer with a coupling prism, the k-vectors can be matched at certain angles depending on the thickness of the metal and the refractive index of the metal and prism. The plasmonic excitation can then be seen as a dip in the reflection spectrum of the incident light on the surface. Moreover, if the plasmonic structure allows coupling of SPP modes on both sides of the metallic layer, the structure can be used to operate in the transmission mode. In this case, the excitation of plasmons leads to a resonance peak in the transmission spectrum. Alternatively, we can excite SPP modes by coupling via gratings constructed by a periodic array of nanoholes [117], as we discuss in the next section.

The propagation length and the lifetime of the SPP modes along the surface can be calculated by finding the distance and the time over which the energy of the SPP modes drop by $1/e$ of its initial value along the metal-dielectric interface, and are given by:

$$\begin{aligned} \delta_{SPP} &= \frac{1}{2k''_{\mathrm{SPP}}} = \frac{(\epsilon'_m)^2}{\epsilon''_m k_0}\left(\frac{\epsilon'_m+\epsilon_d}{\epsilon'_m\epsilon_d}\right)^{3/2}, \\ \tau_{SPP} &= \frac{\delta_{SPP}}{v_g} = \frac{(\epsilon_d+\epsilon'_m)}{ck'_{\mathrm{SPP}}\epsilon_d\epsilon'_m}\frac{4\pi(\epsilon'_m)^2}{\epsilon''_m}, \end{aligned} \tag{4.6}$$

where k''_{SPP} is the imaginary part of the complex SPP wavevector and v_g is the group velocity of the SPP modes. The propagation length of SPP modes on a glass-silver interface, for instance, is ~ 20 μm (at 500 nm) [113], with a lifetime of 0.83 fs, where

we used $v_g \approx 0.8c$ for SPPs in silver [118].

Similarly, we can calculate the decay length of the evanescent waves along the z-direction into the metal and dielectric media, which are given by:

$$\begin{aligned} \delta_m &= \frac{1}{2k''_{mz}} \approx \frac{\lambda_0}{4\pi\sqrt{|\epsilon_m|}}, \\ \delta_d &= \frac{1}{2k''_{dz}} \approx \frac{\lambda_0}{4\pi}\frac{\sqrt{|\epsilon_m|}}{\epsilon_d}, \end{aligned} \tag{4.7}$$

where k''_z is z-component of the SPP wavevector in each media. The decay length for the dielectrics is on the order of the wavelength of the illuminating light, and determines the depth of the light confinement near the metal-dielectric interface. On the other hand, the decay length for the metals defines their skin depth which are usually an order of magnitude smaller than the wavelength of the illuminating light. For example, the skin depth of silver is ~ 3 nm at $\lambda = 800$ nm [119]. If the thickness of the metal is less than its skin depth δ_m, the SPP on both sides of the metal can couple, permitting a direct transmission of the incident light through the structure. On the contrary, if the thickness of the metal is greater than its skin depth, the evanescent wave decays exponentially and cannot transmit through the metallic layer.

4.2 Extraordinary Optical Transmission

When we have a two-dimensional diffractive grating composed of nanoholes, the dispersion relation for the k-vectors on the metal-dielectric interface takes the form:

$$\vec{k}_{SPP} = \vec{k}_x \pm p\frac{2\pi}{P_x}\hat{\mathbf{x}} \pm q\frac{2\pi}{P_y}\hat{\mathbf{y}}, \tag{4.8}$$

where $\vec{k}_x$ is the wavevector of the illuminating light from the dielectric material, P_x and P_y are the periodicities of the nanohole array along the x- and y-directions, respectively, and p and q positive integers corresponding to the SPP excited modes at each direction. Assuming a square grating with $P_x = P_y = P$, a light field with wavelength λ_0 in free space can be coupled to the SPP modes if:

$$\lambda_0 = P\sqrt{\frac{1}{p^2+q^2}\frac{\epsilon_m\epsilon_d}{\epsilon_m+\epsilon_d}}, \tag{4.9}$$

where $\epsilon_d = n^2$ is the permittivity of the dielectric medium (n is the refractive index), and ϵ_m is the complex permittivity of the metallic film.

Ebbesen in 1998 discovered an extraordinary transmission of light through an array of periodic subwavelength nanholes in metal films [120, 121, 122], orders of magnitude larger than predictions by diffraction theory. Localized plasmonic excitations at each nanohole can couple to the localized excitations on the back side of the metal that is not illuminated. This coupling allows a coherent photon-plasmon-photon conversion process that leads to the transduction of light through the nanohole arrays. This process is called "extraordinary optical transmission" (EOT) [123]. It is extraordinary because it gives a result that cannot be predicted with diffraction theory. First, the thickness of the metallic layer is larger than the skin-depth of the metal. Hence, the metallic layer is opaque to the incident EM waves. Also, the size of the nanoholes are smaller than the wavelength of the incident light. According to classical aperture theory, as developed by Bethe [124], the direct transmission of light (at wavelength λ) through a

sub-wavelength hole (with diameter $a \ll \lambda$), is proportional to

$$T \propto \frac{a^6}{\lambda^4}. \tag{4.10}$$

Considering these results from diffraction theory, EOT through the periodic nanohole pattern in a metallic layer can only be possible via the photon-plasmon-photon coupling effect [121].

When a periodic nonohole array in a metallic film is illuminated with broadband light, particular wavelengths satisfy the EOT resonance condition. Each plasmonic nanohole structure has a characteristic EOT spectrum which defines its transmission transfer function $T = T(\lambda)$. There are various designs for the periodic subwavelength nanoholes and nanomaterials to excite EOT plasmonic modes. The geometrical dimensions, such as the size and periodicity of these structures, the thickness of the metallic layer, and the optical properties of the metal and dielectric media, determine the resonance wavelength and the lineshape of different EOT modes. Therefore, by optimizing the geometrical parameters of the periodic nanholes, we can tune their EOT response towards a particular wavelength of interest.

In the next two sections, we define the methods we use to obtain the transfer function of a given nanohole structure either by numerical calculations from simulations or by direct experimental measurements.

4.2.1 COMSOL Simulation

4.2.1.1 What is COMSOL?

The interaction and resonance condition of an EM wave with a periodic nanohole array can be simulated by solving Maxwell's equations with correct boundary conditions at the metal-dielectric interface. Here, we use a commercially available software, called COMSOL Multiphysics, which is a simulating package based on finite element method (FEM) techniques to solve partial differential equations. COMSOL allows us to couple various physical problems, such as heat transfer, dynamics, fluid-flow, electromagnetism, and other physical phenomena together. Here, we only focus on the RF module, which can solve Maxwell equations in different 2D and 3D domains with specific boundary conditions. Optical properties, such as frequency-dependent index of refraction or permittivity of the materials can be imported from reference tables or from the material library of the software. Also, the geometrical domains of the model can be either imported from a 3D CAD software (requires separate license) or can be drawn in its own graphical interface. However, since the accuracy of simulations depends on the size of the simulation elements (mesh size), it is very memory-intensive and might take several days to perform high resolution calculations.

Post-processing tools in COMSOL allow the user to generate 2D and 3D visualizations of different built-in and user-defined variables, such as field concentrations, charge density on the surface and in bulk, and several more.

4.2.1.2 Simulation Setup: Boundary Conditions

To simulate the interaction of an arbitrarily polarized EM wave with a subwavelength nanohole array, the boundary conditions need to be defined properly in different media. Since it is not possible to model all the nanoholes in the array, we model a single unit cell containing one hole. By using periodic boundary condition (PBC) in the $x-y$ plane, we define an infinite array of nanoholes along the x- and y-directions, which is a good approximation for the typical size of our plasmonic structures ($\sim 200\mu\text{m} \times 200\mu\text{m}$). Therefore, we define a through-hole with the desired geometry in a cuboid with dimensions P_x and P_y representing the periodicity along the x- and y-directions, and height t defining the thickness of the metallic layer, as shown in Fig. 4.3. Also, a slab of glass with the same dimensions of the silver unit cell in the x- and y-directions is defined as the substrate below the silver film. Another slab is defined above the silver film to represent the air around the structure. The thickness of the dielectric materials is chosen to be several times larger than the dielectric propagation length (δ_d) to avoid transient evanescent responses near the surface of the structure. In order to truncate the infinite length of the dielectric domains above and below the domain of interest, we use a perfectly matched layer (PML) domain on top and below the dielectric slabs. The PML domains absorb the incoming light to avoid unwanted reflections of the field at the boundaries and back into the simulation domain. Finally, we import the wavelength-dependent real and imaginary parts of the electric permittivity for silver and glass from online references [125].

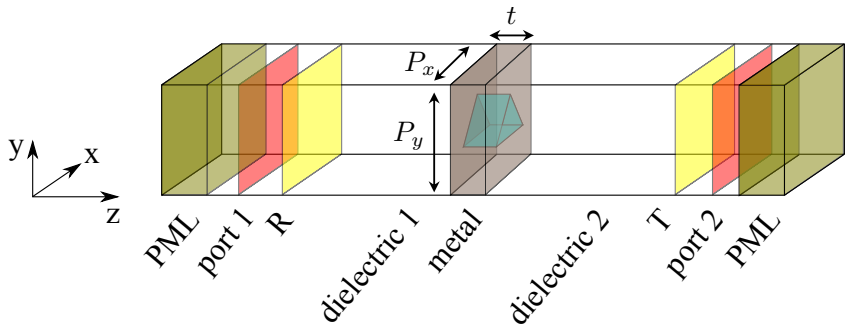

Figure 4.3: Unit cell for simulation with COMSOL. All four planes parallel to the $z-x$ or $y-z$ planes are set to PBC. The R and T planes are used for integrating over the field to obtain intensities for reflection and transmission calculations, respectively.

As shown in Fig. 4.3, an electric field enters from port 1 right after the PML layer, interacts with the nanohole in silver layer, and exits from port 2, right before the second PML layer. To define the "input port", where the illuminating field enters the simulation domain, we turn on the "field excitation" of port 1 and we turn off the field excitation of port 2 defining the "output port". These setting for the input and output ports determines the direction of the EM energy flow.

Since the nanohole structure is periodically repeating along the x- and y- directions, we set PBC on the four planes parallel to the $z-x$ or $y-z$ planes, as shown in Fig. 4.3. This means that the k-vectors of the field are exact copies of each other on the opposite PBCs, and repeat over an infinite extent. The PBC also allows us to calculate the diffraction orders reflected or transmitted at the input and output ports. Depending on the symmetry of the desired nanohole shape, we can also use perfect electric conductor

(PEC) or perfect magnetic conductor (PMC) boundary conditions, and model only half or a quarter of the unit cell. These boundary conditions are the same as continuity of the tangential or normal components of the electric or the magnetic field components at each boundary.

4.2.1.3 COMSOL Simulation Results

Through COMSOL simulation, we can optimize the shape and dimensions of the nanoholes to find the most sensitive response at the desired wavelength. By properly setting up the input field and the material properties, as well as the mesh size and mesh distribution in the three materials, we can solve for the propagation of the EM field as a function of wavelength, resulting in the transmission spectrum through the structure. Using mathematical integration functions in COMSOL, we integrate over the EM field at two analysis surfaces near the input and output ports to calculate the reflected and transmitted EM energy from the metallic film and the glass domains. These two surfaces are placed just after the input and output ports parallel to the silver-dielectric interface, as shown by the R and T planes in Fig. 4.3. We can then find the resonance wavelengths and the electric field distribution on the metal-dielectric interface of the nanohole array, as shown in Fig. 4.4 for a periodic triangular nanohole array. The concentration of the electric field at edges of the nanoholes and the resonance peak (or dip) in the transmission (or reflection) spectrum are typical signatures indicating the excitation of the SPP modes.

In this thesis, we are interested in designing periodic nanohole arrays for plasmonic

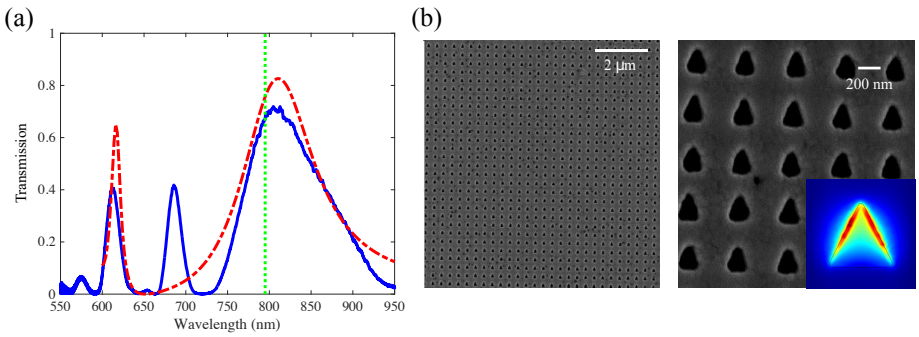

Figure 4.4: (a) EOT spectrum for triangular nanoholes in a silver film between glass and air obtained from COMSOL simulations (dashed red trace) and white light spectroscopy (blue solid trace). Green dotted line indicates wavelength of the twin beams at $\lambda = 795$ nm. (b) SEM images of the triangular nanoholes. The electric field concentrations at the edges of the nanoholes were obtained by COMSOL simulations.

sensing with twin beams. Therefore, our aim is to have sharp resonances as well as a high intensity transmission at or near $\lambda = 795$ nm. The first nanohole plasmonic sensors that we used in our experiments were composed of triangular nanoholes in a silver film and were fabricated by our collaborators at Oak Ridge National Laboratory (ORNL). This structure has a resonance near 800 nm and is suitable for our quantum sensing applications. For this triangular nanohole array, we scan over different parameters to tune the resonance response to have the sharpest slope as well as the maximum transmission (least losses) at this wavelength.

The effect of scanning over some parameters of the triangular nanoholes is listed in table 4.1. These results provide a guide to design and predict the resonance wavelength

Increase in	Shift of Resonance	Magnitude of Resonance
h_{tri}	to higher wavelengths	increases
b_{tri}	to lower wavelengths	increases
P_x	to higher wavelengths	decreases
t_{sil}	to lower wavelengths	decreases

Table 4.1: Effect of scanning over selected parameters of the triangular nanohole arrays on the main EOT plasmonic resonance peak. h_{tri} is the height and b_{tri} is the base of the triangles. t_{sil} is the thickness of the silver layer. P_x is the periodicity of the nanoholes along the incident E-field polarization.

for fabrication purposes. The behavior of some of these parameters is not restricted to the triangular nanoholes and can be generalized to other nanohole shapes. For example, increasing the periodicity of the nanoholes along the polarization of the incident electric field shifts the resonance wavelength towards higher wavelengths (red-shift) which is consistent with Eq. (4.9).

4.2.2 Fabrication of Nanohole Structures

Advances in nanofabrication technologies have allowed us to write, cut, and drill metals to fabricate nanohole geometries based on the numerical simulations. Periodic arrays of nanoholes can be fabricated in metallic layers using standard top-down nanofabrication techniques [126]. The EOT-based plasmonic nanohole structures that we study in

this thesis are fabricated with two different methods at ORNL and Sandia National Laboratory: electron-beam lithography (EBL) and focused ion-beam (FIB) lithography. Therefore, we only focus on these two methods.

During the 1970s, through the developments of the scanning electronic microscope (SEM), researchers noticed that an electron beam could damage some materials. These findings led to the invention of electronic beam lithography [127]. In this method, an electron beam is focused on a poly-methyl methacrylate (PMMA) layer as an electron-sensitive resist material, to drill the nanoholes. The electron beam is then scanned over the sample to mill the nanoholes one-by-one. The typical voltages for electron beam fabrication is between 10-100 kV, which provides a de Broglie wavelength as small as 1 Angstrom and resolutions on the order of 10 nm [104, 128]. The sample is finally baked to enhance the adhesion of the metal to the substrate.

The FIB lithography method [129] is used to directly fabricate nanoholes in metals by utilizing a low energy ion beam to ablate material from a metallic layer by collision. In the FIB technique, the ion beam is generated from a liquid metal that can flow on a sharp tungsten needle, such as gallium. By applying a voltage between the metal source and a target aperture, ions will be emitted into a sharp cone. This voltage can also control the incursion depth of the ion beam into the metallic target layer. The ions can be focused on a tip with dimensions on the order of several nm for milling the desired nanohole pattern on the metallic layer. With the FIB method, the smallest size of the tip can get as small as 10 nm.

During the FIB milling, the sputtered materials will be redeposited and relocated

on the substrate or the sample itself. This limiting factor can be reduced by using a gas injection system. Moreover, the FIB method provides a serial lithographic technique for direct milling of nanohole patterns, with high-resolution and without the need of the mask. However, this method is time-consuming and expensive, which make it not suitable for mass production [104, 128].

The fabricated structures in silver with either method are usually spin-coated with a PMMA layer to prevent oxidation of the silver in ambient air. The oxidation will deposit on and through the nanoholes and fill them, leading to a broadening of the plasmonic resonance with a less efficient EOT. Washing this protecting layer shifts the resonance to lower wavelengths.

4.2.3 White Light Spectroscopy

The characteristic EOT spectrum of a given plasmonic structure can be experimentally measured with a white light spectroscopy setup, as shown in Fig. 4.5. In this setup, the white light beam from a Halogen lamp (Osram 64641-HLX-G6.35, $\lambda = 550\,\text{nm} - 1100\,\text{nm}$) is coupled to a broadband fiber optic (Ocean Optics: P1000-2-VIS-NIR) to form a uniform spatial mode. The output light from the fiber passes through a Glan-Thompson polarizer to linearly polarize it. A broadband half-wave-plate (HWP) allows us to control the polarization of the light to illuminate the nanohole structure. A lens system is then used to collimate and control the size of the beam on the sample. After the plasmonic sample, another lens system directs the beam to a beam profiler (a charge-couple device-CCD camera) to monitor the beam size with respect to the sample area

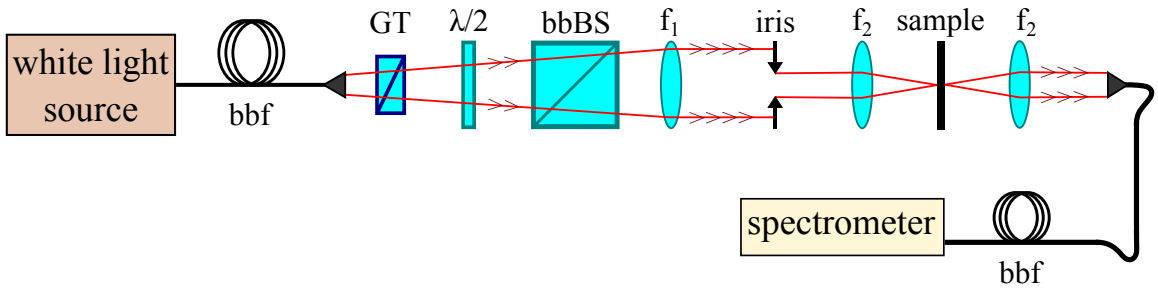

Figure 4.5: Experimental white light spectroscopy setup for characterizing the EOT response of a plasmonic sensor.

and align the center of the plasmonic sample to the input light. After ensuring that the light is not leaking from the finite size of the plasmonic sample (in our experiments $\sim 200\ \mu\text{m} \times 200\ \mu\text{m}$), the transmitted light is coupled to a broadband multi-mode fiber optic to be analyzed with a spectrometer. The spectrometer (Thorlabs: CCS100) shows the power spectrum of the light received from the sample.

By rotating the broadband HWP before the sample, we can align the polarization of the input light along with or normal to the periodic axis of the nanoholes. When the polarization is aligned with the periodic axis of the nanohole array, the EOT spectrum shows the maximum resonance response to the incoming light. Finally, to take into account the effects of optical loss and the polarization dependence of the glass substrate, we normalize the transmitted power through the plasmonic structure to the transmitted power through the glass portion of the sample, for the corresponding linear polarization angle. The sample is mounted on a 3-dimensional translation stage for alignment and to move between the plasmonic structures and the glass substrate. The

normalized transmission from the sample gives the absolute power transmitted through the nanohole plasmonic array. An example measurement of the normalized transmission spectrum for a given triangular sample is shown in Fig. 4.4(a).

4.3 Plasmonic EOT for Sensing Applications

4.3.1 Resonance Shift

A given plasmonic nanohole structure has a characteristic EOT resonance response for transmission or reflection. This response depends on the geometric shape, dimensions, and the periodicity of the nanoholes, as well as the thickness of the metal film, the refractive index of the metal and the surrounding dielectrics, and the properties of the probing light, such as its polarization and angle of incidence. All of these parameters can act as tuning knobs to set the response of the plasmons to the desired wavelength. Therefore, the resonance wavelength and the sensitivity of these sensors can be tuned by changing these parameters, with some of them listed on table 4.1.

For a given nanohole structure, changes in the refractive index of the dielectric media shifts the EOT resonance of the plasmonic nanohole structure. This shift allows us to use the EOT structure as a sensor for changes in refractive index of its neighboring environment. In this thesis, we are interested in using the plasmonic nanohole arrays as sensors of the refractive index by using such shifts in the resonance response. We can observe these changes by gradually increasing the refractive index of the environment using COMSOL simulations or experimentally with the white light spectroscopy setup.

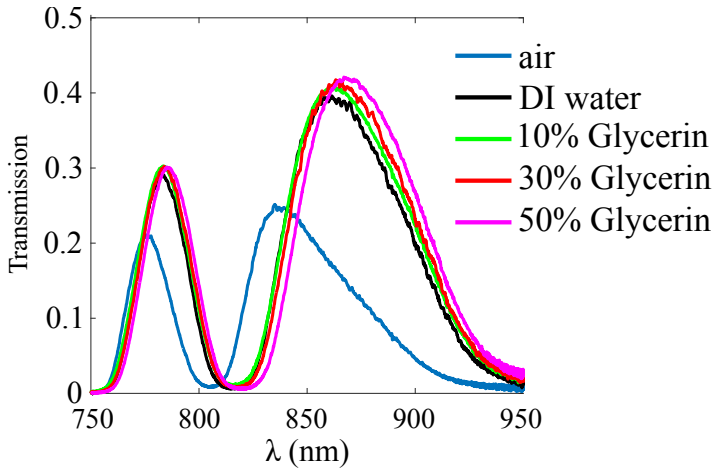

Figure 4.6: The EOT spectrum shifts with changes in the index of refraction as a result of increasing the concentration of Glycerin in water. The plasmonic sensor has periodic triangular nanoholes, as those in Fig. 4.4.

To experimentally characterize the response of our plasmonic structure to changes of refractive index, Δn, we generate large changes in refractive index to generate visible shifts in the EOT spectrum of the sample. We place the sample inside a sealed chamber, initially filled with air. Then we fill the chamber with deionized (DI) water. Due to the increase in the refractive index from $n = 1.000$ (air) to $n = 1.333$ (water), the EOT spectrum shifts to higher wavelengths, as shown in Fig. 4.6. We further shift the EOT spectrum by further increasing the refractive index inside the chamber using incremental concentrations of Glycerin in water. We add Glycerin, which is a water-soluble liquid, to the DI water by weight percentages. Also, to prevent contamination from different weight percentages of Glycerin, we clean wash the chamber after measurements with the previous concentration before taking the white light spectroscopy with the new Glycerin concentration. Figure 4.6 shows the the EOT spectrum shifts to higher wavelengths

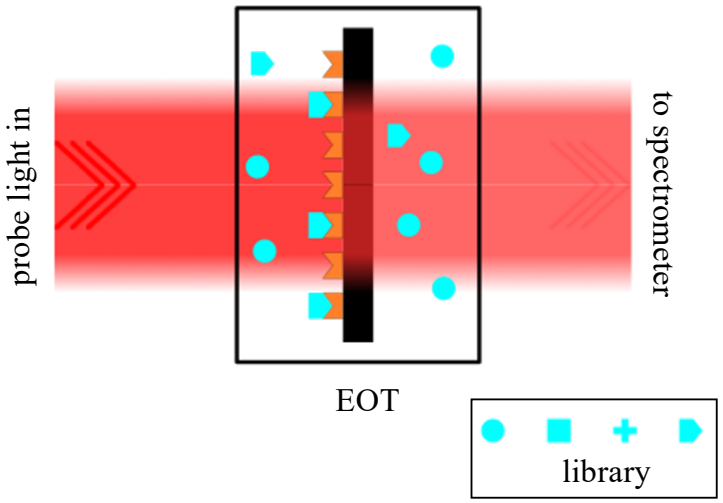

Figure 4.7: Plasmonic sensors can be used to detect certain bio-chemical stimuli, or contaminating elements in a sample flowing through a flow cell. With this configuration, only target particles can attach to the functionalized plasmonic sensor and, therefore, their existence can be detected by the shift in resonance. By making a library of indicators we can use different sensors for detecting different binding particles. Figure inspired by [103] licensed CC by 4.0 International.

as we increase the concentration of Glycerin from 0% (pure DI water) to 50% (weight percentage), corresponding to $\Delta n = 0.065$ RIU* associated with the % of Glycerin [130].

4.3.2 Plasmonic EOT for Sensing

Similar to their parent category of optical resonance sensors that we introduced in section 3.4, plasmonic structures can be used as sensors for detecting changes in the

*RIU: refractive index unit

refractive index. The characteristic EOT resonance of the nanohole structures shifts due to changes in the refractive index (Δn) of the surrounding dielectrics (air and glass). Such shifts change the transmission of the probing beam at a fixed wavelength and polarization of the incident probing light [28, 131, 132, 133, 134, 135]. These changes in the transmission can be detected with a photodetector as long as they are larger than the noise of the measurement. Therefore, a plasmonic nanohole array, similar to a resonance sensor, can be used to sense a change in the refractive index of its neighboring environment, due to temperature, pressure, concentration, or density of the surrounding materials. As pictorially shown in Fig. 4.7, plasmonic bio-chemical sensors usually use binding materials that only attach to specific materials to make it possible for it to detect specific target analytes through the detection of transmission changes [81, 103]. Therefore, EOT plasmonic sensors provide direct sensing suitable for label-free sensing applications [84, 136].

4.3.3 Order of Magnitude Estimation of Sensitivity

We can estimate the order of magnitude of the sensitivity of the plasmonic sensor with triangular nanoholes that we use in our quantum sensing experiments. As defined in chapter 3, the sensitivity is defined as the smallest change in the refractive index that the sensor can resolve from noise:

$$\langle \Delta n \rangle_{\min} = \frac{1}{|\partial T/\partial \lambda|} \frac{1}{|\partial \lambda/\partial n|} \frac{\langle \Delta I \rangle}{|\partial \hat{I}/\partial T|}, \tag{4.11}$$

where $\hat{I}$ is the intensity of light on the photodetector, which depends on the transmission spectrum of the plasmonic sensor, as $\hat{I} = \hat{I}(T(\lambda))$.

The first term on the right hand side of Eq. (4.11) represents the slope of the transmission spectrum at the wavelength of the probing light. We can directly measure the transmission spectrum and its slope with respect to the wavelength for the refractive index of air, $n = 1$. The typical slope of the measured transmission spectrum is $|\partial T/\partial\lambda| \sim 0.005$ nm^{-1} at $\lambda = 795$ nm.

The second term on the right hand side of Eq. (4.11) gives the rate of the shift in the resonance (transmission) peak in response to changes in refractive index. By taking the direct derivative of Eq. (4.9), we have [137]:

$$\left|\frac{\partial\lambda}{\partial n}\right| = \frac{P}{\sqrt{p^2+q^2}}\left(\frac{\varepsilon_m}{n^2+\varepsilon_m}\right)^{3/2}. \tag{4.12}$$

Using the designed nanohole dimensions of our plasmonic structures, $P \sim 400$ nm, $n = 1$ for air, and $\varepsilon_m = -24.5 + i1.83$ at $\lambda = 795$ nm [138], we estimate $|\partial\lambda/\partial n| \sim 500$ nm/RIU for the first order mode of SPP excitations, $p = 1$ and $q = 0$. We can also verify this result from COMSOL simulations. To do so, we simulate the transmission spectrum through the nanohole structure for various incremental values of the refractive index ($\delta n = 0.0001$) and track the shift in the resonance peak.

According to Eq. (4.11), the sensitivity of the plasmonic sensor also depends on the noise and intensity of the probing light, according to $\langle\Delta^2\hat{I}\rangle/|\partial\hat{I}/\partial T|^2$. The EOT spectrum of the plasmonic sensors changes the intensity of the probing light with a mechanism similar to the one introduced by optical losses. As introduced in Eq. (2.40),

optical losses transform the field operator ($\hat{a}$) as:

$$\hat{a} \rightarrow \sqrt{T}\hat{a} + \sqrt{1-T}\hat{a}_v, \tag{4.13}$$

where T is the intensity transmission and $\hat{a}_v$ is the corresponding vacuum mode that couples in as a result of the losses introduced by the plasmonic sensor. The mean and variance of the light intensity after probing the sensor would then become:

$$\langle \hat{I} \rangle = T\langle \hat{I} \rangle_0 \tag{4.14}$$

$$\langle \Delta^2 \hat{I} \rangle = T^2\langle \Delta^2 \hat{I} \rangle_0 + T(1-T)\langle \hat{I} \rangle_0, \tag{4.15}$$

where $\langle \hat{I} \rangle_0$ and $\langle \Delta^2 \hat{I} \rangle_0$ represent the mean and variance of the probing light before the sensor. For the case of a coherent state, the variance is equal to its mean photon number, that is $\langle \Delta^2 \hat{I} \rangle_0 = \langle \hat{I} \rangle_0$. Therefore, $\langle \Delta^2 \hat{I} \rangle = T\langle \hat{I} \rangle_0$, and $|\partial \hat{I}/\partial T| = \langle \hat{I} \rangle_0$. Putting these together, we have:

$$\frac{\langle \Delta \hat{I} \rangle}{|\partial \hat{I}/\partial T|} = \sqrt{\frac{T}{\langle \hat{I} \rangle_0}}. \tag{4.16}$$

According to this result, the sensitivity scales inversely with the square root of the number of photons probing the sensor. For example, a probing light with the optical power of $P \approx 70$ μW corresponds to a photon flux of $F = P/h\nu = P\lambda/(hc) = 2.8 \times 10^{14}$ photons/sec at $\lambda = 795$ nm. Thus, for a measurement bandwidth of 1 Hz, $I_0 \sim 1.5 \times 10^{14}$ photons.

Substituting the individual parts discussed above in to Eq. (4.11), we can estimate the order of magnitude for the sensitivity of our designed plasmonic sensor to be on the order of 10^{-7} RIU/$\sqrt{\text{Hz}}$ for a single measurement. To estimate the absolute value

of the sensitivity, the effective bandwidth of the detector and the number of averages implemented need to be taken into account. As we will see in chapter 5, this estimation matches well with the measured values for the absolute sensitivities of the plasmonic sensor that we use in our experiment.

4.4 Novel Nanohole Structures

To design nanohole structures with sharp resonance and large transmission at the operating wavelength, we use COMSOL to simulate the EOT spectrum for different nanohole structures. Using these structures, different parameters of the nanohole in the unit cell can be used to tune the resonance EOT of the structure. For example, as shown in Fig. 4.8(a), by changing the width of square nanoholes (parameter l), we can tune the wavelength of the resonance peak or make it narrower [139].

Breaking the symmetry of the nanohole arrays would lead to sharp EOT resonances [28]. For example, by using two nanoholes in a unit cell, the EOT resonance response demonstrates a sharp resonances on top of a broader spectrum from the symmetric structures with single nanohole unit cells, as is shown in Fig. 4.8(b). The depth of the sharp resonance can be adjusted by changing the separation between the two nanoholes in the unit cell. The interference resonance response of such two nanohole unit cells is due to a collective response from a large number of such unit cells. Therefore, even small imperfections in the fabrication process can lead to reducing this sharp feature.

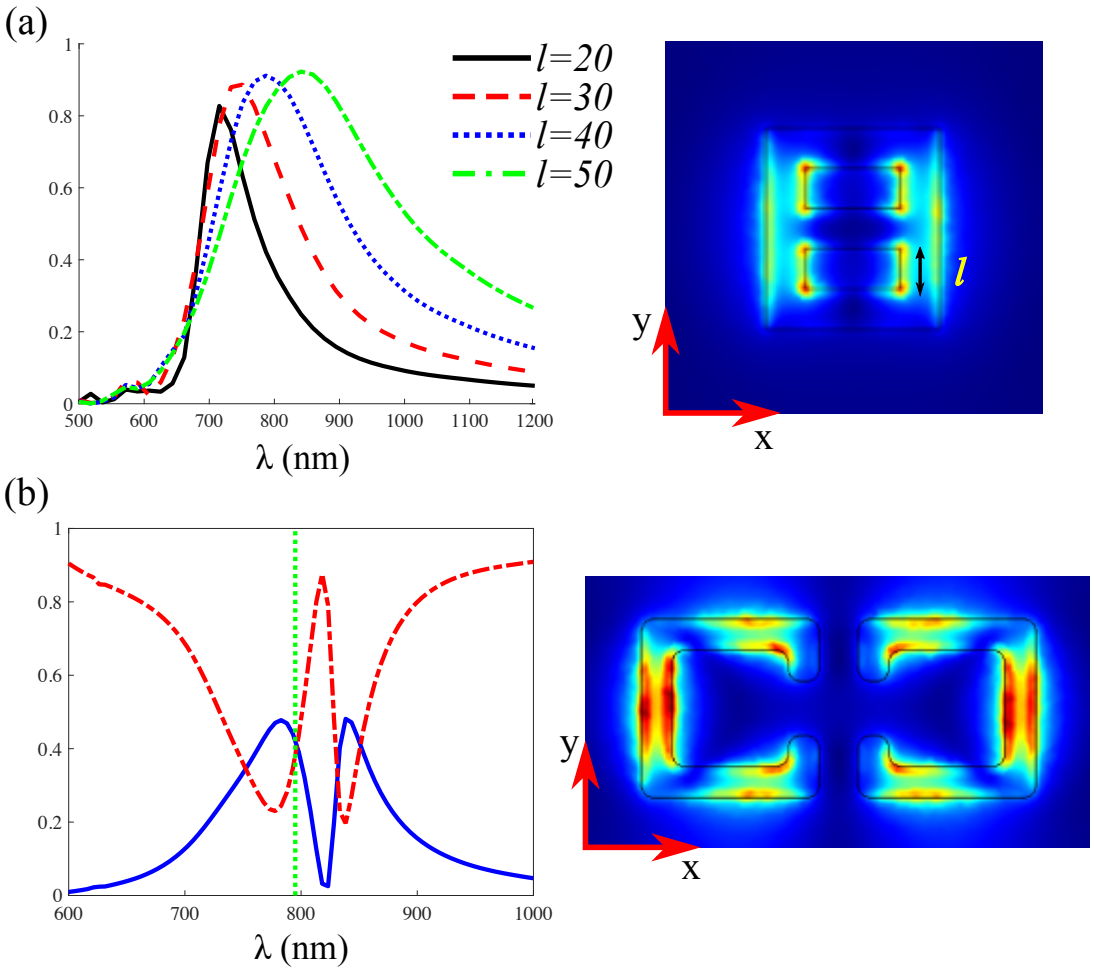

Figure 4.8: Sample transmission spectra from COMSOL simulations for nanoholes in a silver film between glass and air. (a) Transmission spectra for square hole arrays with different l- sizes. (b) Transmission (blue) and reflection (red) spectra for asymmetric C-flipped-C nanoholes. Green dotted lines indicate the wavelength of the twin beams at $\lambda = 795$ nm.

To alleviate the complications associated with the fabrication of small features, we can simplify the nanohole structures and use circular nanoholes instead. The transmission and reflection spectra from such circular structures are shown in Fig. 4.9, for nanohole arrays perforated in a gold film on a silicon substrate. In this figure, the polarization of the electric field of the illuminating light is along the x axis. Compared to the C-structures, the circular nanoholes have less transmission, but less loss in reflection. Since we are interested in large "transmissions" and sharp slopes for plasmonic sensing applications with twin beams, we can use the circular nanoholes in a reflection configuration.

When each unit cell contains a single nanohole, the symmetric distribution of the nanoholes with periodicity $P_x = 2P_y$ leads to a resonance dip in the reflection (or a peak in transmission) spectrum at wavelengths near the periodicity of the unit cells, as shown in Fig. 4.9(a). Keeping the periodicity along the x-direction the same, $P_x = 2P_y$, if we now put two circles in each unit cell asymmetrically, the resonance becomes sharper, as shown in Fig. 4.9(b). When the separation between the two holes (center to center) in each unit cell reaches the distance that makes the nanohole array symmetric inside the unit cells with periodicity $P_x = P_y$, the sharp EOT dip resonance due to the asymmetric unit cells disappears, as shown in Fig. 4.9(c). For this condition, the periodicity along the x-direction is half of the rectangular unit cells. Therefore, the first order EOT resonance falls at lower wavelengths. For an electric field with polarization along y-direction, all of the three structures shown in Fig. 4.9 have the same response, as the periodicity along this direction is fixed at $P_y = 392$ nm.

As we can see from these figures, the results from COMSOL simulations match fairly well with the experimental results. These samples were fabricated at Sandia National Laboratory, and more detailed analysis of their behavior is presented in [140].

COMSOL simulation also allows us to design other novel structures with the goal of reaching higher sensitivities with twin beams of light. By tuning the periodicity of the nanoholes along the x- and y-directions, we can design a periodic nanohole array that has slightly different pitches along the x- and y- directions, as shown in Fig. 4.10. Therefore, the resonance response of the structure at the operating wavelength will be slightly shifted for an incident field with both polarization components along the x- and y-directions [141]. Such geometry allows us to probe the sensor with two orthogonal polarization modes and obtain slightly different responses.

As shown in Fig. 4.10, illuminating this structure with two beams of light linearly polarized along the x- and y-direction, each beam experiences a different transmission and an opposite transmission slope at $\lambda = 795$ nm, for instance. This structure is particularly interesting for our ID measurement with the twin beams, where we can probe the sensor with both beams. In this configuration, the ID cancels the common quantum and classical noise while the changes in transmission have opposite signs for the twin beams as they observe opposite slopes in transmission. This behavior leads to an enhancement of the signal-to-noise ratio, compared to the case of probing the sensor with only the probe beam [142]. We are currently exploring this sensing configuration. Initial samples fabricated at Sandia National Laboratory show transmission spectra as predicted by COMSOL. Experimental and theoretical studies for implementing such a

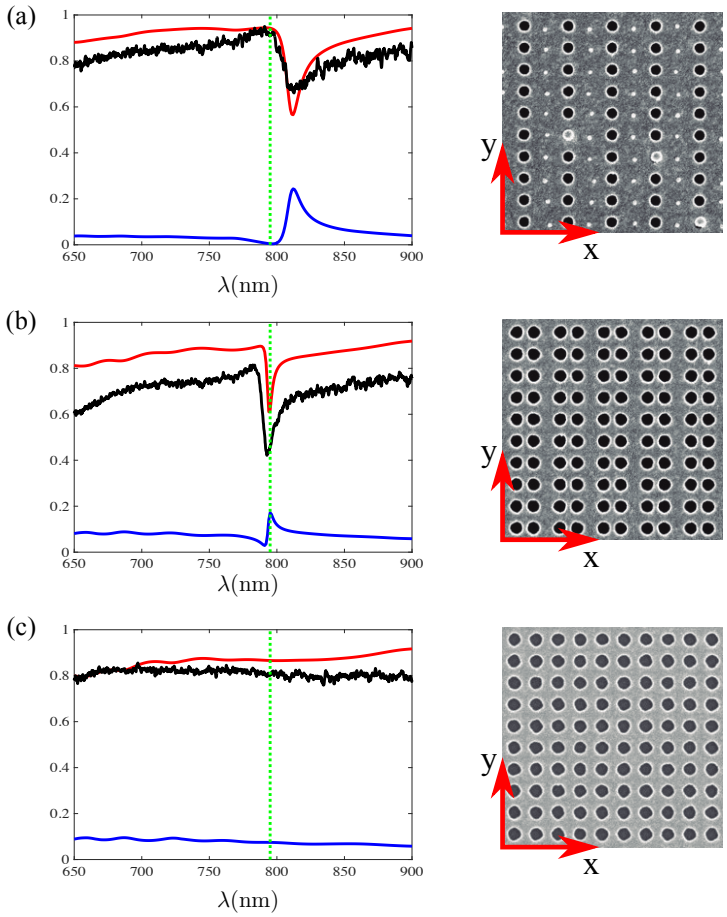

Figure 4.9: Transmission (blue) and reflection spectra from COMSOL (red), and experimental reflection spectrum (black) for circular nanoholes in an 80 nm thick gold layer on a silicon substrate. (a) Rectangular unit cell with single circular hole ($P_x = 2P_y = 784$ nm). (b) Rectangular unit cell with two circular holes ($P_x = 2P_y = 784$ nm): breaking the symmetry of the nanoholes at each unit cell leads to a sharper reflection dip. (c) Square unit cell with single circular hole ($P_x = P_y = 392$ nm). Right column shows the SEM images. Circle diameters: 210 nm. Green dotted lines indicate the wavelength of the twin beams at $\lambda = 795$ nm.

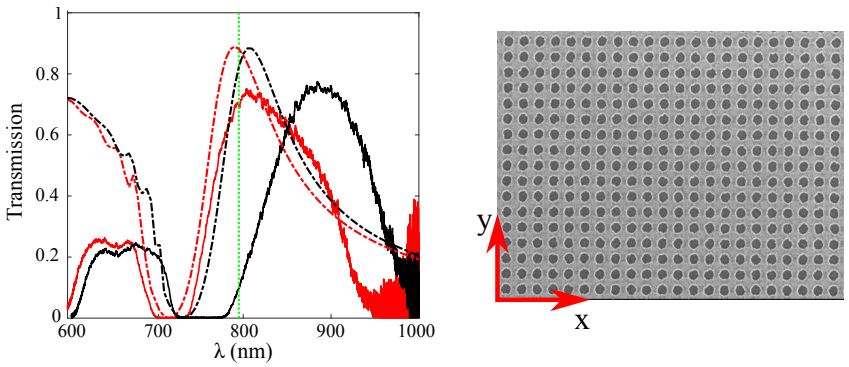

Figure 4.10: Experimental (solid) vs. simulation (dashed) EOT spectra of nanohole array with different periodicities exhibit opposite transmission slopes at $\lambda = 795$ nm (green dotted line) for an illumination with the electric field polarized along the x-axis (red) and along the y-axis (black). $P_x = 478$ nm, $P_y = 485$ nm, diameter 287 nm.

quantum-enhanced sensing configuration is currently ongoing.

Chapter 5

Implementation of Quantum-Enhanced Plasmonic Sensing

In previous chapters, we introduced the building blocks needed to implement quantum sensing. In this chapter, we demonstrate a quantum-enhanced plasmonic sensing configuration to detect changes in the refractive index of air induced by ultrasonic waves. While there have been proof-of-principle experimental and theoretical studies of quantum-enhanced plasmonic sensors [24, 75, 109, 143, 144], our results represent the first implementation of such a sensor with a sensitivity of the same order of magnitude as the classical state-of-the-art. Although we focus on quantum enhancement for plasmonic sensors, the techniques used can be generalized and implemented with other compatible sensors and measurements that already operate at the SNL.

In this chapter, we first prove that plasmonic sensors are compatible with our twin beams and can maintain their spatial information as well as their temporal entanglement properties. The compatibility of plasmonic sensors with temporal entanglement is used in this chapter, while the spatio-temporal quantum correlations in the twin beams will allow us to demonstrate a parallel quantum plasmonic sensing, as presented in chapter 6. Next, in this chapter we present the experimental setup for generating squeezed light to probe a plasmonic sensor. The experimental parameters for the FWM used for the experiments presented in this chapter are optimized to obtain the maximum temporal squeezing between the twin beams. Finally, we present and discuss the results by

demonstrating a quantum enhancement in the absolute sensitivity of our plasmonic sensor.

5.1 Does EOT Preserve Entanglement?

Acknowledgement

The material presented in this section is published in [72]. The dissertation author is the second author of this study.

To ensure that the plasmonic sensors we are using are compatible with quantum states of light, we design an experiment to verify that they maintain the quantum properties of the twin beam, such as the spatial information in entangled images and the temporal quantum entanglement. These tests represent the first steps towards implementing a quantum-enhanced plasmonic sensing configuration. They involve measuring the quantum entanglement before and after the plasmonic sensors.

5.1.1 Entangled Images and Plasmonic Nanoholes

We first check the compatibility of plasmonic sensors with the spatial information present in the twin beams by qualitatively comparing the spatial patterns on the twin beams before and after passing through two plasmonic sensors. Such a classical measurement allows us to determine if plasmonic sensors can preserve the spatial information of the

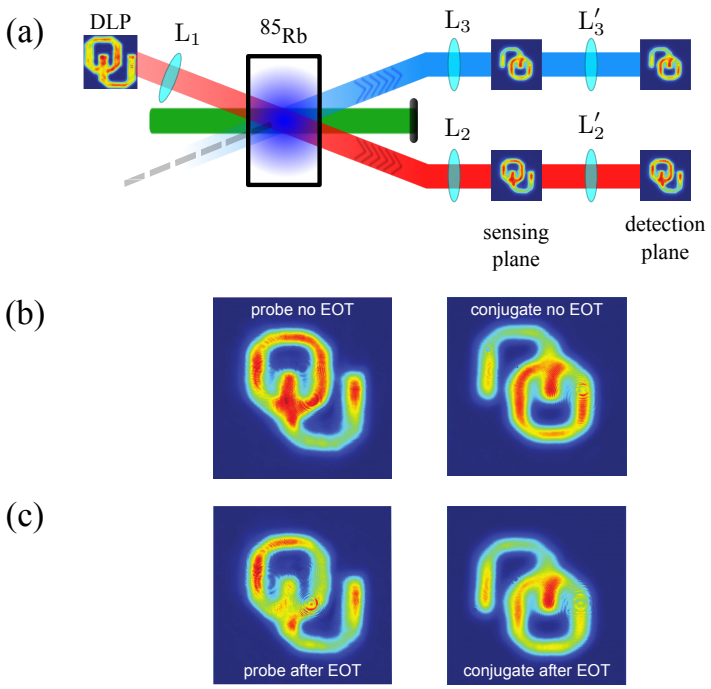

Figure 5.1: (a) By using a DLP, we generate spatial patterns on the seeding probe (red) beam to generate entangled images from the FWM. Lens system L_1 places the Fourier transform on the input image at the center of the Rb cell. Lens systems L_2 and L_3 perform an inverse Fourier transform of the center of the Rb cell to the sensing plane where plasmonic sensors are placed. Imaging lens systems L_2' and L_3' transfer the images from the plasmonic sensors to the detection plane. (b) Entangled images after the FWM at the sensing plane. (c) Entangled images on the detection plane after transduction through the two plasmonic sensors.

twin beams, which allows applications such as parallel plasmonic sensing with twin beams.

The experimental setup to generate the entangled images is presented in Fig. 5.1(a). To generate entangled images with arbitrary spatial patterns on the twin beams, the input probe beam is sent to a digital light processor (DLP) to modify its spatial profile before the Rb cell. An imaging system is used such that the probe beam has a flat wavefront at the plane of the DLP. The DLP (DLP3000-C300REF, Texas Instruments) is a 608×684 array of micro-mirrors that can be programmed through its computer interface to generate an arbitrary binary image on the input probe. The light reflected from the DLP passes through a 4-f lens system with a 500 μm pinhole at its Fourier plane to filter the high spatial frequencies of this image. These high k-vector components are outside the spatial gain bandwidth of the FWM and only introduce uncorrelated light. The image of the DLP after the 4-f system is then converted to its Fourier plane at the center of the Rb cell using a single lens, as shown by L_1 in Fig. 5.1(a), to seed the FWM process. The twin beams after the Rb cell pass through separate lens systems for each beam, as shown by L_2 and L_3 in Fig. 5.1(a), to form the bright twin images with the pattern introduced by the DLP at the Fourier plane after the Rb cell. These images form copies of the seeding image on the probe beam, as explained in chapter 2.

Using the pattern of the logo of the University of Oklahoma ("OU") on the DLP as the input image on the seeding probe beam, a pair of entangled images are generated. The conjugate image is inverted due to momentum conservation, as described in section 2.4. Two separate and independent plasmonic sensors are placed in the path

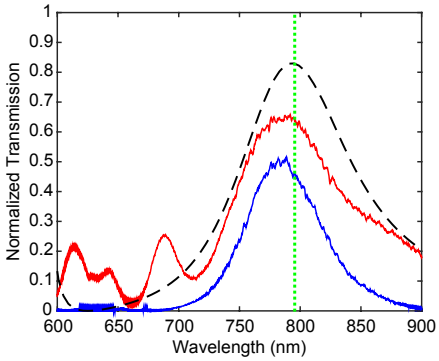

Figure 5.2: EOT spectra for the plasmonic sensors placed in the path of the probe (blue trace) and conjugate (red) beam. COMSOL simulation of the triangular nanohole array is shown with a dashed black trace. Green dotted line indicates our operating wavelength of $\lambda = 795$ nm.

of the entangled images on the plane labeled as "sensing plane" in Fig. 5.1(a). The sensing planes are therefore effectively at the Fourier plane of the Rb cell (far-field).

The entangled images before the plasmonic sensors, shown in Fig 5.1(b), transduce through the two independent and spatially separated plasmonic sensors and are then imaged on a beam profiler. Both plasmonic structures used in this experiment consist of a triangular nanohole arrays in a 100 nm thick silver film. The base size of the triangles is $\sim$ 220 nm and their height is $\sim$ 265 nm, with a periodicity of 400 nm along the horizontal and vertical directions. The transmission spectra of these two nanohole arrays, obtained with the white light spectroscopy described in section 4.2.3, and are shown in Fig. 5.2. Both samples have a transmission peak near $\sim$ 800 nm, which provides a non-zero transmission slope at the wavelength of our twin beams. The intensity transmissions of the samples in the conjugate and probe path are $\sim$ 65%

and ~ 50 %, respectively.

The entangled images generated from the FWM are shown in Fig 5.1(b). Due to the limited spatial bandwidth of the FWM process, as described in section 2.4, the entangled images are not as sharp as the input image on the seeding probe beam. The entangled images after the transduction through the EOT plasmonic structures are shown in Fig 5.1(c). Comparing the entangled images before and after EOT, we can see that the resolution of the output images with respect to the input ones are mainly preserved. This indicates that EOT through the plasmonic structures preserves the spatial information of the incoming optical field. Overall, these images demonstrate clearly the spatial multi-mode nature of twin beams and the plasmonic-mediated EOT process.

Additionally, it is worth noting that the resolution of the entangled images is high enough to resolve spatial patterns of the seeded input OU logo, which indicates that the size of the coherence areas in the twin beam is smaller than the smallest feature of the input seeding image. This point becomes important for spatially resolved sensing application, as will be described in chapter 6.

5.1.2 Temporal Entanglement and Plasmonic Nanoholes

In the previous section we present a classical measurement to qualitatively verify that the spatial information in the twin beam is preserved by the plasmonic sensors. In this section we characterize the quantum entanglement of the twin beams before and after transduction through the plasmon-mediated EOT process in nanohole structures. As

defined in section 2.3.6, the inseparability parameter $\mathcal{I}$ provides a direct measure of the degree of quantum entanglement in the twin beams and can be measured using a double balanced HD system: one HD for the probe and another one for the conjugate. Moreover, to ensure temporal quantum entanglement in a particular spatial mode of the twin beams, we pattern the LOs of the two HDs with a non-Gaussian structure, the "OU" logo, using the DLP, as explained in the previous section. The spatial profile of LOs effectively selects out the spatial pattern of twin beams being measured.

The experimental setup to measure the inseparability parameter before and after the plasmonic sensors is given in Fig. 5.3. To generate the required LOs, we duplicate the FWM process: two spatially separated FWM processes occur simultaneously inside the same vapor cell. We split the probe (before the DLP) and the pump beams just before the Rb cell. That means that two pairs of pump-probe beams enter the cell to start two identical FWM processes and generate two pairs of twin beams. One probe beam generates the two LOs (probe and conjugate) while the second probe beam is used to generate the signal twin beam for the two HDs. Therefore, the LOs are automatically matched to the entangled images that are being characterized as signals on the HDs. Since the LO should be more intense than the signal, we block the signal seeding probe beam to let it grow from a spontaneous FWM. On the other hand, the LO seeding probe generates bright twin beams which grow from a stimulated FWM.

After the vapor cell, the signal twin beams are imaged on the two plasmonic structures that we introduced in Fig. 5.2, while the LO twin beams pass through the boro-silicate glass substrate. With this setup, the measurement apparatus for the LO

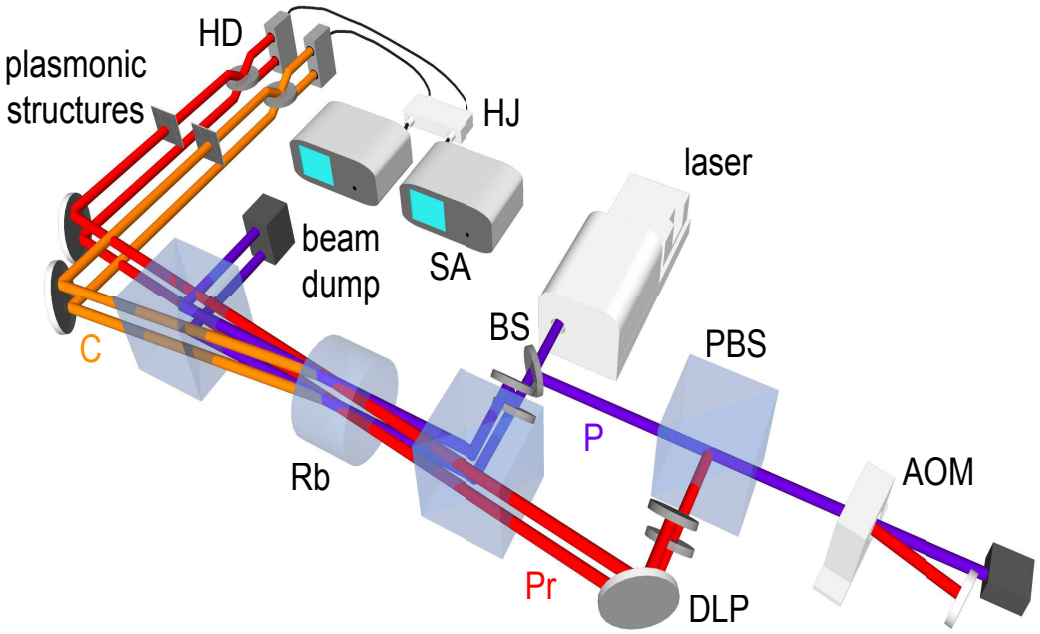

Figure 5.3: Experimental setup to characterize quantum entanglement between the twin beams before and after transduction through the plasmonic structures. By duplicating the FWM process, we generate the two LOs for performing two balanced HDs. Figure reproduced from [72].

and signal twin beams undergo almost the same optical paths to provide a better mode-matching between the signals and the LOs of the entangled images.

The initial alignment of the HDs for each mode is performed with bright entangled images for the signal to optimize the mode-matching efficiency of the HDs. The mode-matching quantifies how similar the spatial profile of the LO is compared to the spatial mode of the signal, and is calculated from the fringe contrast of the interference between the LO and the signal. Assuming the LO and the signal have equal power,the mode-matching efficiency is given by:

$$\text{Mode-Matching} = \frac{I_{\max} - I_{\min}}{I_{\max} + I_{\min}} = \frac{I_{\text{amp}}}{I_{\text{avg}}}, \tag{5.1}$$

where I is the DC output of each HD, and the minimum, maximum, amplitude, and average subscripts are defined in Fig. 5.4. We scan the phase of the LO using a small mirror epoxied to a piezoelectric transducer (PZT). As we drive the piezo with a triangular function, the interference of the LO and bright signal beam can be measured on an oscilloscope synchronized with the function generator driving the piezo-mounted mirror. For an ideal interference, complete spatial overlap between the LO and the signal modes leads to a mode-matching of 100%.

For our experiment, we obtain a mode-matching of 97% when the entangled images pass through the glass substrate, and 94% when they pass through the EOT plasmonic structures. The fact that the mode-matching does not significantly change with and without plasmonic structure gives another indication that the photon-plasmon-photon conversion in the EOT is a coherent process that preserves the spatial information of

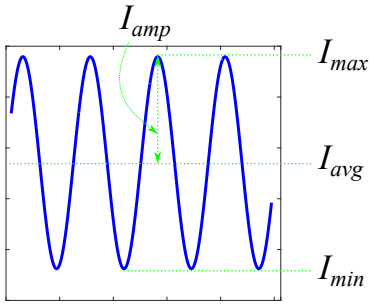

Figure 5.4: Contrast fringes of the HD as we scan the phase of the LO.

the incoming optical fields.

After the initial alignment optimization, the input probe beam for the signal twin beams is blocked and the process grows from the spontaneous emission, generating a VTMSS. The spatial profile of the LOs, which are bright and patterned with the "OU" logo, selects the spatial profile of the signal vacuum twin beams on the two HDs. Figure 5.5(b) shows the spatial profile of the LOs used for the probe and conjugate HDs.

The sum and difference signals to obtain the joint quadratures of the twin beams are generated by adding and subtracting the signals from the two HDs using a HJ. These signals are then analyzed on a SA. By scanning the phase of both LOs in a synchronous way, we directly measure the joint quadratures needed for the inseparability parameter. Figures 5.5(a) and (c) show the results of our measurements on the effect of the plasmonic structures on the quadrature squeezing for "OU" entangled images. The blue (red) traces show the noise of the sum (difference) signals normalized to the SNL as the phase of the LOs are scanned linearly in time, before, Fig. 5.5(a), and after, Fig. 5.5(c), the vacuum twin beams undergo EOT through the plasmonic structures.

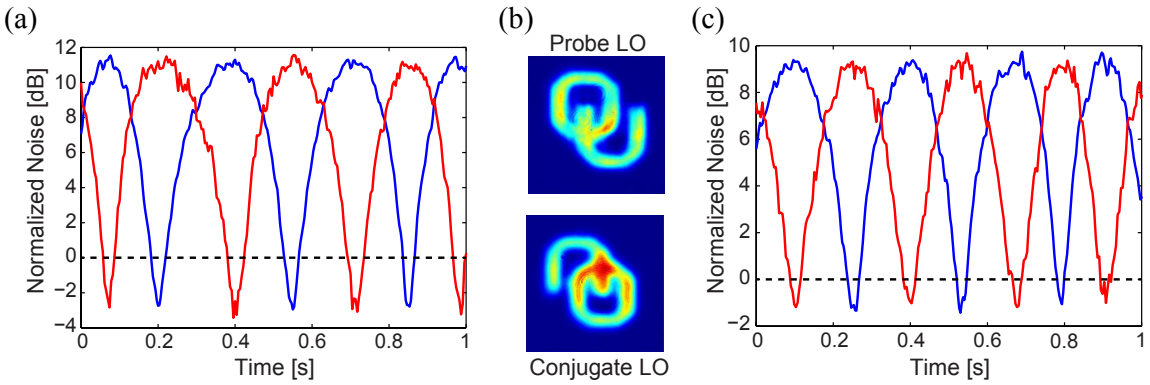

Figure 5.5: The difference and sum signal from the two HDs as we scan the phases of the LOs together. (a) Normalized noise of the joint quadratures without passing through EOT. (b) Spatial modes of the twin beams LOs. (c) Normalized noise of the joint quadratures after passing through EOT. Figure reproduced from [72]

When the phase of the LOs is set to measure the amplitude quadratures, the minimum of the red trace corresponds to the amplitude difference quadrature $\langle \Delta^2 \hat{X}_- \rangle$ and shows squeezing, while at the same time the blue trace corresponds to the amplitude sum quadrature $\langle \Delta^2 \hat{X}_+ \rangle$ and shows excess noise. When the phase of the LOs is set to the phase quadratures, the minimum of the blue trace corresponding to the phase sum $\langle \Delta^2 \hat{Y}_+ \rangle$ shows squeezing, while the red trace for the phase difference $\langle \Delta^2 \hat{Y}_- \rangle$ shows excess noise. Therefore, as expected for the twin beams, the amplitude difference and phase sum quadratures are squeezed. The traces plotted in Fig. 5.5 are normalized to the SNL shown by dashed lines at zero.

The noise of both joint quadratures is below the SNL before and after the transduction process, indicating that entanglement is preserved after undergoing the photon-

Parameter	Value
FWM Gain	4
Pump Size (diameter)	3 mm
Pump Power	≈ 700 mW
Cell Temperature	115° C
PZT Amplitude	200 mV
PZT Freq.	500 mHz
Probes Mode-Matching after EOT	94%
Conjugates Mode-Matching after EOT	93%

Table 5.1: Relevant parameters for generating squeezed states and measuring entanglement with two balanced HDs.

plasmon-photon conversion of the EOT. In particular, before the plasmonic structures, both joint quadratures have a noise of 2.8 ± 0.2 dB below the SNL, which corresponds to $\mathcal{I} = 1.05$. After EOT, the noise of the joint quadratures is 1.1 ± 0.2 dB below the SNL, corresponding to $\mathcal{I} = 1.55$.

The reduction in entanglement after EOT is consistent with the reduction that is expected from the losses introduced by the plasmonic structures. As described in section 2.3, using a BS model for losses, we predict -1.15 dB of squeezing after taking the losses due to the plasmonic structures and the slight degradation in HD mode-matching into account. For the configuration used in this experiment, the initial squeezing of the entangled images by an ID measurement was -3.5 ± 0.2 dB. The

Parameter	Value
Resolution Bandwidth (RBW)	30 kHz
Video Bandwidth (VBW)	100 Hz
Frequency	1 MHz
Span	100 Hz
Attenuation	0 dB
Preamp	ON

Table 5.2: Relevant SA parameters used in the experiment.

reduction of squeezing level when measuring the quadrature squeezing without the plasmonic structures is most likely due to the imperfect mode-matching and alignment between the LOs and the twin beams. The FWM parameters used in this experiment are listed in table 5.1 and the settings of the SA are listed in table 5.2.

These results show that entanglement in the twin beams is preserved by EOT through the plasmonic structures. Therefore, we can conclude that the EOT process is compatible with quantum entanglement and can maintain the quantum properties of the twin beams [69, 106, 107, 145]. These results provide the first steps towards a quantum plasmonic network and pointing to a mechanism for parallel quantum plasmonic information processing [24, 144].

5.2 Experiment: Quantum-Enhanced Plasmonic Sensing

Acknowledgement

The material in this section is published in [73]. The dissertation author is the first author of this publication.

Knowing that plasmonic sensors are compatible with squeezed light, we use them as the sensing device as described in chapter 3. In this section, we construct our quantum sensing configuration by probing a plasmonic sensor with twin beams and performing an ID measurement to detect modulations in the refractive index of air below the SNL.

5.2.1 Experimental Apparatus

The experimental setup for quantum plasmonic sensing is shown in Fig. 5.6. The twin beams are generated from a FWM process in ^{85}Rb atoms, as explained in section 2.2.2. The probe from the twin beams is used for probing the plasmonic sensor to detect changes in the refractive index of the air surrounding it. The probe beam, after undergoing EOT through the plasmonic sensor is measured with a photodetector. The conjugate beam of the twin beams acts as the reference and is directly sent to its designated photodetector. A variable electronic attenuator (see section 2.3.3) on the conjugate detector is used to minimize the measured noise between the twin beams in an ID measurement. The difference signal is then analyzed on an electronic SA to

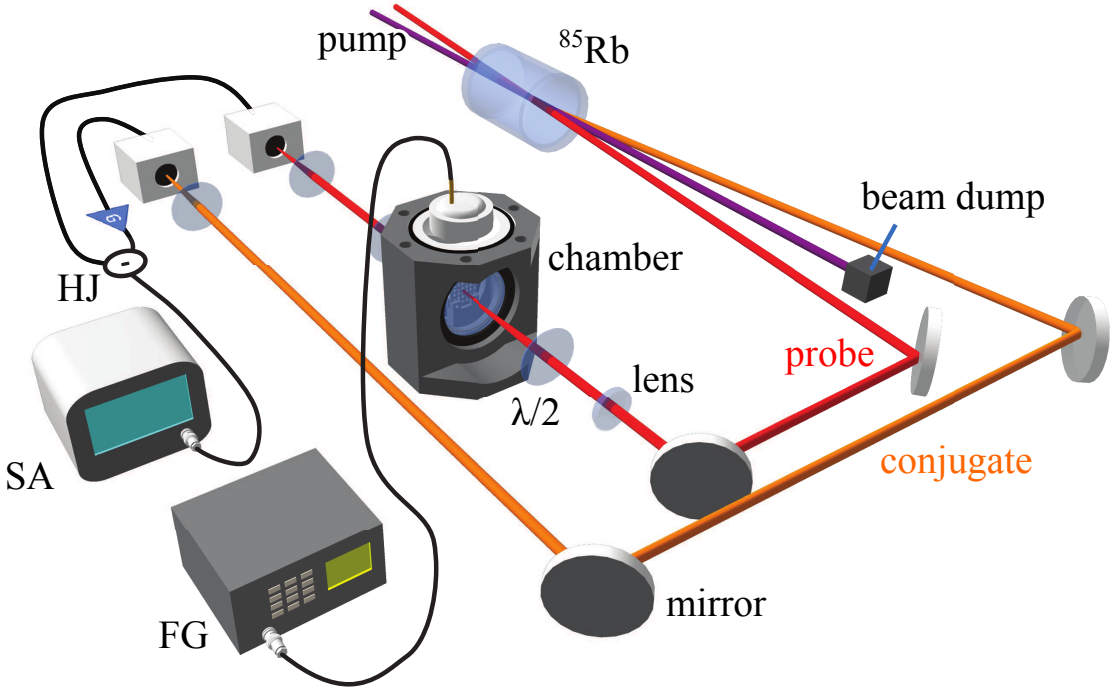

Figure 5.6: Experimental implementation of quantum plasmonic sensing. SA: spectrum analyzer, FG: function generator, HJ: hybrid junction. Figure reproduced from [73]

characterize the SNR.

The parameter space for the FWM was scanned to obtain the maximum gain from the process and consequently the best squeezing possible in the temporal degree of freedom. Table 5.3 summarizes the optimized parameters for the FWM used in this experiment. Since all the probe photons of the twin beams are focused on a single plasmonic sensor, our sensing configuration is not sensitive to the spatial correlations. The spatial modes of the twin beams become important in chapter 6 for the implementation of parallel quantum plasmonic sensing.

Parameter	**Value**
Δ (one-photon detuning)	800 MHz
δ (two-photon detuning)	4 MHz
Pump waist diameter	1 mm
Pump power	600 mW
Probe waist diameter	0.7 mm
Probe power (seeding)	70 μW
Rb cell size	1 inch (diameter), 12 mm (length)
Pump–probe angle	0.5°
Rb vapor cell temperature	109°C

Table 5.3: FWM parameters leading to optimum squeezing for the quantum plasmonic sensing experiment.

The plasmonic sensor that we use in this experiment has an overall size of 200 μm $\times$ 200 μm. These sensors were introduced in chapter 4 and the characteristic transmission spectrum and the SEM images for the particular sensor used for this experiment are shown in Fig. 4.4. The plasmonic sensor shows an EOT transmission of $\sim$66% at the probing wavelength of 795 nm. A layer of PMMA is deposited on top of the nanohole array to protect the sample from oxidizing. We have verified that this layer of PMMA does not significantly affect the functionality or the sensitivity of the sensor for the ultrasound-based measurements described here.

The probe beam is focused to a waist diameter $\approx$ 20 μm into the plasmonic structure to avoid beam diffraction and leakage from the edges of the sensor. Moreover, since the plasmonic response is polarization dependent, we use a $\lambda/2$ wave-plate before the sensor, as shown in Fig. 5.6, to align the polarization of the input light with the base of the triangles.

5.2.2 Signal Generation: Chamber

We study the response of the plasmonic sensor to modulations in the refractive index of air induced with an ultrasound buzzer, which is a piezoelectric material used to generate pressure waves when driven with a modulation voltage. Because the index of refraction depends on the pressure of air [146], such modulations lead to modulations in the index of refraction of air around the plasmonic sensor. Moreover, the ultrasound buzzer allows us to introduce modulations at high frequency, which makes it possible to perform the measurements away from the low frequency technical noise.

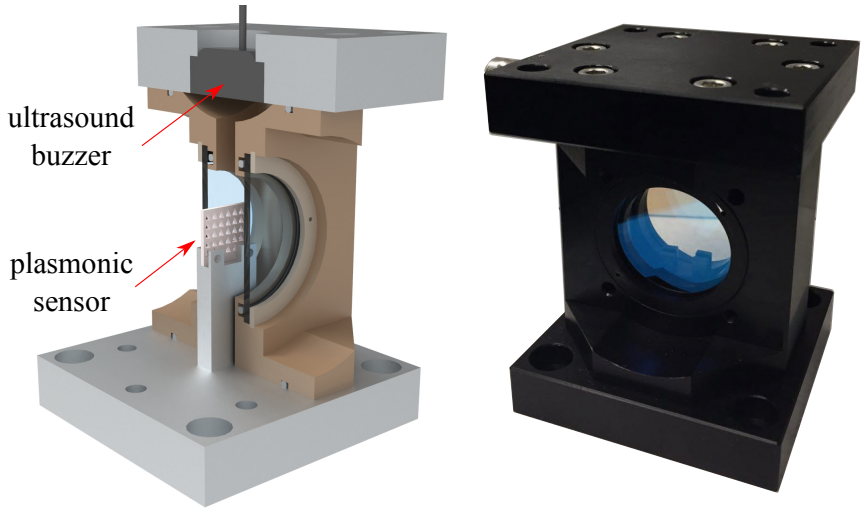

Figure 5.7: Cross-sectional cut (left) of the chamber (right) built to hold the plasmonic sensor and ultrasound buzzer in a controlled environment.

To provide a well-controlled and stable modulation of the refractive index, a hermetically sealed chamber was designed and built to enclose the plasmonic sensor and the buzzer, as shown in Fig. 5.7. Such a design minimizes the undesired effects of air currents or humidity changes during the data acquisition time, resulting in a controlled environment. Moreover, the home-built chamber can be filled with liquids in case modulations in such environments need to be studied.

5.2.3 Chamber Calibration

The magnitude of the pressure waves generated by the ultrasound buzzer depends on the amplitude of the driving voltage applied in the buzzer. However, due to the formation of ultrasound standing waves inside the chamber, the amplitude of the ultrasounds depends on the frequency of the modulations and the geometry and the volume of the

chamber. Therefore, each point inside the chamber has a different modulation amplitude of the refractive index. To have a measure of the absolute changes in refractive index for each voltage driving the buzzer, we calibrate the chamber via a Mach-Zehnder interferometer, as shown in Fig. 5.8. Moreover, to ensure we are calibrating the refractive index modulation at the location of the plasmonic sensor, we keep the location of the plasmonic sensor fixed with respect to the probe beam.

The interferometer reads the modulations in phase ($\Delta\phi$) due to the refractive index modulations (Δn):

$$\Delta\phi = \frac{2\pi L}{\lambda}\Delta n, \tag{5.2}$$

where λ is the wavelength of the light (795 nm), and L is the length of the chamber over which the phase change is introduced. Using a 50/50 BS before the chamber, we use half of the beam to probe the chamber and the other half serves as the reference beam. These two beams are overlapped to interfere on the second BS to produce the difference signal at the output of the HJ that subtracts the photocurrents from the photodetectors at the outputs of both ports of the interferometer. This way, phase modulations lead to amplitude modulations through the interference signal on the output of the interferometer.

We scan the phase of the reference arm with a mirror driven by a PZT, which toggles the output signal of the interferometer between a complete constructive and destructive interference. As we scan the phase of the interferometer by driving the PZT with a sine function, a sinusoidal signal appears on the low frequency (DC) output of the interferometer, similar to the interference pattern shown in Fig. 5.4. By using a

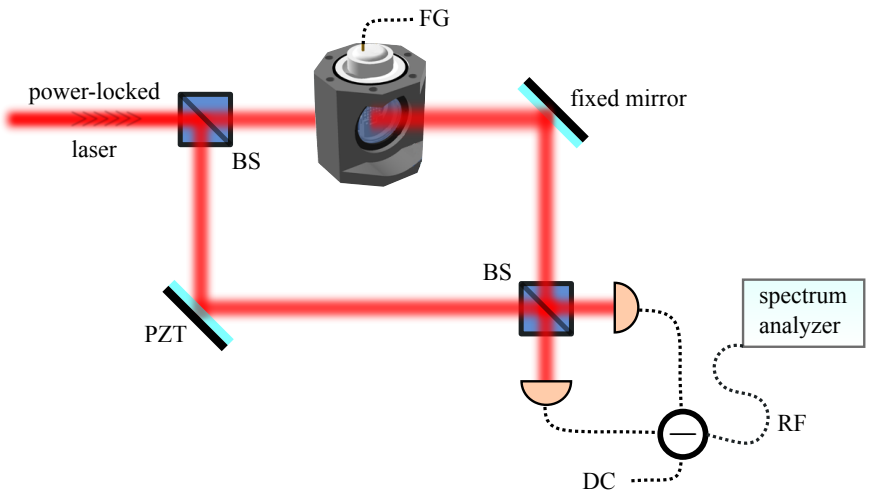

Figure 5.8: Mach-Zehnder interferometer for calibrating the refractive index modulation as a function of the voltage applied to the ultrasound buzzer inside the chamber. FG: function generator, PZT: piezo electric, BS: balanced (50/50) beam splitter.

bias-tee (with a cutoff frequency of 100 kHz) at the output of the HJ, we can split the DC and the high frequency (RF) components of the interference signal. As we scan the phase of the interferometer, the interference fringes are scanned and we can calculate the contrast of the interferometer as $V = A \sin(\Delta\phi)$, where A represents the amplitude of the peak-to-peak signal.

The DC port is also used to lock the interferometer to its most sensitive operating point. The most sensitive point to operate the interferometer is where we have the sharpest slope for the interference signal, corresponding to the point where I_{avg} becomes zero in Fig. 5.4. This is when the signals from the two outputs are completely identical and cancel each other. Therefore, we lock the phase of the interferometer using the proportional-integral-derivative (PID) locking setup at this point.

After locking the interferometer to its zero crossing phase, we can calibrate the amplitude of the phase modulations introduced by the ultrasound buzzer. Since their frequency is faster than the PID response, they are not attenuated by the locking setup. Moreover, we monitor these modulations using the RF portion of the bias-tee, independent from the DC portion which was used for the locking setup. Therefore, the modulation signal appears on the RF portion and can be analyzed with the SA. We generate the modulations in the refractive index of air by driving an ultrasound buzzer with a sinusoidal function at its resonant frequency of 199 kHz.

With small driving voltages of the buzzer that generates the modulation signals when locked around the most sensitive point, changes in phase are linearly related to the changes in the amplitude of the interference signal. Using the proportionality

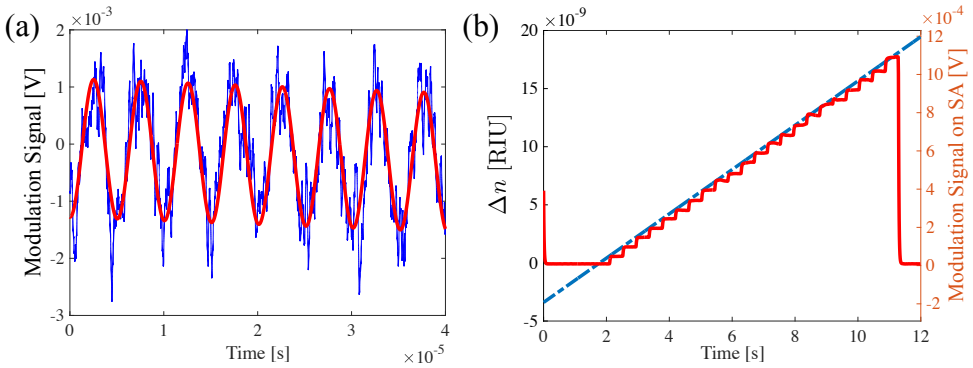

Figure 5.9: (a) Modulation signal on the oscilloscope from the locked interferometer as we drive the ultrasound buzzer. (b) Calibration results: left vertical axis is Δn and the right vertical axis is the magnitude of the modulation signal on the SA. Dashed blue trace is the linear fit to the measured data (red trace). The horizontal axis is time, which is proportional to the driving voltage of the buzzer.

relation, we have:

$$\frac{\Delta\phi}{\pi} = \frac{B}{A} \Longrightarrow \Delta\phi = \frac{\pi B}{A}, \tag{5.3}$$

where B is the amplitude of the ultrasound modulations around the zero-crossing point of the interferometer, as shown in Fig. 5.9(a).

Using Eq. (5.2), the average change in the refractive index (Δn) along the effective propagation length of the chamber (L) can be extracted from the amplitude of the modulation signal according to:

$$\Delta n = \frac{\lambda B}{2AL}. \tag{5.4}$$

The amplitude of the modulation signal depends on the driving voltage of the transducer: higher driving voltages of the ultrasonic buzzer generate stronger ultrasonic pressure waves, which lead to larger refractive index modulations. Additionally, the magnitude of the refractive index modulations generated by the ultrasound buzzer is proportional to the size of the driving voltage V_d of the buzzer:

$$\Delta n \propto V_d. \tag{5.5}$$

Therefore, we can measure the amplitude of the modulation signal at different driving voltages of the buzzer V_d, as shown in Fig. 5.9(b). By fitting a line to the data, we can directly find the corresponding change in refractive index at each driving voltage of the buzzer, that is, Δn to V_d relation of the form:

$$\Delta n = \left(1.651 \times 10^{-5} \frac{[RIU]}{[V]}\right) \cdot V_d, \tag{5.6}$$

where we used the measured values of $B = 272$ mV, $A = 3.3$ V, and $L = 6.35$ mm for our calculation. In this analysis, the horizontal intercept of the linear fit in Fig. 5.9(b)

is bound to zero, due to the fact that when there is no driving voltage, no modulation exists.

5.3 Experimental Results

After calibrating the ultrasounds inside the chamber, we can probe a plasmonic sensor with twin beams to detect these modulations in the refractive index of air. When we drive the ultrasonic transducer at its resonant frequency (199 kHz), if the size of this modulation signal is large enough, we can see the modulation on top of the noise in the ID measurement output.

The minimum amplitude of the modulation in the refractive index that the plasmonic sensor can detect depends on the response of the sensor (defined by the slope of the transmission transfer function of the sensor), the magnitude of the ultrasound standing waves, and the optical power and noise properties of the light probing the sensor. Placing a given plasmonic sensor at a fixed location and with a fixed optical power, a constant driving voltage of the buzzer (V_d) generates a stable modulation signal. As described for the calibration process, the magnitude of the modulation in transmission through the plasmonic sensor is linearly proportional to the modulation in refractive index, which itself depends on the driving voltage of the buzzer.

The noise of the measurement, on the other hand, depends on the properties of the probing light: for a classical state, the noise is at or above the SNL, while for the twin beams it can be reduced below the SNL due to their quantum correlations. The initial

ID squeezing between the twin beam was -9 dB which was degraded to -4 dB (60% below the SNL) after 66% intensity transmission through the plasmonic sensor and with -3.5 dB optimized EA.

For the classical counterpart of our quantum plasmonic sensing configuration, we replace the twin beams with two coherent states (two laser beams which do not undergo a nonlinear amplification). One laser beam with the same power as the probe beam probes the sensor, while another beam of the same power as the conjugate beam serves as the reference beam, leading to the measurement at the SNL with two beams. Moreover, to keep the number of photons probing the sensor fixed as our resource, we lock the optical power in the probe beam at 70 μW with the AOM that generates the frequency red-shift of the probe beam (not shown in Fig. 5.6). This amount of optical power is set by the saturation limit of the photo-detectors.

5.3.1 Discrete Signals

First, we apply a modulation signal with a constant discrete driving voltage. Figure 5.10 shows the measured power spectrum normalized to the SNL. In this figure the SA is swept over a 2 kHz span centered around 199 kHz. For a large driving voltage, corresponding to $\Delta n = 1.6 \times 10^{-7}$ RIU, the modulation signal at 199 kHz is large enough to be resolved using both coherent states (blue trace) and twin beams (red trace). By using the twin beams, we obtain an enhancement in the SNR due to the remaining -4 dB of squeezing. Such a quantum enhancement allows us to resolve smaller modulation amplitudes with our twin beam than with coherent states, as can be seen in Fig. 5.10(b). In this case, a

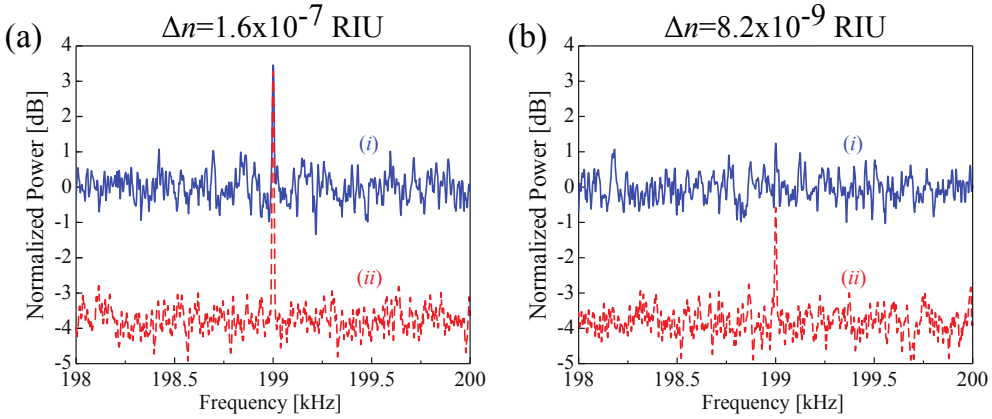

Figure 5.10: Modulation signal in transmission from the plasmonic sensor from modulations in the refractive index of air measured with a SA. (a) Signals due to large changes in the refractive index can be resolved with both the coherent states and the twin beams while smaller signals. (b) As the magnitude of the modulation signal reduces, only twin beams can resolve it. SA settings: RBW= 100 Hz, VBW= 10 Hz, with 50 times averaging. Figure reproduced from [73].

modulation signal corresponding to $\Delta n = 8.2 \times 10^{-9}$ RIU, can be distinguished from the noise only with the twin beams. This result explicitly shows the higher sensitivities that we can obtain with the implemented quantum-enhanced plasmonic sensors, enabling us to detect modulation signals beyond the SNL.

5.3.2 Ramping Signal and SNR

In addition to detecting the refractive index modulation signal below the SNL using a plasmonic sensor, we can measure the absolute sensitivity and quantify the quantum

enhancement, defined in chapter 3. To obtain these values, we linearly decrease the driving voltage of the ultrasonic buzzer using a down-ramping sawtooth function on the function generator. Moreover, the SA is set to analyze the signal at the modulation frequency (199 kHz) using its zero-span feature, while synchronized with the function generator driving the buzzer. Therefore, effectively, the SA is set to measure the power in the signal peak, shown in Fig. 5.10. The measured signals are shown in Fig. 5.11, using classical states (blue trace) and twin beams (red trace). Moreover, to find the noise of the measurement for each state, we let the SA free-run while the buzzer is not being driven. The noise level of such measurements is determined by the noise of the optical field used to probe the sensor, as shown in Fig. 5.11 with pale blue and pale red traces for the SNL and the twin beams, respectively.

The signal displayed on the SA (S_{SA}) is a quadrature addition of the noise (σ_{noise}) and the transmission modulation signal itself (S_{sig}):

$$S_{SA}^2 = \sigma_{noise}^2 + C_s \cdot S_{sig}^2, \tag{5.7}$$

where the scaling factor C_s is related to the averaging on the SA in log scale, as averaging the log of a signal is not the same as taking the log of the averaged signal. The scaling factor depends on the ratio of the RBW to the VBW of the SA and the number of times averaging over the traces [147], and becomes significant for signals close to the noise [60]. By setting the SA to power average the traces in linear scale, this correction factor would be internally taken into account.

As the amplitude of the driving voltage decreases, the magnitude of the modulation

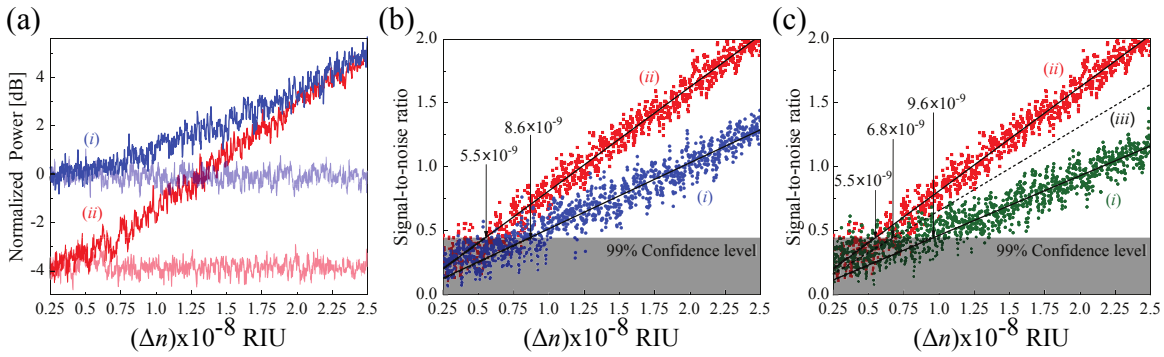

Figure 5.11: Quantum-enhanced sensing with the plasmonic sensor. (a) Zero-span at 199 kHz: Decreasing the amplitude of the ultrasound modulation, hence Δn, the signal reaches the noise at difference levels with (i) coherent states and (ii) twin beams. (b) Signal-to-noise ratio (SNR) vs. changes in the refractive index of air. The values shown indicate the smallest changes in refractive index where we can be 99% confident that what we are detecting is "not" noise. (c) Comparison between the SNR using a balanced classical configuration with two coherent states, trace (i), twin beams, trace (ii), and the optimal classical configuration with a single coherent state, trace (iii). SA settings: RBW = 10 Hz, VBW = 1 Hz, Averaging: 50 times. Figure reproduced from [73].

signal gets smaller to a level that cannot be clearly distinguished from the noise (pale traces). According to Eq. (5.7), the SNR in logarithmic scale is calculated as:

$$\text{SNR [dB]} = \text{Signal (mod. ON) [dBm]} - \text{Signal (mod. OFF) [dBm]} - \text{CF}, \tag{5.8}$$

where the correction factor CF is the same as the C_s in log scale, and varies with the calculated SNR. Since we are interested in the SNR values in linear scale, we convert the value obtained in Eq.(5.8) into linear scale: $\sqrt{10^{\text{SNR[dB]}/10}}$. The linear values of the SNR calculated as described above are shown in Figs. 5.11(b) and (c). As expected, the calculated SNR values have linear relations with respect to changes in refractive index.

According to the definition of the sensitivity in section 3.1, we are interested in the point where we cannot resolve the modulation signal from the noise. Since the noise of the twin beams is lower than the SNL, the noise starts to dominate the measurement at lower values of Δn with the twin beams than with coherent states. Here, we use the 99% confidence interval standard for sensitivity, which shows the $(\Delta n)_{\text{min}}$ at which the signal can be distinguished from the noise, with 99% confidence. Using a linear fit for the SNR and bounding its intercept to zero, which corresponds to the point when there is no signal, $(\Delta n)^{\text{CS}}_{\text{min}} = 8.6 \times 10^{-9}$ RIU when probing with coherent states and $(\Delta n)^{\text{TB}}_{\text{min}} = 5.5 \times 10^{-9}$ RIU when probing with twin beams, as shown in Fig. 5.11(b).

These results are obtained for particular values of the bandwidths for the measurement system used in our experiment. To make our results independent of the detection bandwidth, we normalize the absolute sensitivities to the resolution bandwidth (RBW) of the SA that we used in these measurement, i.e. 100 Hz. The RBW is the bandwidth

window for the detected power on the SA. Since we are interested in the SNR as the ratio of the signal to the noise in volts, we take the square root of the RBW. Therefore, taking the bandwidth of the measurement system into account, the sensitivities become 8.6×10^{-10} RIU/$\sqrt{\text{Hz}}$ and 5.5×10^{-10} RIU/$\sqrt{\text{Hz}}$ when probing with coherent states and twin beams, respectively.

5.3.3 Quantum Enhancement

As explained in section 3.5, the ratio between the sensitivities obtained with twin beams to the one at the SNL provides the QEF. This ratio quantifies the enhancement we can achieve by using the quantum entangled states of light. Therefore, we can measure the QEF by taking the ratio of the minimum resolvable change in refractive index obtained with the coherent states to the one with the twin beams, as defined in section 3.5. Since the plasmonic sensor used to measure the changes in air refractive index is the same with both states of light, the contribution to the sensitivity due to the characteristic response of the plasmonic sensor cancels as a common factor. Therefore, for a given sensor, and with a fixed optical power, the QEF depends only on the amount of noise reduction in twin beams:

$$\text{QEF} = \sqrt{\frac{(\Delta^2 \hat{M}_-)^{\text{CS}}_{\text{min}}}{(\Delta^2 \hat{M}_-)^{\text{TB}}_{\text{min}}}} = \sqrt{\frac{1}{R_{\text{lin}}}}, \tag{5.9}$$

where $\hat{M}_-$ is the ID measurement signal, and R_{lin} is the level of squeezing measured in linear scale, as introduced in Eq. (2.38).

Using the initial -9 dB squeezing right after the ^{85}Rb vapor cell, the QEF corresponds

to 2.82. This means that we would expect to be able to detect changes in the refractive index of air as small as $(\Delta n)^{\mathrm{TB}}_{\mathrm{min}} = 3 \times 10^{-10}$ RIU$/\sqrt{Hz}$, using the same optical powers and plasmonic sensor. Due to all the optical losses in the measurement, such as the optical loss from the optical elements in path as well as the 66% EOT from the plasmonic sensor, the measured squeezing with our twin beam is limited to -4 dB, corresponding to a QEF of 1.58.

By comparing the absolute sensitivity using coherent states and twin beams, we can directly measure the QEF from the experimental results. According to the values shown in Fig. 5.11, the ratio between these two sensitivities: $(\Delta n)^{\mathrm{CS}}_{\mathrm{min}}/(\Delta n)^{\mathrm{TB}}_{\mathrm{min}} = \frac{8.6\times10^{-10}\ \mathrm{RIU}/\sqrt{\mathrm{Hz}}}{5.5\times10^{-10}\ \mathrm{RIU}/\sqrt{\mathrm{Hz}}} = 1.54$, which is consistent with the expected QEF from the remaining -4 dB of squeezing.

5.3.4 Optimal Classical Measurement with a Single Beam

When measuring with a pure coherent state, the optimum measurement corresponds to using only one coherent state probing the sample. This can be seen in the noise calculations for the ID measurement in Eq. (2.44), where the SNL gets minimized when the EA is set to zero, $G = 0$. This explicitly shows that when we have no quantum correlations in the reference beam, the addition of the second beam only increases the noise as their fluctuations are uncorrelated and add up in quadrature. Therefore, instead of comparing with the classical counterpart of our quantum sensing configuration, it is interesting to compare the sensitivity with the optimum classical measurement setup with only one coherent state probing the sensor. Our resource needs to be kept the

same; that is, the number of photons reaching the plasmonic sensor needs to be kept equal to those in the probe beam (from the twin beams) before the sensor.

As mentioned before, since it is practically hard to have a pure coherent state, to reach the SNL it is necessary to eliminate all the technical noise from a beam of light through an ID measurement. Therefore, to estimate the noise of the single-beam measurement at the SNL, we perform a balanced measurement with two coherent states, each with equal power to that of the probe from the twin beams. The result of such measurement is shown in Fig. 5.11(c) in green, trace (i), and results in $(\Delta n)^{\mathrm{2CS}}_{\mathrm{min}} = 9.6 \times 10^{-10}$ RIU/$\sqrt{\mathrm{Hz}}$. Since the noise of the ID signal is equal to the sum of the noise in both beams, which is twice the noise of the single beam probing the sensor, we estimate the sensitivity of a single coherent state by dividing the noise in half, or in logarithmic scale, subtract 3 dB from the SNR of the ID measurement with two coherent states. This calculation leads to the dashed line, trace (iii), in Fig. 5.11(c), which provides an estimation of the sensitivity of a measurement with a single coherent state to be $(\Delta n)^{\mathrm{1CS}}_{\mathrm{min}} = 6.8 \times 10^{-10}$ RIU/$\sqrt{\mathrm{Hz}}$, with the same power as the probe beam from the twin beams. Even compared to the optimal classical measurement with a single-beam coherent state configuration, we obtain a QEF $= \frac{6.8\times10^{-10}\ \mathrm{RIU}/\sqrt{\mathrm{Hz}}}{5.5\times10^{-10}\ \mathrm{RIU}/\sqrt{\mathrm{Hz}}} \approx 1.24$, corresponding to a $\sim 24\%$ quantum enhancement in sensitivity.

5.4 Conclusion

In this chapter we demonstrated an experimental implementation of quantum-enhanced plasmonic sensing to directly detect modulations in the refractive index of air beyond the SNL. Although this measurement detects modulations in the refractive index at 199 kHz, the results can be extended to other sensing applications and at other frequencies. Plasmonic sensors are typically used to detect slow varying changes in refractive index. Such measurements can be performed by monitoring the transmission change at DC frequencies, where technical noise dominates. Technically, it is hard to generate squeezed light at such low frequencies [148, 149]. However, it is possible to extend the presented quantum sensing configuration to the regime where the changes in the refractive index are at low frequencies and benefit from the same quantum enhancements.

Although this experiment is not the first of its kind, our experiment is nearly five orders of magnitude more sensitive compared to previous proof-of-principle quantum-enhanced plasmonic sensing [75, 105, 109, 143]. For example, the smallest detectable change of refractive index using quantum resources in Ref. [75] is reported to be 0.001 RIU with a 1 kHz bandwidth, which leads to $\sim 3 \times 10^{-5}$ RIU/$\sqrt{\text{Hz}}$. Moreover, the sensitivity of our quantum plasmonic sensing configuration is comparable to the classical state-of-the-art ultrasound sensing with plasmonic sensors [29], where the optical power is reported as 14-times higher than the optical power of the probe beam in our experiment. Using such high powers can cause thermo-plasmonic effects and damage

the plasmonic sensor, the target sample to be detected, or even the photodetectors.

The achievable QEF is mainly limited by the losses after the source, which can degrade the initial quantum correlation and the measured level of squeezing between the twin beams. In our experimental setup, the major sources of optical loss include the imperfect EOT process through the plasmonic sensor (∼34% loss) and the optical losses introduced by optical elements (∼27% loss). The loss from the plasmonic sensors is not fundamental and can be minimized significantly by optimizing their design and fabrication process. Near-ideal plasmonic structures approaching 100% EOT response can be expected [150, 151]. However, as mentioned in chapter 3, resonance sensors are not sensitive to changes in transmission at the peak of their resonance and therefore introducing some losses is inevitable. By eliminating the losses in the system, or redesigning the measurement to estimate using phase, for instance, would allow us to take better advantage of the initial available quantum correlations. Under such ideal conditions, we would expect a QEF of 182% with the initial -9 dB squeezing in our twin beams.

These results can be extended to other compatible measurement configurations, opening new possibilities for real-life applications, such as high precision biomedical and biochemical detection schemes.

Chapter 6

Parallel Quantum Plasmonic Sensing

Acknowledgement

The content of this chapter is under preparation for publication. The dissertation author is the leading researcher of this study.

6.1 Introduction

Parallel measurements can allow us to estimate multiple parameters with available resources simultaneously. If the sensitivity of these measurements is limited to the SNL, quantum squeezed states of light can enhance their sensitivity further. In particular, multi-mode quantum states can perform multiple measurements or probe multiple sensors simultaneously to estimate multiple parameters in parallel. Therefore, quantum sensing is extendable to complex sensing architectures. This allows us to benefit efficiently from available quantum resources for implementing fast measurements beyond the SNL [152, 153, 154]. Various applications which require parallel optical readout of multiple parameters, including microscopy, spectroscopy, gravitational wave detection, molecular tracing [38, 76, 116, 155, 156, 157, 158, 159], can benefit from multi-spatial-mode twin beams of light to enable a quantum multi-parameter estimation configuration [160, 161]. Such parallelism requires the existence of quantum correlations in multiple modes to estimate multiple parameters on a single sensor, or to perform

multiple measurements on multiple sensors each probed by a different quantum spatial mode.

In particular, if the quantum correlated modes are spatially resolvable, these modes can be used to probe an array of spatially distributed sensors in parallel. Twin beams of light are intrinsically capable of carrying quantum correlations in multiple spatial modes [162]. Each pair of these temporally correlated modes in the transverse plane of the probe and conjugate can ideally be treated as independent quantum correlated beams of light [163]. Spatial squeezing has been shown to be applicable in parallel quantum-enhanced sensing for biological imaging and molecular tracking [76, 77] and for enhancing the sensitivity of beam displacements [35, 164]. Similarly, the multi-spatial-mode nature of the twin beams allows us to perform parallel sensing. For example, with an array of sensors and a corresponding array of photodetectors, one can utilize localized correlations in the subregions of the twin beams to perform a spatially-resolved distributed parallel quantum sensing. These independent spatial subregions of the twin beams result from the phase-matching condition, as introduced in section 2.4.2.

In chapter 5, we implemented a quantum-enhanced sensing setup to probe a single plasmonic sensor by using twin beams of light and directly measuring changes in the refractive index of air with a sensitivity beyond the SNL. In that setup, the spatial correlations in the twin beams were averaged over all the spatial subareas by focusing the beam on a single photodetector. Here, we extend that setup to exploit the quantum correlations embedded in the transverse plane of the twin beam to independently probe four plasmonic sensors with independent spatial subregions of the twin beam. This

allows us to enhance the sensitivity of the array of four independent plasmonic sensors in a parallel configuration. As introduced in chapter 4, plasmonic sensors detect local modulations in the refractive index of air in their proximity.

The parallel quantum plasmonic sensing described here is a proof-of-principle for practical parallel quantum information [165] and is a step towards realizing a spatially resolved quantum sensing configuration. Moreover, it illustrates a new path to take advantage of quantum resources in various degrees of freedom for sub-shot-noise sensing applications. These results can be applied to other parallel plasmonic sensing setups which are conventionally probed with classical states of light [116, 158, 159] to enhance them through the available temporal and spatial quantum correlations in twin beams.

In this chapter, we first describe the building blocks for the experimental implementation of our parallel quantum plasmonic sensing. Then, we discuss the results for parallel detection of modulations in the refractive index of air below the SNL.

6.2 Experimental Setup

The experimental setup that we use for the quantum parallel sensing is shown in Fig. 6.1, which extends the setup described in chapter 5 [73]. Here, instead of one plasmonic sensor, an array of four plasmonic sensors (quadrant plasmonic sensor, QPS) is probed simultaneously with multiple spatial modes in the twin beams to detect local modulations in refractive index of air at each sensor independently. The corresponding correlated subareas of the conjugate beam are masked with an array of four masks

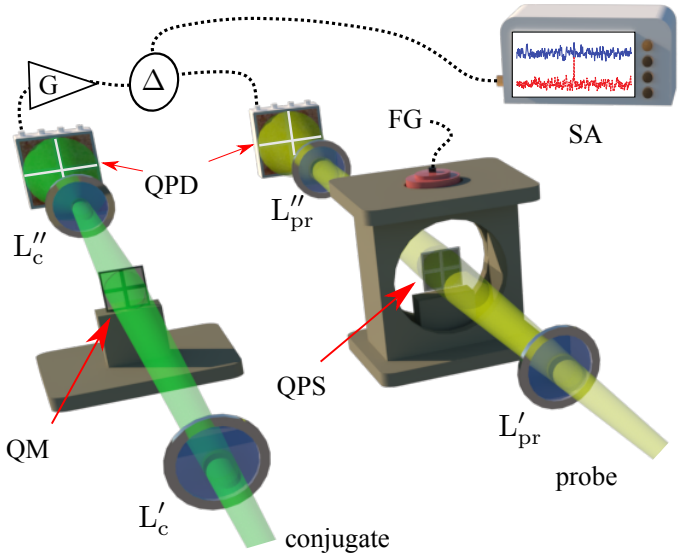

Figure 6.1: Experimental setup for parallel quantum plasmonic sensing. Function generator (FG) drives the ultrasound buzzer at 400 kHz. QPS: quadrant plasmonic sensor, QM: quadrant mask, QPD: quadrant photodetector, SA: spectrum analyzer, G: EA, Δ: subtraction port of the HJ.

(quadrant mask, QM) to select the four reference subareas. The size and position of the QM are designed to be identical to the QPS to ensure the corresponding spatial subareas in both twin beams are selected. The outgoing four pairs of corresponding subregions of the twin beam after the QPS and the QM are imaged on a pair of quadrant photodetectors (QPD) to perform four independent ID measurements.

6.2.1 Multi-Spatial-Mode Twin Beams

For our experiment, the twin beams of light are generated with the FWM process in the D1 line of hot ^{85}Rb atoms, as described in chapter 2. The experimental parameters used for the experiment described in this chapter are listed in table 6.1. With these parameters the FWM generates twin beams with an initial ID squeezing of -5.2 dB.

As discussed in section 2.4, subareas in the twin beams can independently preserve the squeezing level of the initial twin beams. Moreover, the squeezing at our measured frequency (400 kHz) between subareas of the twin beams is preserved only in the near field. To verify this behavior, we placed razor blades in the path of the twin beams at the image plane of the Rb cell (near field) to block half or three quarters of the beams. As was shown in Fig. 2.19, we verified that the ID noise spectrum between the remaining subareas of the twin beam almost maintain the level of squeezing of the whole beam. We have also verified that in a far field plane, the noise of the clipped subareas of the twin beam cannot be cancelled at low frequencies and show excess noise (not shown here) [70]. Therefore, we choose the near field as the sensing plane for implementing our experimental parallel quantum sensing.

Parameter	**Value**
FWM Gain	~ 8
Pump Diameter ($1/e^2$)	3.0 mm
Pump Power	~ 1.9 W
Probe Diameter ($1/e^2$)	2.5 mm
Δ (one-photon detuning)	1.05 GHz
δ (two-photon detuning)	6 MHz
Pump-Probe Angle	0.53°
Cell Temperature	111° C
ID Squeezing	-5.2 dB

Table 6.1: Experimental parameters for the FWM process optimized to generate multi-spatial-mode squeezed states.

With the experimental settings for the FWM process listed in table 6.1, the initial -5.2 dB of squeezing is reduced to -4.5 dB when only one subarea of a quarter of the size of the twin beams is left. As mentioned in chapter 5, the source is capable of achieving a squeezing level as high as -9 dB with the experimental parameters listed in table 5.3 [73]. However, those parameters do not provide the large number of spatial modes needed for parallel sensing. This behavior manifests the trade-off between producing a large level of squeezing with the whole twin beam vs. having a large number of spatial modes that exhibit squeezing.

6.2.2 Quadrant Plasmonic Sensors

The sensors that we use for parallel sensing are plasmonic sensors whose operating mechanism is explained in chapter 4, and have the same nanohole structures as the single sensors used in the experiments of chapter 5. The particular plasmonic structures that we use in this chapter are also composed of a periodic array of subwavelength triangular nanoholes*. in a thin silver film ($\approx$ 100 nm thick) deposited on a glass substrate. A microscope image of the QPS is shown in Fig. 6.2(a), where each quadrant is a single plasmonic sensor (200 μm $\times$ 200 μm). The gap between the quadrant sensors (20 μm) is to isolate the four sensors. Numbers in the microscope image indicate the way we label each one of the quadrant sensors on the probe beam as p_i, with $i = 1 - 4$. The characteristic transmission resonance responses of these four plasmonic sensors are given in Fig. 6.2(b). To perform the white light spectroscopy for the transmission of these

*SEM images are shown in Fig. 4.4(b)

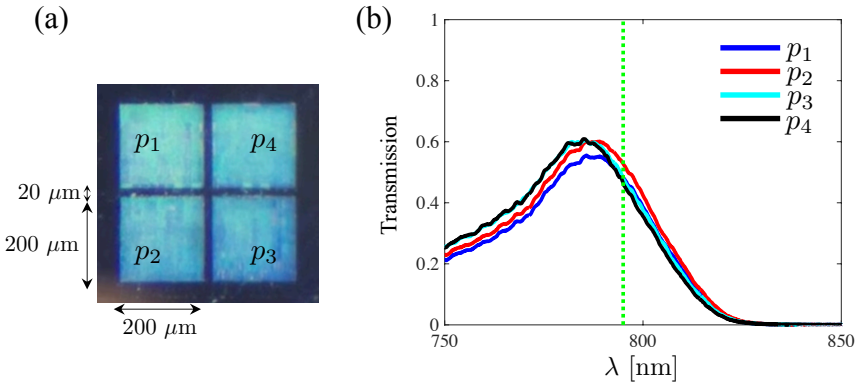

Figure 6.2: The QPS used in our parallel quantum sensing experiment. (a) Microscope image of the QPS. (b) Normalized EOT spectra of the four independent plasmonic sensors. When the sensors are tilted by $\approx 22°$, their transmissions reach $\sim 50\%$ at $\lambda = 795$ nm.

sensors, the angle of incidence on the plasmonic sensor is optimized for transmission amplitude and slope at 795 nm. By changing the angle of incidence, the effective periodicity of the nanoholes changes, which can shift the resonance response of the plasmonic sensors to higher wavelength. These plasmonic sensors show nearly 50% transmission at $\approx 22° \pm 2°$ incidence angle.

6.2.3 Imaging System: Beam Size at Sensing Plane

To take advantage of these quantum correlated subareas of the twin beam in the near field for our parallel sensing purpose, we image the center of the vapor cell onto the sensing plane (the location of plasmonic sensors). To find the location of the near field of the Rb cell to place the QPS and QM in the path of the twin beams, we place a target mask (Thorlabs NBS 1963A) with a pattern of number 18 on the seeding probe

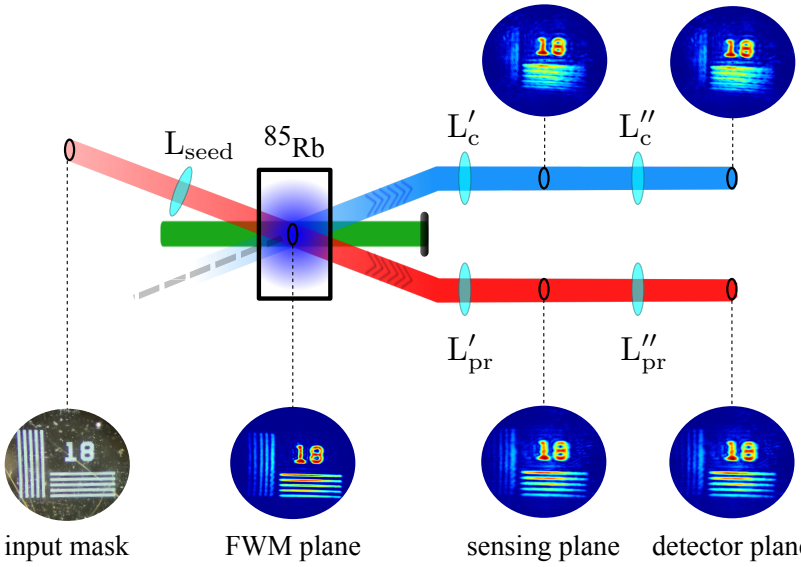

Figure 6.3: Setup for finding the image planes for the near field using a Thorlabs target mask with number 18. The QPS and QM are placed at the "sensing plane". The quadrant detectors are placed at the "detector plane". Not to scale.

before the Rb cell. Using an imaging lens system, shown as L_{seed} in Fig. 6.3, we image this target mask to the center of the Rb cell to seed the FWM process and generate entangled images. Two telescope systems are placed after the cell, shown as L'_{pr} and L'_{c} for the probe and conjugate beams in Fig. 6.3, respectively, to transfer these images from the center of the cell to the sensing plane. This sensing plane is where we put the QM and QPS for our parallel sensing. These imaging systems form clear and sharp near field images with the desired magnification, which will be explained shortly.

Due to the Kerr nonlinear focusing effect caused by the intense pump beam for the FWM, the sharp image of the probe gets slightly blurry and the imaging plane is slightly shifted along the beam from where it was without the pump beam. We adjust the sensing plane to place the QPS and QM accordingly to compensate for this effect. The images of the alignment mask on the twin beams at the sensing plane are shown in Fig. 6.3. As we can see, in the near field, the generated entangled images are exact copies of each other with the same orientation. We need to emphasize that this target mask was only used for alignment purposes. After finding the near field sensing planes, the aligning mask was removed to perform the measurement with spatially multi-mode twin beams with a bright Gaussian profile.

The imaging system after the FWM (L'_{pr} in Fig. 6.3) also demagnifies the probe beam to illuminate the QPS with a Gaussian waist diameter ($1/e^2$) of 360 μm. This ensures the illumination of a maximum area of the QPS without being leaked at the outer edges of the sensor, while having the smallest area of the beam blocked by the 20 μm silver division separating the sensors. This division isolates individual sensors

from any cross-talk between them while performing parallel sensing.

Another imaging system, shown as L_c' in Fig. 6.1, demagnifies the conjugate beam to illuminate the QM with a Gaussian profile with waist diameter of $1/e^2 = 360$ μm. The QM on the conjugate beam allows us to access subareas in transverse plane of the conjugate beam which are correlated with the corresponding subareas of the probe beam, while blocking the uncorrelated subregions. The QM is also aligned to the conjugate beam with the same angle ($22^\circ \pm 2^\circ$) as the QPS is aligned to the probe. These considerations assure maximum overlap between the correlated subareas in the twin beams that make it through the QPS and QM, leading to the maximum cancellation of quantum noise.

The optimum size of the beams illuminating the QPS and QM is obtained from modeling the optimum size of the Gaussian waist diameter of an incident beam that can provide maximum transmission through the QM. The Gaussian profile can be described as:

$$\text{Gaussian} = \frac{1}{2\pi\sigma_x\sigma_y} \exp\left[-\left(\frac{x^2}{2\sigma_x^2} + \frac{y^2}{2\sigma_y^2}\right)\right], \tag{6.1}$$

for waist diameters of σ_x and σ_y along the x- and y-directions, respectively, and centered at the origin. We then integrate the total power of the Gaussian beam with different waist sizes ($\sigma = \sigma_x = \sigma_y$) to find the maximum total power passing through the QM. The size and the tilting angle of the QM in this model are set equal to the ones of the QPS and QM in the experiment, as $[d\cos(\theta)]$ along the x-direction and d along the y-direction. As mentioned before, the horizontal tilting is $\theta = 22^\circ$ and $d = 200$ μm. The result of this modeling is plotted in Fig. 6.4, which shows a maximum transmission

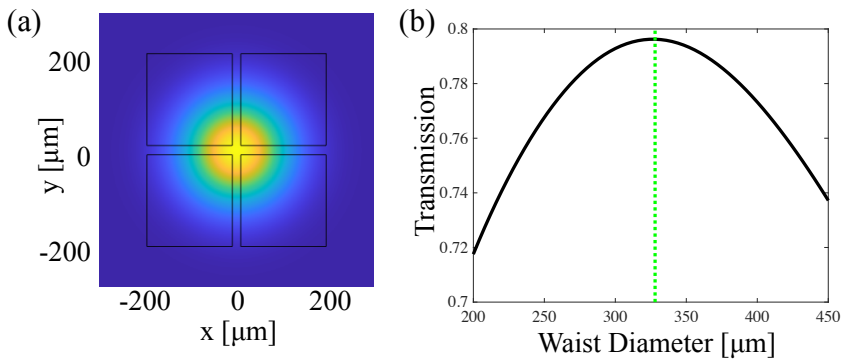

Figure 6.4: (a) Gaussian profile of output beam at the QM or QPS. (b) Transmission of the Gaussian beam through a QM as a function of the beam waist diameter. Transmission is maximum for a waist diameter of about 330 μm. Here, the QM is tilted by 22°.

of $\approx 80\%$ at a waist diameter of about 330 μm. Due to the technical limitations, the experimental beam size of the twin beams on the QPS and the QM are 360 μm. As can be seen from Fig. 6.4(b), the transmission does not change much from the theoretical optimum beam diameter.

6.2.4 Quadrant Detectors with Home-Built Electronics

The eight quadrants of the twin beam, four from the probe beam after transducing through the QPS and four from the conjugate after passing through the QM, are magnified and imaged on two independent QPDs (Hamamatsu, S5980/-10, each quadrant of the four photodetectors is 2.48 mm$\times$ 2.48 mm), with a quantum efficiency of about 95% at 795 nm. A telescope lens system, indicated as L''_{pr} for probe arm and L''_{c} for conjugate arm in Fig. 6.1, was used for magnifying and imaging the eight quadrants

onto the corresponding eight photodetectors. These lens systems consist of an aspheric lens (Thorlabs A240TM-B) and a 2-inch diameter lens. The aspheric lens has an effective focal length of EFL0.8 mm and a numerical aperture of NA= 0.5 to capture the maximum amount of light diffracted from the QPS and QM. The detection plane for placing the quadrant detectors was also verified by using the target mask on the seed probe and forming the entangled images, as shown in Fig. 6.3.

Since the QPS and the QM are imaged on the QPDs for each beam, we label the QPDs according to its corresponding subareas of the twin beam. As we labeled the QPS on the probe beam with p_i $(i = 1 - 4)$, we label the QPD for the QPS with the same labels. Also, we label the QM on the conjugate beam as c_i $(i = 1 - 4)$. Accordingly, we label the QPD capturing the light from the QM with the same labels as c_i $(i = 1 - 4)$.

We have designed and assembled the electronics for the QPD such that we can access the low- (DC) and high-frequency (RF) components of the individual detectors. The high-frequency components of a pair of QPDs, one from the probe's quadrant and another one from the conjugate's quadrant, are subtracted with a HJ. The output of this ID is then analyzed with the SA.

6.2.5 Independence of Multiple Spatial Modes

The presence of multiple spatial modes was verified in section 2.4.2, where we showed that the squeezing is maintained in twin beam subareas by blocking quarters of the beams, as was shown in Fig. 2.19. To check the independence of these multiple spatial subregions in the twin beam, we measure the noise of the twin beam subareas

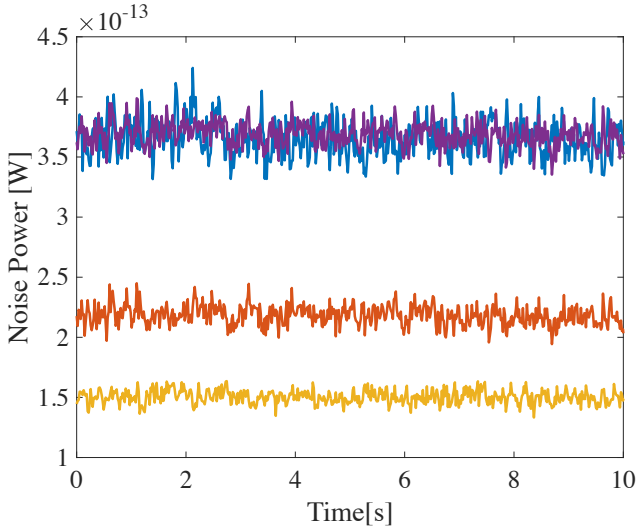

Figure 6.5: Noise power from individual quadrants for the probe p_3 (yellow) and the conjugate c_4 (red). The ID signal from $p_3 - c_4$ (blue) overlaps the signal from adding (on the computer) the signal from the two quadrants $p_3 + c_4$ (violet). This indicates that the spatial subregions of the twin beam are independent. SA analysis frequency: 400 kHz.

individually (subareas p_i from the QPS and c_j from the QM, for instance), as well as the ID measurement between them. Due to the spatial multi-mode nature of the quantum correlations in the twin beams, selecting a pair of quantum correlated quadrants leads to a noise reduction, while the noise of an ID measurement between uncorrelated quadrant pairs adds up in quadrature. Since the sensing plane of this experiment is in the near field, a quadrant subarea of the probe beam is quantum-correlated with the quadrant subarea of the conjugate beam with the same label, i.e. p_i and c_i. On the other hand, uncorrelated quadrant subareas of the twin beam are labeled with different indices: p_i and c_j with $i \neq j$. The results of such a test measurement for quadrant pairs $p_3 - c_4$, are shown in Fig. 6.5, where the noise power of the uncorrelated subareas adds up in quadrature and reaches the same level as that of adding the noise of the individual uncorrelated quadrants. This explicitly shows that the quadrant subareas of the twin beam are independent from each other.

6.3 Implementation of Parallel Quantum Plasmonic Sensing

Similar to the experiment presented in chapter 5, we modulate the index of refraction using an ultrasound buzzer in a controlled environment and perform measurements with twin beams. In this chapter, the measurements will be done on all four plasmonic sensors in parallel. The QPS is probed by four independent subareas of the probe beam and the QM is used to select the quantum-correlated quadrants on the conjugate beam. We can perform ID measurements between 16 pairs of QPS and QM. Four pairs have

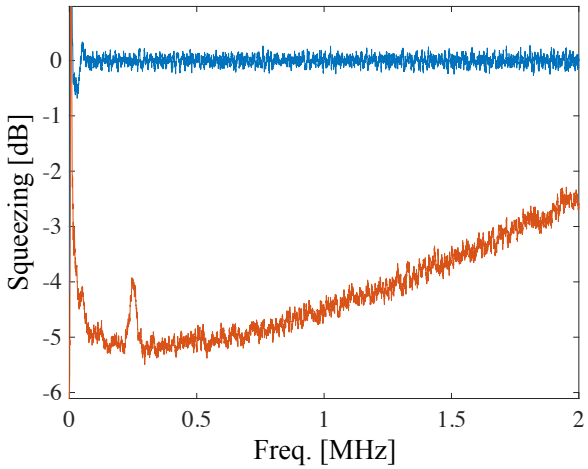

Figure 6.6: Initial squeezing spectrum (red) normalized to the SNL (blue) from an ID measurement. Each beam is focused onto a single photodetector.

quantum correlations and the ID measurement can result in a squeezed measurement. The other twelve pairs are uncorrelated and will exhibit excess noise as they correspond to independent spatial regions.

6.3.1 Experimental Results

We first measure the initial squeezing spectrum of the twin beam right after the FWM process by focusing each beam on a single photodetector and performing an ID measurement. The squeezing spectrum is shown in Fig. 6.6. The squeezing of our twin beam has a maximum noise reduction, reaching a -5.2 dB squeezing, at ~ 400 kHz. Therefore, we choose to perform our parallel plasmonic sensing with a signal modulated at this frequency.

When performing the experiment, the probe beam of the twin beams under-

goes $\approx 48\%$ transmission from the plasmonic QPS (QPS transmission $\sim 50\%$, glass substrate transmission $\sim 95\%$) and the conjugate beam undergoes about 90% transmission from the QM on its path. Since optical loss in the probe quadrants is significantly higher than the one in the conjugate beam, the home-built electronics for the QPDs allow us to insert a variable EA on the conjugate detectors and maximize the noise reduction in the tiwn beam quadrants. By scanning over different values of the variable EA, with an EA of -6 dB, we can maximally cancel the quantum noise in the correlated pairs of quadrant detectors. With these values, we expect theoretically (see section 2.3.3) to achieve ≈ -2.5 dB of squeezing in each quadrant after losses and the insertion of the EA. In this estimation, we assume that the size of the coherent areas in the twin beam are infinitely small, or alternatively, that each quadrant subarea of the twin beams contains an infinite number of coherence areas. Therefore, selecting the subareas for the QPS and the QM would not reduce the squeezing in the twin beam subareas.

The remaining squeezing between correlated pairs of quadrant twin beams after the QPS and QM is experimentally measured to be: $p_1 - c_1 \approx -1.4$ dB, $p_2 - c_2 \approx -1.2$ dB, $p_3 - c_3 \approx -1.0$ dB, and $p_4 - c_4 \approx -1.1$ dB. The difference between the expected and the measured levels of squeezing is due in part to the finite size of the coherence areas and an imperfect alignment of the imaging planes and corresponding quadrants.

6.3.2 SNL Calibration

The SNL can be measured with coherent states of the same optical power as the twin beam quadrants while keeping the optimum EA of the conjugate detector fixed to the

level determined with the twin beams. For a pure coherent state, an ID measurement with imbalanced optical losses and an optimum EA on the conjugate detector provides the real SNL. Since we do not have a pure coherent state, we check whether our measurement becomes shot-noise limited when we use a laser beam which does not undergo FWM. We verify that our measurement is at the SNL showing a linear behavior for the noise vs. total optical power. Also, this behavior matches fairly well with the expected values for calibrating the SNL with a pure coherent state.

6.3.3 Signal Generation

As introduced in chapter 5, we generate the modulation signal by driving an ultrasound buzzer (Multicomp: MCUSD-11A400B11RS) to emit ultrasound pressure waves at its resonance frequency, in this case at 400 kHz. Similarly, the ultrasound buzzer and the QPS are placed inside the same hermetically sealed chamber described in section 5.2.2. By driving the ultrasound buzzer, the standing pressure waves inside the chamber generate modulations in the refractive index of air with different amplitudes near each quadrant of the QPS. As a result, transmission modulations through each quadrant of the QPS give rise to four modulation signals with different amplitudes on each quadrant subarea of the probe beam. With the configuration that we use, this informations is accessed individually and in parallel by the corresponding QPDs. The amplitude of these signals is proportional to the driving voltage of the ultrasound buzzer as well as the response of the individual plasmonic sensors, and if large enough, can be resolved from the noise associated with the probing field.

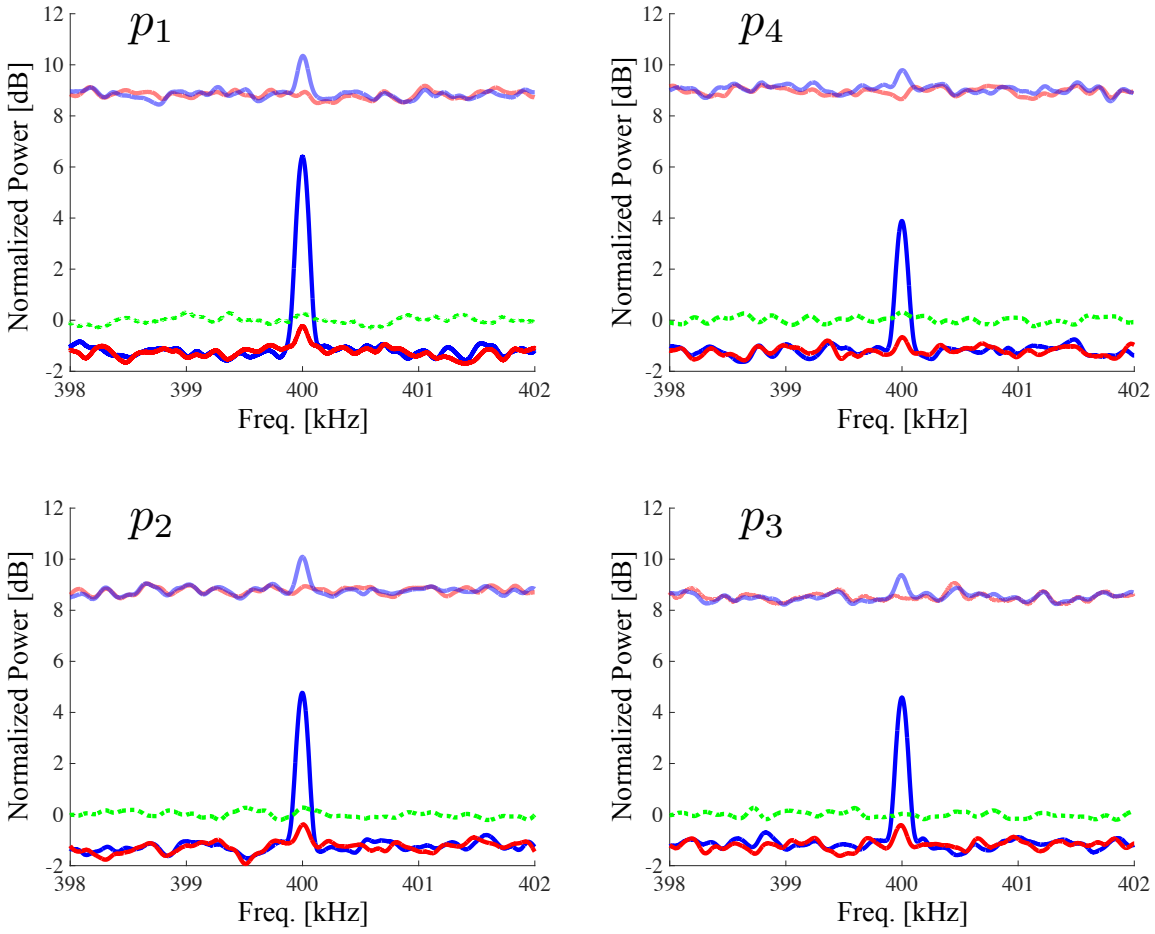

Figure 6.7: Parallel plasmonic sensing of local modulations in the refractive index of air, with 400 mV (blue), and 100 mV (red) driving voltage of the buzzer. All the traces are normalized to their corresponding SNL (dotted green). The noise of correlated subareas (solid) falls below the SNL, while the noise of uncorrelated ones adds up in quadrature (pale traces). SA settings: RBW: 100 Hz, VBW: 3 Hz, power averaged by 200 times.

The power spectra (normalized to the SNL) for parallel detection of the modulation signal with individual quadrants of the QPS p_i $(i = 1 - 4)$, are shown in Fig. 6.7. For each quadrant, higher driving voltages of the buzzer generate larger signals at the modulation frequency. However, due to the multi-spatial-mode nature of the twin beams, the noise for a given measurement with each quadrant for the probe without the modulation depends on the conjugate quadrant subarea c_i $(i = 1 - 4)$.

The solid traces in Fig. 6.7 show the modulation signals and the noise levels measured with ID measurements between QPDs of the corresponding subareas in the twin beams, i.e. $p_i - c_i$ for two driving voltages: 400 mV (blue) and 100 mV (red). This configuration corresponds to the quantum-correlated subareas of the twin beams in the near field. On the other hand, subtracting the signal from uncorrelated QPD pairs leads to an excess noise above the SNL, as the noise of the uncorrelated quadrants add in quadrature, as shown in section 6.2.5. This indicates that the multiple spatial modes of the twin beam are independent of each other. The higher noise level of uncorrelated quadrant pairs $p_i - c_j$ with $i \neq j$ prevents us from resolving the modulation signal, as shown by pale traces in Fig. 6.7. All traces are normalized to the mean of their corresponding SNL values, which are shown by dotted green traces.

6.3.4 Ramping Modulations

The results with modulation signals at discrete voltages clearly prove the capability of the twin beam to simultaneously enhance the sensitivity of the four plasmoinc sensors and to detect modulation signals below the SNL in parallel. We can also quantify

the quantum-enhancement in the sensitivity of these sensors by finding the smallest modulation signal that can be resolved with the twin beam in comparison to a coherent state. That is, by measuring the SNR using twin beams and coherent states of the same optical power on each QPS, and then comparing the modulation voltages at which the SNRs become equal to one. To do so, we linearly increase the amplitude of the buzzer's driving voltage, which consequently increases the amplitude of the modulations in the refractive index of air. The SA is triggered and synchronized with the function generator to record the increasing modulation signals from each sensor, at the modulation frequency. Similar to the measurements with discrete driving voltages, the noise can only go below the SNL when the corresponding correlated quadrants are chosen.

To measure the SNR for each quadrant of the QPS, we first extract the modulation signal from the noise by subtracting the signal without any modulations from the signal with the modulation on. The square root of the ratio between the extracted signal to the noise for correlated (uncorrelated) quadrant pairs gives the SNR of each sensor with spatially correlated (uncorrelated) quadrants of the twin beams. Figure 6.8 shows the SNR traces for parallel sensing with the four plasmonic sensors, which follow a linear behavior, as shown by solid lines fitted to the data. Out of the 16 possible combinations of QPD quadrant pairs from the QPS and QM, only four of them show quantum correlations and have better SNR than the coherent states, as expected.

The magnitude of the modulation signal at each driving voltage depends on the optical power and the location of the probing subarea of the sensors. To measure the

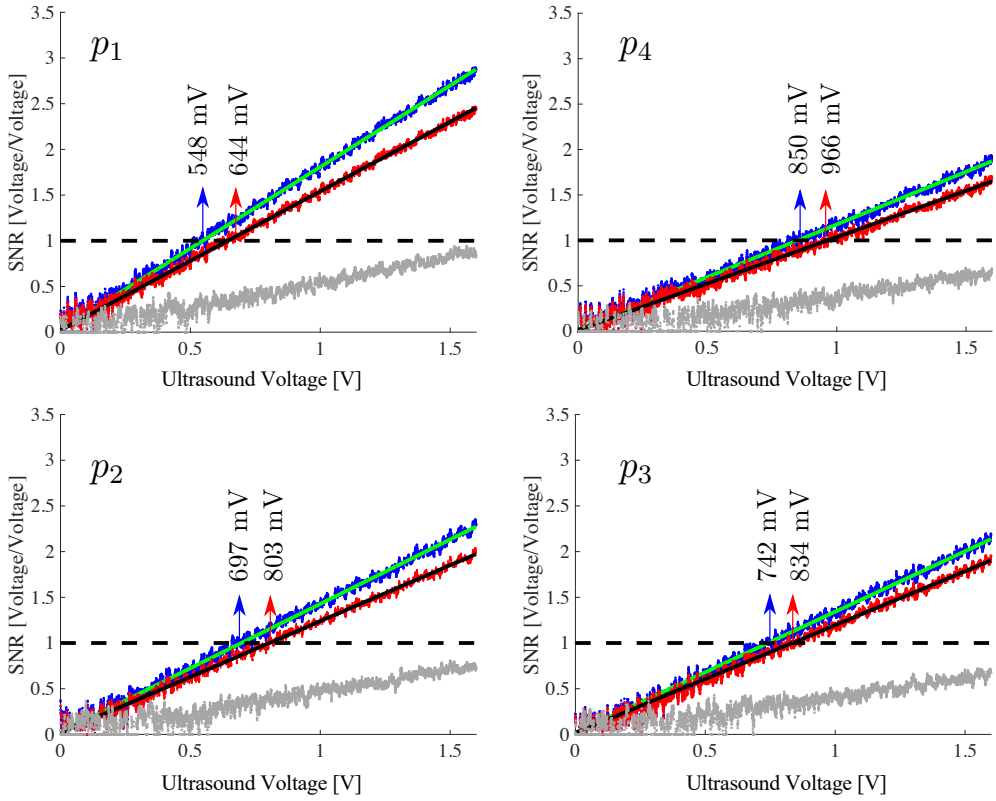

Figure 6.8: SNR for parallel quantum sensing with four independent plasmonic sensors as a function of the driving voltage of the ultrasound buzzer at 400 kHz. Correlated subareas of the twin beams (blue) have better SNR than the estimated SNR for a coherent state (red). SNR with uncorrelated quadrants are shown with gray traces. Arrows indicate the voltages where the SNR= 1 (shown by black dashed lines) for each QPS. SA settings: RBW: 1 kHz, VBW: 10 Hz, power averaged 50 times.

SNR with coherent states, we need to probe the QPS with the same beam size and optical power. To use the probe beam as a coherent state, we need to block the pump beam to prevent the nonlinear amplification through the FWM process. However, the size of the probe mode of the twin beam changes when the FWM process is on, due to the cross-Kerr lensing effect of the intense pump beam. When the FWM process is turned off, the size of the probe beam on the QPS increases, which changes the optical readout of each plasmonic sensor. Therefore, since changing the optical system for imaging will change the optical path of the probe beam on the QPS and we cannot ensure probing exactly the same modulations in refractive index, we are not able to compare the same signals that are measured with a coherent state to the ones we obtained using the twin beam. However, for large enough signals, we can assume that the magnitude of the modulation signal can properly be extracted by subtracting the noise in each measurement. Under this assumption, we can directly measure the SNR for the QPS using twin beams, while estimating the SNR for a coherent state of the same power as the probe and conjugate beams before the QPS and QM.

Knowing the SNR of individual sensors with twin beams and a coherent state, we can quantify the QEF, as defined in section 3.5. Using the SNR plots in Fig. 6.8, we can find the modulation voltages for which the SNR values become equal to one. For example, we can calculate the QEF for plasmonic sensor p_1. The SNR with a coherent state becomes one at $V_d^{\mathrm{CS}} = 644$ mV, while the SNR with the correlated quadrant pair of the twin beams, i.e., p_1 and c_1, becomes one at $V_d^{\mathrm{TB}} = 548$ mV, as indicated by arrows in Fig. 6.8. The ratio of these two voltages provides a direct measure of a 17.7%

QEF by using twin beams over a coherent state at the SNL. This value matches with the theoretically expected QEF with the remaining 1.4 dB of squeezing in this pair, as described in section 3.5.

The measured SNR of the QPS quadrant p_i with correlated quadrants of the twin beam are shown with the blue traces in Fig. 6.8, while the estimated SNR values with a coherent state are shown with the red traces. Solid lines represent linear fits to the SNR data. The noise of the correlated pairs of the twin beam subareas is below the SNL, leading to SNR values higher than the SNR of a coherent state. As expected, the uncorrelated pairs of the twin beam subareas have higher noise than the SNL, leading to the smallest SNR values, as shown with the gray traces in Fig. 6.8.

Knowing the absolute value of the smallest detectable change in the refractive index, or the sensitivity of each QPS, requires calibrating the amplitude of the modulations in the index of refraction of air inside the chamber. By refractometry methods, such as a Mach-Zehnder interferometer, we can calibrate these changes with respect to the driving voltage of ultrasound buzzer, as described in section 5.2.3. Since our main goal was to demonstrate parallel quantum plasmonic sensing below the SNL, the sensors' absolute sensitivity is not needed, and such calibrations were not conducted in the current study. However, as we showed in chapter 5, the sensitivity of such QPS is of the order of the current state-of-the-art for plasmonic sensors [73].

6.4 Conclusion

The configuration presented here for spatially resolved quantum sensing can open new doors to numerous sensing configurations and different applications. For example, other compatible sensors can be used instead of plasmonic sensors, or different parameters, such as phase or polarization, can be measured with each sensor in parallel. Moreover, the motion of bio-chemical samples can be detected and tracked at each subarea. These applications can also be extended to more than four quadrants to increase the spatial resolution of the sensing configuration.

In conclusion, we have implemented a parallel quantum-enhanced plasmonic sensing configuration to detect modulations in the refractive index of air in four parallel independent plasmonic sensors below the SNL. With an average squeezing of about -1.2 dB on each quadrant of the QPS, we could detect local modulations in the refractive index of air with up to $\approx 17.7\%$ higher sensitivity than measurements with a coherent state. Using sensors with less optical losses or using alternative measurement parameters, such as phase, can improve the overall sensitivity of the presented quantum-enhanced parallel plasmonic sensing scheme. We believe this study provides a proof-of-principle for implementing parallel quantum sensing and can be extended to more complex parallel sensing configurations.

Chapter 7

Conclusions and Future Work

In this thesis, we studied the building blocks for quantum sensing needed to take advantage of quantum correlations in two-mode squeezed states of light to surpass the SNL. In particular, we presented a practical application of these squeezed states to enhance the sensitivity of a plasmonic sensor and implemented a quantum-enhanced plasmonic sensor. Moreover, we presented an experimental setup for spatially resolved quantum sensing for parallel detection of local changes in the refractive index of air below the SNL.

The implementation of quantum-enhanced sensing presented here points towards further improvements in the sensitivity of current state of the art plasmonic sensors to analyse lower concentrations or dynamics of biochemical samples and enable higher precision levels in single molecule bio-sensing detection. These results are important when the lower detection limit is bounded by the SNL and detecting smaller changes beyond that limit is required. In addition to plasmonic sensors, other classical sensing and measuring devices, and detectors with optical readouts at the SNL can benefit from the use of these squeezed states of light.

In the future, we will explore different nanohole structures to use as plasmonic sensors by performing simulations on different shapes and sizes to obtain optimum values for the sensitivity and higher transmissions that will allow us to take maximum advantage of the quantum properties. Using COMSOL, we can optimize the parameters

for designing different nanohole architectures to obtain higher EOT transmissions and steeper slopes. The main limiting factor is in the fabrication process, which requires special care to be able to obtain the sensitivities predicted from simulations.

Once we obtain proper samples with predicted resonances for quantum plasmonic sensing, we will extend the current study to benefit further from the use of squeezed light. With the design of nanoholes with slightly different periodicities along the x- and y-directions, we can obtain higher sensitivities by probing the sensor with both of the twin beams. This way, using an ID measurement reduces the quantum noise between the twin beams, while the modulation signal from the shift of the EOT resonance adds up due to opposite slopes. However, this preliminary idea needs more theoretical studies as losses in the conjugate arm will reduce the amount of quantum-enhancement that we initially might expect.

Furthermore, with the promising progress in fabricating nanohole structures, we can perform quantum plasmonic sensing experiments with new nanohole structures that have asymmetric two-hole unit cells. As we have predicted, we expect to achieve higher absolute sensitivities with these new designs. Such experiments will further enhance the sensitivity of state-of-the-art plasmonic sensors, while enabling the detection of changes in the refractive index below the SNL.

The parallel sensing configurations can also provide several applications and opens new paths to explore. Since each subarea in the twin beams acts as an independent probe beam, it offers several applications. Here, we propose a few potential ideas for future references.

– Multiple particle detection: Detection of different particles at the location of each QPS allows simultaneous probing of multiple sensors, each for detecting a different particle or contamination.

– Multiple parameter estimation: On the detection end, since all the ports of the QPDs are accessible, we can perform independent measurement for each quadrant sensor. For example, we can perform HD measurements to estimate phase changes with one sensor and transmission changes with another sensor.

– Tracking applications: By designing the setup to have smaller coherence areas, we can increase the spatial resolution and use smaller detectors, such as a CCD camera, to track the coordinate of a particle withing the probe beam.

References

[1] V. Giovannetti, S. Lloyd, and L. Maccone, "Quantum-enhanced measurements: beating the standard quantum limit," *Science*, vol. 306, no. 5700, pp. 1330–1336, 2004.

[2] J. Homola, S. S. Yee, and G. Gauglitz, "Surface plasmon resonance sensors: review," *Sensors and Actuators B: Chemical*, vol. 54, no. 1, pp. 3–15, 1999.

[3] M. Piliarik and J. Homola, "Surface plasmon resonance (spr) sensors: approaching their limits?," *Optics Express*, vol. 17, no. 19, pp. 16505–16517, 2009.

[4] M. Saleem, "The failure of classical physics and the advent of quantum mechanics," *Quantum Mechanics. IOP Publishing*, 2015.

[5] T. H. Maiman *et al.*, "Stimulated optical radiation in ruby," 1960.

[6] C. M. Caves, "Quantum-mechanical noise in an interferometer," *Physical Review D*, vol. 23, no. 8, p. 1693, 1981.

[7] R. J. Glauber, "Coherent and incoherent states of the radiation field," *Physical Review*, vol. 131, no. 6, p. 2766, 1963.

[8] H. J. Kimble, M. Dagenais, and L. Mandel, "Photon antibunching in resonance fluorescence," *Physical Review Letters*, vol. 39, no. 11, p. 691, 1977.

[9] R. Slusher, L. Hollberg, B. Yurke, J. Mertz, and J. Valley, "Observation of squeezed states generated by four-wave mixing in an optical cavity," *Physical Review Letters*, vol. 55, no. 22, p. 2409, 1985.

[10] J. P. Dowling and G. J. Milburn, "Quantum technology: the second quantum revolution," *Philosophical Transactions of the Royal Society of London. Series A: Mathematical, Physical and Engineering Sciences*, vol. 361, no. 1809, pp. 1655–1674, 2003.

[11] I. H. Deutsch, "Harnessing the power of the second quantum revolution," *Physical Review X Quantum*, vol. 1, no. 2, p. 020101, 2020.

[12] B. Yurke and E. A. Whittaker, "Squeezed-state-enhanced frequency-modulation spectroscopy," *Optics Letters*, vol. 12, no. 4, pp. 236–238, 1987.

[13] H. Carmichael, A. Lane, and D. Walls, "Resonance fluorescence from an atom in a squeezed vacuum," *Physical Review Letters*, vol. 58, no. 24, p. 2539, 1987.

[14] E. Polzik, J. Carri, and H. Kimble, "Spectroscopy with squeezed light," *Physical Review Letters*, vol. 68, no. 20, p. 3020, 1992.

[15] M. Xiao, L.-A. Wu, and H. J. Kimble, "Precision measurement beyond the shot-noise limit," *Physical Review Letters*, vol. 59, no. 3, p. 278, 1987.

[16] P. Grangier, R. Slusher, B. Yurke, and A. LaPorta, "Squeezed-light–enhanced polarization interferometer," *Physical Review Letters*, vol. 59, no. 19, p. 2153, 1987.

[17] J. Abadie, B. P. Abbott, R. Abbott, T. D. Abbott, M. Abernathy, C. Adams, R. Adhikari, C. Affeldt, B. Allen, G. Allen, *et al.*, "A gravitational wave observatory operating beyond the quantum shot-noise limit," *Nature Physics*, vol. 7, no. 12, p. 962, 2011.

[18] H. Grote, K. Danzmann, K. Dooley, R. Schnabel, J. Slutsky, and H. Vahlbruch, "First long-term application of squeezed states of light in a gravitational-wave observatory," *Physical Review Letters*, vol. 110, no. 18, p. 181101, 2013.

[19] J. Aasi, J. Abadie, B. Abbott, R. Abbott, T. Abbott, M. Abernathy, C. Adams, T. Adams, P. Addesso, R. Adhikari, *et al.*, "Enhanced sensitivity of the ligo gravitational wave detector by using squeezed states of light," *Nature Photonics*, vol. 7, no. 8, pp. 613–619, 2013.

[20] L. S. Collaboration *et al.*, "A gravitational wave observatory operating beyond the quantum shot-noise limit," *Nature Physics*, vol. 7, no. 12, pp. 962–965, 2011.

[21] R. Schnabel, N. Mavalvala, D. E. McClelland, and P. K. Lam, "Quantum metrology for gravitational wave astronomy," *Nature Communications*, vol. 1, no. 1, pp. 1–10, 2010.

[22] J. Gea-Banacloche and G. Leuchs, "Squeezed states in non-ideal interferometers: the effect of aberrations," *Journal of Modern Optics*, vol. 36, no. 10, pp. 1277–1284, 1989.

[23] C. L. Degen, F. Reinhard, and P. Cappellaro, "Quantum sensing," *Reviews of Modern Physics*, vol. 89, p. 035002, Jul 2017.

[24] C. Lee, F. Dieleman, J. Lee, C. Rockstuhl, S. A. Maier, and M. Tame, "Quantum plasmonic sensing: beyond the shot-noise and diffraction limit," *ACS Photonics*, vol. 3, no. 6, pp. 992–999, 2016.

[25] B. J. Lawrie, P. D. Lett, A. M. Marino, and R. C. Pooser, "Quantum sensing with squeezed light," *ACS Photonics*, vol. 6, no. 6, pp. 1307–1318, 2019.

[26] J. A. Schuller, E. S. Barnard, W. Cai, Y. C. Jun, J. S. White, and M. L. Brongersma, "Plasmonics for extreme light concentration and manipulation," *Nature Materials*, vol. 9, no. 3, pp. 193–204, 2010.

[27] J. Homola, "Present and future of surface plasmon resonance biosensors," *Analytical and Bioanalytical Chemistry*, vol. 377, no. 3, pp. 528–539, 2003.

[28] R. Gordon, D. Sinton, K. L. Kavanagh, and A. G. Brolo, "A new generation of sensors based on extraordinary optical transmission," *Accounts of Chemical Research*, vol. 41, no. 8, pp. 1049–1057, 2008.

[29] V. V. Yakovlev, W. Dickson, A. Murphy, J. McPhillips, R. J. Pollard, V. A. Podolskiy, and A. V. Zayats, "Ultrasensitive non-resonant detection of ultrasound with plasmonic metamaterials," *Advanced Materials*, vol. 25, no. 16, pp. 2351–2356, 2013.

[30] J. Mejía-Salazar and O. N. Oliveira Jr, "Plasmonic biosensing: focus review," *Chemical Reviews*, vol. 118, no. 20, pp. 10617–10625, 2018.

[31] M. Genovese, "Real applications of quantum imaging," *Journal of Optics*, vol. 18, no. 7, p. 073002, 2016.

[32] O. S. Magaña-Loaiza and R. W. Boyd, "Quantum imaging and information," *Reports on Progress in Physics*, vol. 82, no. 12, p. 124401, 2019.

[33] G. Brida, M. Genovese, and I. R. Berchera, "Experimental realization of sub-shot-noise quantum imaging," *Nature Photonics*, vol. 4, no. 4, pp. 227–230, 2010.

[34] V. Boyer, A. Marino, and P. Lett, "Generation of spatially broadband twin beams for quantum imaging," *Physical Review Letters*, vol. 100, no. 14, p. 143601, 2008.

[35] N. Treps, N. Grosse, W. P. Bowen, C. Fabre, H.-A. Bachor, and P. K. Lam, "A quantum laser pointer," *Science*, vol. 301, no. 5635, pp. 940–943, 2003.

[36] D. F. Walls, "Squeezed states of light," *Nature*, vol. 306, no. 5939, pp. 141–146, 1983.

[37] V. Giovannetti, S. Lloyd, and L. Maccone, "Advances in quantum metrology," *Nature Photonics*, vol. 5, no. 4, pp. 222–229, 2011.

[38] M. A. Taylor and W. P. Bowen, "Quantum metrology and its application in biology," *Physics Reports*, vol. 615, pp. 1–59, 2016.

[39] S. Pirandola, B. R. Bardhan, T. Gehring, C. Weedbrook, and S. Lloyd, "Advances in photonic quantum sensing," *Nature Photonics*, vol. 12, no. 12, pp. 724–733, 2018.

[40] C. L. Degen, F. Reinhard, and P. Cappellaro, "Quantum sensing," *Reviews of Modern Physics*, vol. 89, no. 3, p. 035002, 2017.

[41] M. Atzori and R. Sessoli, "The second quantum revolution: role and challenges of molecular chemistry," *Journal of the American Chemical Society*, vol. 141, no. 29, pp. 11339–11352, 2019.

[42] R. J. Glauber, "The quantum theory of optical coherence," *Physical Review*, vol. 130, no. 6, p. 2529, 1963.

[43] L.-A. Wu, M. Xiao, and H. Kimble, "Squeezed states of light from an optical parametric oscillator," *JOSA B*, vol. 4, no. 10, pp. 1465–1475, 1987.

[44] R. Loudon and P. L. Knight, "Squeezed light," *Journal of Modern Optics*, vol. 34, no. 6-7, pp. 709–759, 1987.

[45] M. C. Teich and B. E. Saleh, "Squeezed state of light," *Quantum Optics: Journal of the European Optical Society Part B*, vol. 1, no. 2, p. 153, 1989.

[46] D. Stoler, "Equivalence classes of minimum uncertainty packets," *Physical Review D*, vol. 1, no. 12, p. 3217, 1970.

[47] D. Stoler, "Equivalence classes of minimum-uncertainty packets. ii," *Physical Review D*, vol. 4, no. 6, p. 1925, 1971.

[48] H. P. Yuen, "Two-photon coherent states of the radiation field," *Physical Review A*, vol. 13, no. 6, p. 2226, 1976.

[49] H. Yuen and J. Shapiro, "Optical communication with two-photon coherent states–part iii: Quantum measurements realizable with photoemissive detectors," *IEEE Transactions on Information Theory*, vol. 26, no. 1, pp. 78–92, 1980.

[50] L.-A. Wu, H. Kimble, J. Hall, and H. Wu, "Generation of squeezed states by parametric down conversion," *Physical Review Letters*, vol. 57, no. 20, p. 2520, 1986.

[51] A. M. Marino, *Experimental Studies of Two-Mode Squeezed States in Rubidium Vapor*. PhD thesis, The Institute of Optics, The College School of Engineering and Applied Sciences, University of Rochester, Rochester, New York, 2006.

[52] M. Turnbull, *Multi-spatial-mode quadrature squeezing from four-wave mixing in a hot atomic vapour*. PhD thesis, University of Birmingham, 2014.

[53] A. Lvovsky, "Squeezed light," *Photonics: Scientific Foundations Technology and Applications*, vol. 1, 2014.

[54] R. W. Boyd, *Nonlinear optics*. Academic press, 2020.

[55] C. McCormick, A. M. Marino, V. Boyer, and P. D. Lett, "Strong low-frequency quantum correlations from a four-wave-mixing amplifier," *Physical Review A*, vol. 78, no. 4, p. 043816, 2008.

[56] M. Reid, D. Walls, and B. Dalton, "Squeezing of quantum fluctuations via atomic coherence effects," *Physical Review Letters*, vol. 55, no. 12, p. 1288, 1985.

[57] M. Lukin, A. Matsko, M. Fleischhauer, and M. O. Scully, "Quantum noise and correlations in resonantly enhanced wave mixing based on atomic coherence," *Physical Review Letters*, vol. 82, no. 9, p. 1847, 1999.

[58] P. Hemmer, D. Katz, J. Donoghue, M. Cronin-Golomb, M. Shahriar, and P. Kumar, "Efficient low-intensity optical phase conjugation based on coherent population trapping in sodium," *Optics Letters*, vol. 20, no. 9, pp. 982–984, 1995.

[59] M. Shahriar and P. Hemmer, "Generation of squeezed states and twin beams via non-degenerate four-wave mixing in a λ system," *Optics Communications*, vol. 158, no. 1-6, pp. 273–286, 1998.

[60] H.-A. Bachor, T. C. Ralph, S. Lucia, and T. C. Ralph, *A guide to experiments in quantum optics*, vol. 1. wiley-vch Weinheim, 2004.

[61] H. P. Yuen and V. W. Chan, "Noise in homodyne and heterodyne detection," *Optics Letters*, vol. 8, no. 3, pp. 177–179, 1983.

[62] A. I. Lvovsky and M. G. Raymer, "Continuous-variable optical quantum-state tomography," *Reviews of Modern Physics*, vol. 81, no. 1, p. 299, 2009.

[63] A. I. Lvovsky, "Squeezed light," *Photonics: Scientific Foundations, Technology and Applications*, vol. 1, pp. 121–163, 2015.

[64] B. E. Anderson, P. Gupta, B. L. Schmittberger, T. Horrom, C. Hermann-Avigliano, K. M. Jones, and P. D. Lett, "Phase sensing beyond the standard quantum limit with a variation on the su (1, 1) interferometer," *Optica*, vol. 4, no. 7, pp. 752–756, 2017.

[65] P. Gupta, B. L. Schmittberger, B. E. Anderson, K. M. Jones, and P. D. Lett, "Optimized phase sensing in a truncated su (1, 1) interferometer," *Optics Express*, vol. 26, no. 1, pp. 391–401, 2018.

[66] L.-M. Duan, G. Giedke, J. I. Cirac, and P. Zoller, "Inseparability criterion for continuous variable systems," *Physical Review Letters*, vol. 84, no. 12, p. 2722, 2000.

[67] T. Schneider, *Nonlinear optics in telecommunications*. Springer Science & Business Media, 2004.

[68] M. Martinelli, N. Treps, S. Ducci, S. Gigan, A. Maître, and C. Fabre, "Experimental study of the spatial distribution of quantum correlations in a confocal optical parametric oscillator," *Physical Review A*, vol. 67, no. 2, p. 023808, 2003.

[69] M. Holtfrerich and A. Marino, "Control of the size of the coherence area in entangled twin beams," *Physical Review A*, vol. 93, no. 6, p. 063821, 2016.

[70] M.-C. Wu, N. R. Brewer, R. W. Speirs, K. M. Jones, and P. D. Lett, "Two-beam coupling in the production of quantum correlated images by four-wave mixing," *Optics Express*, vol. 29, no. 11, pp. 16665–16675, 2021.

[71] M. Dowran, T. S. Woodworth, A. Kumar, and A. M. Marino, "Fundamental sensitivity bounds for quantum enhanced optical resonance sensors based on transmission and phase estimation," *arXiv preprint arXiv:2106.07741*, 2021.

[72] M. Holtfrerich, M. Dowran, R. Davidson, B. Lawrie, R. Pooser, and A. Marino, "Toward quantum plasmonic networks," *Optica*, vol. 3, no. 9, pp. 985–988, 2016.

[73] M. Dowran, A. Kumar, B. J. Lawrie, R. C. Pooser, and A. M. Marino, "Quantum-enhanced plasmonic sensing," *Optica*, vol. 5, no. 5, pp. 628–633, 2018.

[74] C. Xu, L. Zhang, S. Huang, T. Ma, F. Liu, H. Yonezawa, Y. Zhang, and M. Xiao, "Sensing and tracking enhanced by quantum squeezing," *Photonics Research*, vol. 7, no. 6, pp. A14–A26, 2019.

[75] R. C. Pooser and B. Lawrie, "Plasmonic trace sensing below the photon shot noise limit," *ACS Photonics*, vol. 3, no. 1, pp. 8–13, 2016.

[76] M. A. Taylor, J. Janousek, V. Daria, J. Knittel, B. Hage, H.-A. Bachor, and W. P. Bowen, "Biological measurement beyond the quantum limit," *Nature Photonics*, vol. 7, no. 3, pp. 229–233, 2013.

[77] M. A. Taylor, J. Janousek, V. Daria, J. Knittel, B. Hage, H.-A. Bachor, and W. P. Bowen, "Subdiffraction-limited quantum imaging within a living cell," *Physical Review X*, vol. 4, no. 1, p. 011017, 2014.

[78] G. Baffou and R. Quidant, "Thermo-plasmonics: using metallic nanostructures as nano-sources of heat," *Laser & Photonics Reviews*, vol. 7, no. 2, pp. 171–187, 2013.

[79] J. N. Anker, W. P. Hall, O. Lyandres, N. C. Shah, J. Zhao, and R. P. Van Duyne, "Biosensing with plasmonic nanosensors," *Nanoscience and Technology: A Collection of Reviews from Nature Journals*, pp. 308–319, 2010.

[80] L. Guo, J. A. Jackman, H.-H. Yang, P. Chen, N.-J. Cho, and D.-H. Kim, "Strategies for enhancing the sensitivity of plasmonic nanosensors," *Nano Today*, vol. 10, no. 2, pp. 213–239, 2015.

[81] F. Yesilkoy, "Optical interrogation techniques for nanophotonic biochemical sensors," *Sensors*, vol. 19, no. 19, p. 4287, 2019.

[82] R. H. Kop, P. De Vries, R. Sprik, and A. Lagendijk, "Kramers-kronig relations for an interferometer," *Optics Communications*, vol. 138, no. 1-3, pp. 118–126, 1997.

[83] B. Gralak, M. Lequime, M. Zerrad, and C. Amra, "Phase retrieval of reflection and transmission coefficients from kramers–kronig relations," *JOSA A*, vol. 32, no. 3, pp. 456–462, 2015.

[84] S. Subramanian, H.-Y. Wu, T. Constant, J. Xavier, and F. Vollmer, "Label-free optical single-molecule micro-and nanosensors," *Advanced Materials*, vol. 30, no. 51, p. 1801246, 2018.

[85] Y. Zhi, X.-C. Yu, Q. Gong, L. Yang, and Y.-F. Xiao, "Single nanoparticle detection using optical microcavities," *Advanced Materials*, vol. 29, no. 12, p. 1604920, 2017.

[86] M. R. Foreman, J. D. Swaim, and F. Vollmer, "Whispering gallery mode sensors," *Advances in optics and photonics*, vol. 7, no. 2, pp. 168–240, 2015.

[87] J. H. Wade and R. C. Bailey, "Applications of optical microcavity resonators in analytical chemistry," *Annual Review of Analytical Chemistry*, vol. 9, pp. 1–25, 2016.

[88] G. Pitruzzello and T. F. Krauss, "Photonic crystal resonances for sensing and imaging," *Journal of Optics*, vol. 20, no. 7, p. 073004, 2018.

[89] S. Deng, P. Wang, and X. Yu, "Phase-sensitive surface plasmon resonance sensors: Recent progress and future prospects," *Sensors*, vol. 17, no. 12, p. 2819, 2017.

[90] X. Zhou, L. Zhang, and W. Pang, "Performance and noise analysis of optical microresonator-based biochemical sensors using intensity detection," *Optics Express*, vol. 24, no. 16, pp. 18197–18208, 2016.

[91] A. V. Kabashin, S. Patskovsky, and A. N. Grigorenko, "Phase and amplitude sensitivities in surface plasmon resonance bio and chemical sensing," *Optics Express*, vol. 17, no. 23, pp. 21191–21204, 2009.

[92] K. Lodewijks, W. Van Roy, G. Borghs, L. Lagae, and P. Van Dorpe, "Boosting the figure-of-merit of lspr-based refractive index sensing by phase-sensitive measurements," *Nano Letters*, vol. 12, no. 3, pp. 1655–1659, 2012.

[93] I. Humer, H. Huber, F. Kienberger, J. Danzberger, and J. Smoliner, "Phase and amplitude sensitive scanning microwave microscopy/spectroscopy on metal–oxide–semiconductor systems," *Journal of Applied Physics*, vol. 111, no. 7, p. 074313, 2012.

[94] B. E. Anderson, B. L. Schmittberger, P. Gupta, K. M. Jones, and P. D. Lett, "Optimal phase measurements with bright-and vacuum-seeded su (1, 1) interferometers," *Physical Review A*, vol. 95, no. 6, p. 063843, 2017.

[95] T. S. Woodworth, K. W. C. Chan, C. Hermann-Avigliano, and A. M. Marino, "Transmission estimation at the cramér-rao bound for squeezed states of light in the presence of loss and imperfect detection," *Physical Review A*, vol. 102, no. 5, p. 052603, 2020.

[96] S. L. Braunstein and C. M. Caves, "Statistical distance and the geometry of quantum states," *Physical Review Letters*, vol. 72, no. 22, p. 3439, 1994.

[97] C. Sparaciari, S. Olivares, and M. G. Paris, "Gaussian-state interferometry with passive and active elements," *Physical Review A*, vol. 93, no. 2, p. 023810, 2016.

[98] H. Vahlbruch, M. Mehmet, K. Danzmann, and R. Schnabel, "Detection of 15 db squeezed states of light and their application for the absolute calibration of photoelectric quantum efficiency," *Physical Review Letters*, vol. 117, no. 11, p. 110801, 2016.

[99] M. Li, S. K. Cushing, J. Zhang, S. Suri, R. Evans, W. P. Petros, L. F. Gibson, D. Ma, Y. Liu, and N. Wu, "Three-dimensional hierarchical plasmonic nano-architecture enhanced surface-enhanced raman scattering immuno-sensor for cancer biomarker detection in blood plasma," *ACS Nano*, vol. 7, no. 6, p. 4967, 2013.

[100] S. Chen, M. Svedendahl, M. Käll, L. Gunnarsson, and A. Dmitriev, "Ultrahigh sensitivity made simple: nanoplasmonic label-free biosensing with an extremely low limit-of-detection for bacterial and cancer diagnostics," *Nanotechnology*, vol. 20, no. 43, p. 434015, 2009.

[101] S.-H. Oh and H. Altug, "Performance metrics and enabling technologies for nanoplasmonic biosensors," *Nature Communications*, vol. 9, no. 1, pp. 1–5, 2018.

[102] A. M. Shrivastav, U. Cvelbar, and I. Abdulhalim, "A comprehensive review on plasmonic-based biosensors used in viral diagnostics," *Communications Biology*, vol. 4, no. 1, pp. 1–12, 2021.

[103] H. H. Nguyen, J. Park, S. Kang, and M. Kim, "Surface plasmon resonance: a versatile technique for biosensor applications," *Sensors*, vol. 15, no. 5, pp. 10481–10510, 2015.

[104] N. C. Lindquist, P. Nagpal, K. M. McPeak, D. J. Norris, and S.-H. Oh, "Engineering metallic nanostructures for plasmonics and nanophotonics," *Reports on Progress in Physics*, vol. 75, no. 3, p. 036501, 2012.

[105] X. Wang, M. Jefferson, P. C. Hobbs, W. P. Risk, B. E. Feller, R. D. Miller, and A. Knoesen, "Shot-noise limited detection for surface plasmon sensing," *Optics Express*, vol. 19, no. 1, pp. 107–117, 2011.

[106] S. Fasel, F. Robin, E. Moreno, D. Erni, N. Gisin, and H. Zbinden, "Energy-time entanglement preservation in plasmon-assisted light transmission," *Physical Review Letters*, vol. 94, no. 11, p. 110501, 2005.

[107] E. Altewischer, M. Van Exter, and J. Woerdman, "Plasmon-assisted transmission of entangled photons," *Nature*, vol. 418, no. 6895, pp. 304–306, 2002.

[108] R. C. Pooser and B. Lawrie, "Plasmonic trace sensing below the photon shot noise limit," *ACS Photonics*, vol. 3, no. 1, pp. 8–13, 2015.

[109] D. A. Kalashnikov, Z. Pan, A. I. Kuznetsov, and L. A. Krivitsky, "Quantum spectroscopy of plasmonic nanostructures," *Physical Review X*, vol. 4, no. 1, p. 011049, 2014.

[110] C. Genet and T. W. Ebbesen, "Light in tiny holes," *Nanoscience And Technology: A Collection of Reviews from Nature Journals*, pp. 205–212, 2010.

[111] X. Liu, J.-H. Kang, H. Yuan, J. Park, S. J. Kim, Y. Cui, H. Y. Hwang, and M. L. Brongersma, "Electrical tuning of a quantum plasmonic resonance," *Nature Nanotechnology*, vol. 12, no. 9, pp. 866–870, 2017.

[112] A. Otto, "Excitation of nonradiative surface plasma waves in silver by the method of frustrated total reflection," *Zeitschrift für Physik A Hadrons and nuclei*, vol. 216, no. 4, pp. 398–410, 1968.

[113] W. L. Barnes, A. Dereux, and T. W. Ebbesen, "Surface plasmon subwavelength optics," *Nature*, vol. 424, no. 6950, pp. 824–830, 2003.

[114] E. Kretschmann, H. Raether, *et al.*, "Radiative decay of non-radiative surface plasmons excited by light," *Z. Naturforsch. A*, vol. 23, no. 12, pp. 2135–2136, 1968.

[115] B. Liedberg, C. Nylander, and I. Lunström, "Surface plasmon resonance for gas detection and biosensing," *Sensors and Actuators*, vol. 4, pp. 299–304, 1983.

[116] H. Im, A. Lesuffleur, N. C. Lindquist, and S.-H. Oh, "Plasmonic nanoholes in a multichannel microarray format for parallel kinetic assays and differential sensing," *Analytical Chemistry*, vol. 81, no. 8, pp. 2854–2859, 2009.

[117] R. H. Ritchie, E. Arakawa, J. Cowan, and R. Hamm, "Surface-plasmon resonance effect in grating diffraction," *Physical Review Letters*, vol. 21, no. 22, p. 1530, 1968.

[118] V. V. Temnov, U. Woggon, J. Dintinger, E. Devaux, and T. W. Ebbesen, "Measuring group velocity of surface plasmons by surface plasmon interferometry," in *Quantum Electronics and Laser Science Conference*, p. QThG3, Optical Society of America, 2007.

[119] W. C. Johnson, "Transmission lines and networks," *McGraw-Hill Electrical and Electronical Engineering Series*, 1963.

[120] T. W. Ebbesen, H. J. Lezec, H. Ghaemi, T. Thio, and P. A. Wolff, "Extraordinary optical transmission through sub-wavelength hole arrays," *Nature*, vol. 391, no. 6668, pp. 667–669, 1998.

[121] F. J. Garcia-Vidal, L. Martin-Moreno, T. Ebbesen, and L. Kuipers, "Light passing through subwavelength apertures," *Reviews of Modern Physics*, vol. 82, no. 1, p. 729, 2010.

[122] V. G. Kravets, A. V. Kabashin, W. L. Barnes, and A. N. Grigorenko, "Plasmonic surface lattice resonances: a review of properties and applications," *Chemical Reviews*, vol. 118, no. 12, pp. 5912–5951, 2018.

[123] L. Martin-Moreno, F. Garcia-Vidal, H. Lezec, K. Pellerin, T. Thio, J. Pendry, and T. Ebbesen, "Theory of extraordinary optical transmission through subwavelength hole arrays," *Physical Review Letters*, vol. 86, no. 6, p. 1114, 2001.

[124] H. Bethe, "Theory of diffraction by small holes," *Physical Review*, vol. 66, no. 7-8, p. 163, 1944.

[125] M. N. Polyanskiy, "Refractive index database." https://refractiveindex.info. Accessed on 2021-06-30.

[126] J.-F. Masson, M.-P. Murray-Méthot, and L. S. Live, "Nanohole arrays in chemical analysis: manufacturing methods and applications," *Analyst*, vol. 135, no. 7, pp. 1483–1489, 2010.

[127] R. Pease, "Electron beam lithography," *Contemporary Physics*, vol. 22, no. 3, pp. 265–290, 1981.

[128] C. Escobedo, "On-chip nanohole array based sensing: a review," *Lab on a Chip*, vol. 13, no. 13, pp. 2445–2463, 2013.

[129] R. Watkins, P. Rockett, S. Thoms, R. Clampitt, and R. Syms, "Focused ion beam milling," *Vacuum*, vol. 36, no. 11-12, pp. 961–967, 1986.

[130] K. Takamura, H. Fischer, and N. R. Morrow, "Physical properties of aqueous glycerol solutions," *Journal of Petroleum Science and Engineering*, vol. 98, pp. 50–60, 2012.

[131] M. E. Stewart, C. R. Anderton, L. B. Thompson, J. Maria, S. K. Gray, J. A. Rogers, and R. G. Nuzzo, "Nanostructured plasmonic sensors," *Chemical Reviews*, vol. 108, no. 2, pp. 494–521, 2008.

[132] H.-C. Lee, C.-T. Li, H.-F. Chen, and T.-J. Yen, "Demonstration of an ultrasensitive refractive-index plasmonic sensor by enabling its quadrupole resonance in phase interrogation," *Optics Letters*, vol. 40, no. 22, pp. 5152–5155, 2015.

[133] J. Homola, "Surface plasmon resonance sensors for detection of chemical and biological species," *Chemical Reviews*, vol. 108, no. 2, pp. 462–493, 2008.

[134] C.-l. Wong, H. Ho, K.-s. Chan, S.-y. Wu, and C. Lin, "Application of spectral surface plasmon resonance to gas pressure sensing," *Optical Engineering*, vol. 44, no. 12, pp. 124403–124403, 2005.

[135] K. A. Willets and R. P. Van Duyne, "Localized surface plasmon resonance spectroscopy and sensing," *Annu. Rev. Phys. Chem.*, vol. 58, pp. 267–297, 2007.

[136] H. K. Hunt and A. M. Armani, "Label-free biological and chemical sensors," *Nanoscale*, vol. 2, no. 9, pp. 1544–1559, 2010.

[137] F. Eftekhari, R. Gordon, J. Ferreira, A. Brolo, and D. Sinton, "Polarization-dependent sensing of a self-assembled monolayer using biaxial nanohole arrays," *Applied Physics Letters*, vol. 92, no. 25, p. 253103, 2008.

[138] A. D. Rakić, A. B. Djurišić, J. M. Elazar, and M. L. Majewski, "Optical properties of metallic films for vertical-cavity optoelectronic devices," *Applied Optics*, vol. 37, no. 22, pp. 5271–5283, 1998.

[139] X. Zhang, G. Liu, Y. Hu, Z. Liu, Z. Cai, Y. Chen, X. Liu, G. Fu, G. Gu, and M. Liu, "Enhanced optical transmission in a plasmonic nanostructure perforated with compound holes and nanorods," *Optics Communications*, vol. 325, pp. 105–110, 2014.

[140] S. Sanders, M. Dowran, U. Jain, T.-M. Lu, A. M. Marino, and A. Manjavacas, "Quantum-enhanced sensing using lattice resonances supported by metallic nanohole arrays," *Submitted for publication*, vol. -, no. -, pp. –, 2021.

[141] A. Blanchard-Dionne, L. Guyot, S. Patskovsky, R. Gordon, and M. Meunier, "Intensity based surface plasmon resonance sensor using a nanohole rectangular array," *Optics Express*, vol. 19, no. 16, pp. 15041–15046, 2011.

[142] U. Jain, M. Dowran, and A. Marino, "Enhanced quantum sensing with dual probing twin beams," *Bulletin of the American Physical Society*, 2021.

[143] W. Fan, B. J. Lawrie, and R. C. Pooser, "Quantum plasmonic sensing," *Physical Review A*, vol. 92, no. 5, p. 053812, 2015.

[144] J.-S. Lee, T. Huynh, S.-Y. Lee, K.-G. Lee, J. Lee, M. Tame, C. Rockstuhl, and C. Lee, "Quantum noise reduction in intensity-sensitive surface-plasmon-resonance sensors," *Physical Review A*, vol. 96, no. 3, p. 033833, 2017.

[145] B. Lawrie, P. Evans, and R. Pooser, "Extraordinary optical transmission of multimode quantum correlations via localized surface plasmons," *Physical Review Letters*, vol. 110, no. 15, p. 156802, 2013.

[146] B. Edlén, "The refractive index of air," *Metrologia*, vol. 2, no. 2, p. 71, 1966.

[147] D. A. Hill and D. P. Haworth, "Accurate measurement of low signal-to-noise ratios using a superheterodyne spectrum analyzer," *IEEE Transactions on Instrumentation and Measurement*, vol. 39, no. 2, p. 432, 1990.

[148] K. McKenzie, N. Grosse, W. P. Bowen, S. E. Whitcomb, M. B. Gray, D. E. McClelland, and P. K. Lam, "Squeezing in the audio gravitational-wave detection band," *Physical Review Letters*, vol. 93, no. 16, p. 161105, 2004.

[149] H. Vahlbruch, S. Chelkowski, B. Hage, A. Franzen, K. Danzmann, and R. Schnabel, "Coherent control of vacuum squeezing in the gravitational-wave detection band," *Physical Review Letters*, vol. 97, no. 1, p. 011101, 2006.

[150] Y. Poujet, J. Salvi, and F. I. Baida, "90% extraordinary optical transmission in the visible range through annular aperture metallic arrays," *Optics Letters*, vol. 32, no. 20, pp. 2942–2944, 2007.

[151] K. M. McPeak, S. V. Jayanti, S. J. Kress, S. Meyer, S. Iotti, A. Rossinelli, and D. J. Norris, "Plasmonic films can easily be better: rules and recipes," *ACS Photonics*, vol. 2, no. 3, pp. 326–333, 2015.

[152] N. Spagnolo, L. Aparo, C. Vitelli, A. Crespi, R. Ramponi, R. Osellame, P. Mataloni, and F. Sciarrino, "Quantum interferometry with three-dimensional geometry," *Scientific Reports*, vol. 2, no. 1, pp. 1–6, 2012.

[153] M. D. Vidrighin, G. Donati, M. G. Genoni, X.-M. Jin, W. S. Kolthammer, M. Kim, A. Datta, M. Barbieri, and I. A. Walmsley, "Joint estimation of phase and phase diffusion for quantum metrology," *Nature Communications*, vol. 5, no. 1, pp. 1–7, 2014.

[154] X. Guo, C. R. Breum, J. Borregaard, S. Izumi, M. V. Larsen, T. Gehring, M. Christandl, J. S. Neergaard-Nielsen, and U. L. Andersen, "Distributed quantum sensing in a continuous-variable entangled network," *Nature Physics*, vol. 16, no. 3, pp. 281–284, 2020.

[155] M. Lassen, V. Delaubert, J. Janousek, K. Wagner, H.-A. Bachor, P. K. Lam, N. Treps, P. Buchhave, C. Fabre, and C. Harb, "Tools for multimode quantum information: modulation, detection, and spatial quantum correlations," *Physical Review Letters*, vol. 98, no. 8, p. 083602, 2007.

[156] T. Baumgratz and A. Datta, "Quantum enhanced estimation of a multidimensional field," *Physical Review Letters*, vol. 116, no. 3, p. 030801, 2016.

[157] A. Muraviev, V. Smolski, Z. Loparo, and K. Vodopyanov, "Massively parallel sensing of trace molecules and their isotopologues with broadband subharmonic mid-infrared frequency combs," *Nature Photonics*, vol. 12, no. 4, pp. 209–214, 2018.

[158] S. S. Acimovic, M. A. Ortega, V. Sanz, J. Berthelot, J. L. Garcia-Cordero, J. Renger, S. J. Maerkl, M. P. Kreuzer, and R. Quidant, "Lspr chip for parallel, rapid, and sensitive detection of cancer markers in serum," *Nano Letters*, vol. 14, no. 5, pp. 2636–2641, 2014.

[159] R. Thijssen, T. J. Kippenberg, A. Polman, and E. Verhagen, "Parallel transduction of nanomechanical motion using plasmonic resonators," *ACS Photonics*, vol. 1, no. 11, pp. 1181–1188, 2014.

[160] S. Altenburg and S. Wölk, "Multi-parameter estimation: global, local and sequential strategies," *Physica Scripta*, vol. 94, no. 1, p. 014001, 2018.

[161] T. J. Proctor, P. A. Knott, and J. A. Dunningham, "Multiparameter estimation in networked quantum sensors," *Physical Review Letters*, vol. 120, no. 8, p. 080501, 2018.

[162] V. Boyer, A. M. Marino, R. C. Pooser, and P. D. Lett, "Entangled images from four-wave mixing," *Science*, vol. 321, no. 5888, pp. 544–547, 2008.

[163] A. Kumar, G. Nirala, and A. M. Marino, "Einstein-podolsky-rosen paradox with position-momentum entangled macroscopic twin beams," *arXiv preprint arXiv:2007.09259*, 2020.

[164] H. Qi, K. Brádler, C. Weedbrook, and S. Guha, "Quantum precision of beam pointing," *arXiv preprint arXiv:1808.01302*, 2018.

[165] P. Zoller, T. Beth, D. Binosi, R. Blatt, H. Briegel, D. Bruss, T. Calarco, J. I. Cirac, D. Deutsch, J. Eisert, *et al.*, "Quantum information processing and communication," *The European Physical Journal D-Atomic, Molecular, Optical and Plasma Physics*, vol. 36, no. 2, pp. 203–228, 2005.

[166] M. Dowran, A. Kumar, A. Marino, B. J. Lawrie, and R. C. Pooser, "Quantum plasmonic sensing beyond the classical limit," *Optics and Photonics News*, vol. 2018, no. 12, 2018.

[167] M. Dowran, A. Win, U. Jain, B. Lawrie, R. Pooser, and A. Marino, "Parallel quantum sensing with spatially multimode twin beams of light," *Bulletin of the American Physical Society*, 2021.

[168] M. Dowran, T. S. Woodworth, and A. M. Marino, "Phase-and transmission-based quantum-enhanced resonance sensing at the quantum cramér rao bound," in *Frontiers in Optics*, pp. FW7C–3, Optical Society of America, 2020.

[169] M. Dowran, A. L. Win, A. Kumar, B. J. Lawrie, R. C. Pooser, and A. M. Marino, "Parallel quantum enhanced plasmonic sensing through spatial quantum correlations," in *Frontiers in Optics*, pp. JTu3A–48, Optical Society of America, 2019.

[170] A. Win, M. Dowran, A. Kumar, B. J. Lawrie, R. C. Pooser, and A. M. Marino, "Parallel quantum-enhanced plasmonic sensing," in *APS Division of Atomic, Molecular and Optical Physics Meeting Abstracts*, vol. 2019, pp. D08–005, 2019.

[171] M. Dowran, A. Kumar, B. J. Lawrie, R. C. Pooser, and A. M. Marino, "Sensitivity improvement of quantum-enhanced plasmonic sensing with phase-based configuration," *Bulletin of the American Physical Society*, vol. 64, 2019.

[172] A. Kumar, M. Dowran, B. Lawrie, R. Pooser, and A. Marino, "Quantum-enhanced ultrasound detection with plasmonic sensors," in *CLEO: QELS_Fundamental Science*, pp. JF2B–6, Optical Society of America, 2018.

[173] A. Kumar, M. Dowran, B. Lawrie, R. Pooser, and A. Marino, "Plasmonic sensing beyond the shot noise limit," in *Frontiers in Optics*, pp. JW3A–10, Optical Society of America, 2017.

[174] M. Dowran, A. Kumar, B. Lawrie, R. Pooser, and A. Marino, "Quantum sensing beyond the shot-noise limit with plasmonic sensors," in *APS Division of Atomic, Molecular and Optical Physics Meeting Abstracts*, vol. 2017, pp. T7–007, 2017.

[175] M. Dowran, M. W. Holtfrerich, R. Davidson, B. J. Lawrie, R. C. Pooser, and A. M. Marino, "Transduction of entangled images by localized surface plasmons," in *Quantum Information and Measurement*, pp. QW5A–2, Optical Society of America, 2017.

[176] M. Dowran, M. Holtfrerich, B. Lawrie, R. Davidson, R. Pooser, and A. Marino, "Transduction of entangled images by localized surface plasmons," *Bulletin of the American Physical Society*, vol. 61, 2016.

Appendix A

Publications and Conference Presentations

A.1 Publications

Below is a list of peer-reviewed publications in which I was either the first or the second author. The list is in reverse chronological order.

6. Umang Jain, **Mohammadjavad Dowran**, Alberto M. Marino, "Extra Quantum Enhanced Plasmonic Sensing with Orthogonally Polarized Twin Beams," (*on-going work*)

5. **Mohammadjavad Dowran**, Aye L. Win, Umang Jain, Ashok Kumar, Benjamin J. Lawrie, Raphael C. Pooser, and Alberto M. Marino, "Parallel Quantum Plasmonic Sensing," (*under preparation*)

4. Stephen Sanders, **Mohammadjavad Dowran**, Umang Jain, Tzu-Ming Lu, Alberto M. Marino, and Alejandro Manjavacas, "Quantum-enhanced sensing using lattice resonances supported by metallic nanohole arrays," (*submitted for publication*)

3. **Mohammadjavad Dowran**, Timothy S. Woodworth, Ashok Kumar, and Alberto M. Marino1, "Fundamental Bounds of Sensitivity of Quantum Enhanced Sensitivities at the Cramér Rao Bound," (*submitted for publication, currently on arXiv* [71])

2. **Mohammadjavad Dowran**, Ashok Kumar, Benjamin J. Lawrie, Raphael C. Pooser, Alberto M. Marino, "Quantum-Enhanced Plasmonic Sensing", Optica 5 (5), pp. 628-633 (2018) [73]. This paper was selected as one of the main achievements of optics and photonics community in 2018. The report was published in: **Mohammadjavad Dowran**, Ashok Kumar, Benjamin J. Lawrie, Raphael C. Pooser, and Alberto M. Marino, "Quantum Plasmonic Sensing Beyond the Classical Limit," Optics and Photonics News (OPN), December 2018 [166]

1. Matthew W. Holtfrerich, **Mohammadjavad Dowran**, Roderick Davidson, Benjamin J. Lawrie, Raphael C. Pooser, and Alberto M. Marino, "Toward quantum plasmonic networks," Optica 3 (9), pp. 985-988 (2016) [72]

A.2 Conference Presentations

Below is a list of the presentations that I have either presented or been co-author of the presentation:

13. **Mohammadjavad Dowran**, Aye L. Win, Umang Jain, Benjamin Lawrie, Raphael Pooser, Alberto M. Marino, "Parallel Quantum Sensing with Spatially Multimode Twin Beams of Light," 52$^{\text{nd}}$ Annual Meeting of the APS Division of Atomic, Molecular, and Optical Physics (DAMOP), June 2021 [online] [167]

12. Umang Jain, **Mohammadjavad Dowran**, Alberto M. Marino, "Enhanced Quantum Sensing with Dual Probing Twin Beams," 52$^{\text{nd}}$ Annual Meeting of the APS Division of Atomic, Molecular, and Optical Physics (DAMOP), June 2021 [online] [142]

11. **Mohammadjavad Dowran**, Timothy S. Woodworth, Alberto M. Marino, "Phase- and Transmission-Based Quantum-Enhanced Resonance Sensing at the Quantum Cramér Rao Bound," Frontiers in Optics (FIO) 2020, Washington, DC [online] [168]

10. **Mohammadjavad Dowran**, Aye L Win, Ashok Kumar, Benjamin J Lawrie, Raphael C. Pooser, Alberto M. Marino, "Parallel Quantum Enhanced Plasmonic Sensing through Spatial Quantum Correlations," Frontiers in Optics (FIO) 2019, Washington, DC [169]

9. Aye L. Win, **Mohammadjavad Dowran**, Ashok Kumar, Benjamin J. Lawrie, Raphael C. Pooser, Alberto M. Marino, "Parallel Quantum-Enhanced Plasmonic Sensing," 50$^{\text{th}}$ Annual Meeting of the APS Division of Atomic, Molecular, and Optical Physics (DAMOP) 2019, Milwaukee, WI [170]

8. **Mohammadjavad Dowran**, Ashok Kumar, Benjamin J. Lawrie, Raphael C. Pooser, Alberto M. Marino, "Sensitivity Improvement of Quantum-Enhanced Plasmonic Sensing with Phase-Based Configuration," 50$^{\text{th}}$ Annual Meeting of the APS Division of Atomic, Molecular, and Optical Physics (DAMOP) 2019, Milwaukee, WI [171]

7. Ashok Kumar, **Mohammadjavad Dowran**, Benjamin J. Lawrie, Raphael C. Pooser, Alberto M. Marino, "Quantum-Enhanced Ultrasound Detection with Plasmonic Sensors," CLEO 2018, San Jose, CA [172]

6. **Mohammadjavad Dowran**, Ashok Kumar, Benjamin J. Lawrie, Raphael C. Pooser, Alberto Marino, "Quantum-Enhanced Plasmonic Sensing with Different

Detection Schemes," The International Conference on Quantum Communication, Measurement and Computing (QCMC) 2018, Baton Rouge, LA

5. Ashok Kumar, **Mohammadjavad Dowran**, Benjamin J. Lawrie, Raphael C. Pooser, Alberto M. Marino, "Plasmonic Sensing Beyond the Shot-Noise Limit," Frontiers in Optics (FIO) 2017, Washington, DC [173]

4. **Mohammadjavad Dowran**, Ashok Kumar, Benjamin J. Lawrie, Raphael C. Pooser, Alberto M. Marino, "Quantum Sensing Beyond the Shot-Noise Limit with Plasmonic Sensors," 48$^{\text{th}}$ Annual Meeting of the APS Division of Atomic, Molecular, and Optical Physics (DAMOP) 2017, Sacramento, CA [174]

3. **Mohammadjavad Dowran**, Matthew Holtfrerich, Raphael C. Pooser, Benjamin J. Lawrie, Roderick Davidson, Alberto M. Marino, "Transduction of Entangled Images by Localized Surface Plasmons," Quantum Information and Measurement 2017, Paris, France [175]

2. **Mohammadjavad Dowran**, Matthew Holtfrerich, Raphael C. Pooser, Benjamin J. Lawrie, Roderick Davidson, Alberto M. Marino, "Transduction of Entangled Images by Localized Surface Plasmons," 47$^{\text{th}}$ Annual Meeting of the APS Division of Atomic, Molecular and Optical Physics (DAMOP), 2016 Providence, RI [176]

1. **Mohammadjavad Dowran**, Matthew Holtfrerich, Raphael C. Pooser, Benjamin J. Lawrie, Alberto M. Marino, "Transduction of Entangled Images by Localized Surface Plasmons," 18$^{\text{th}}$ Annual SQuInT Workshop 2016, Albuquerque, NM